



Universitetet  
i Stavanger

Faculty of Science and Technology

## MASTER'S THESIS

Study Program/ Specialization:

Marine and Offshore Technology

Spring semester, 2020

Open / ~~Restricted~~ access

Writer:

Clarissa Pires Vieira Serta

(Writer's signature)

Faculty supervisor:

Prof. Muk Chen Ong

Marek Jan Janocha

Dr. Guang Yin

Thesis title:

Computational Fluid Dynamics (CFD) Investigations of Flow-Induced Vibrations of Two Rigidly Coupled Cylinders at High Reynolds Number

Credits (ECTS): 30

Key words:

turbulent flow, rigidly coupled cylinders,  
flow-induced vibrations, CFD, URANS,  
OpenFOAM

Pages: 86

+ Enclosure: 12

Stavanger, July 12, 2020

Date/year

## Abstract

Two degree-of-freedom (2-DoF) flow-induced vibrations (FIV) of a single cylinder and two rigidly coupled cylinders are numerically investigated at the Reynolds number of  $3.6 \times 10^6$ . Two-dimensional (2D) Unsteady Reynolds-Averaged Navier-Stokes (URANS) simulations are performed combined with the  $k - \omega$  SST turbulence model. A low mass-damping system is considered with the mass ratio set to 2 and the damping ratio to zero. For the coupled cylinders configurations, the diameter ratio is set to 0.25. A parametric study is performed to analyse the influence of the reduced velocity ( $U_r$ ), the position angle ( $\alpha$ ) of the small cylinder relative to the large cylinder and the gap ratio ( $G/D$ ) between the cylinders on the FIV response of the system. For the single cylinder, the simulations are performed for  $2.5 \leq U_r \leq 12$ , and for the coupled cylinders, for  $2 \leq U_r \leq 12$ . To analyse the effect of  $\alpha$ , three values are considered, [ $\alpha = 0^\circ, 90^\circ, 180^\circ$ ] with a constant value of  $G/D = 0.1$ . The effect of  $G/D$  is studied for the  $\alpha = 90^\circ$  configuration in which the  $G/D = 0.25$  and  $G/D = 0.5$  configurations are analysed in addition to the  $G/D = 0.1$  cases. A good grid convergence is obtained and the numerical model is validated against published results for a stationary single cylinder. It is found that the lock-in regime extends beyond  $U_r = 12$  for the  $\alpha = 0^\circ, 180^\circ$  and  $\alpha = 90^\circ$  at  $G/D = 0.1, 0.25$  configurations compared with the single cylinder configuration. Galloping response is observed when the small cylinder is placed at  $\alpha = 90^\circ$ , with  $G/D = 0.1$ , and at  $\alpha = 180^\circ$ . In addition, for the  $\alpha = 90^\circ$  configuration, the results obtained for  $\overline{C}_D$ ,  $\overline{C}_L$  and  $A_{y,max}/D$  converge to those of the single cylinder with the increase of  $G/D$ .

## Acknowledgments

I would like to express my sincere gratitude to Prof. Muk Chen Ong for the privilege of working under his supervision. I also appreciate his continuous support and guidance during this study.

I would like to thank my co-supervisors Marek Janocha and Dr. Guang Yin for their valuable contribution to this thesis. They have always provided important comments and advices that have helped to improve the present work.

I would like to acknowledge the Department of Mechanical and Structural Engineering and Materials Science of the University of Stavanger for all the necessary resources for the completion of this work.

My heartfelt gratitude to my dear husband, Vinicius, for sharing this journey with me. His continuous love, support and patience have been invaluable to the accomplishment of this work.

Most of all, I am grateful to my family for their constant encouragement. This journey would not have been possible without the love and support from my parents and my sisters.

# Table of Contents

<b>Abstract</b> .....	i
<b>Acknowledgements</b> .....	ii
<b>Table of Contents</b> .....	iii
<b>List of Figures</b> .....	vi
<b>List of Tables</b> .....	x
<b>1 Introduction</b> .....	1
1.1 Background and Motivation.....	1
1.2 Research Objectives and Outline of the Thesis.....	4
<b>2 Theory</b> .....	6
2.1 Flow Around a Circular Cylinder.....	6
2.1.1 Flow Regimes.....	7
2.2 Turbulent Flow.....	9
2.3 Boundary Layer.....	10
2.3.1 Turbulent Boundary Layer.....	12
2.4 Vortex Shedding.....	14
2.5 Hydrodynamic Forces in Fluid-Structure Interactions.....	16
2.5.1 Drag and Lift Coefficients.....	17
2.5.2 Pressure and Skin Friction Coefficients.....	17

2.6 Flow-Induced Vibrations.....	18
2.6.1 Equation of Motion.....	18
2.6.2 Added Mass.....	20
2.6.3 Strouhal Number.....	20
2.6.4 Reduced Velocity.....	22
2.6.5 Mass Ratio.....	22
2.6.6 Amplitude Ratio.....	22
2.6.7 Lock-in.....	23
<b>3 Numerical Method.....</b>	<b>25</b>
3.1 Computational Fluid Dynamics.....	25
3.1.1 Introduction.....	25
3.1.2 OpenFOAM.....	25
3.2 Governing Equations.....	27
3.2.1 Conservation of Mass and Momentum.....	27
3.2.2 Reynolds-Averaged Navier-Stokes Equations.....	28
3.3 Finite Volume Method.....	30
3.3.1 Spatial Discretization.....	30
3.3.2 Temporal Discretization.....	32
3.4 PIMPLE.....	32
3.5 Turbulence Modelling.....	33
3.5.1 $k - \omega$ SST Turbulence Model.....	33
<b>4 Numerical Model.....</b>	<b>36</b>
4.1 Numerical Set-up.....	36
4.2 Convergence Studies.....	38
4.3 Model Validation.....	44
<b>5 Flow-Induced Vibrations of Two Rigidly Coupled Cylinders at <math>Re = 3.6 \times 10^6</math> ..</b>	<b>47</b>
5.1 Introduction.....	47

5.2 Effect of the Position Angle $\alpha$ .....	47
5.2.1 Hydrodynamic Force Coefficients.....	47
5.2.2 Amplitude Response.....	50
5.2.3 Frequency Analysis.....	51
5.2.4 Motion Trajectories.....	56
5.2.5 Flow Field Analysis.....	59
5.3 Effect of the Gap Ratio $G/D$ .....	67
5.3.1 Hydrodynamic Force Coefficients.....	67
5.3.2 Amplitude Response.....	70
5.3.3 Frequency Analysis.....	71
5.3.4 Motion Trajectories.....	73
5.3.5 Flow Field Analysis.....	75
<b>6 Conclusions and Recommendations for Future Work.....</b>	<b>80</b>
6.1 Conclusions.....	80
6.2 Recommendations for Future Work .....	82
<b>References.....</b>	<b>83</b>
<b>Appendix A</b> Time histories of the hydrodynamic coefficients and the normalized displacements	

## List of Figures

2.1	Flow field around a circular cylinder.....	6
2.2	Schematic depiction of a velocity profile within the boundary layer.....	10
2.3	Velocity profiles close to the separation point S.....	11
2.4	Development of the boundary layer along a flat plate.....	12
2.5	Plot of velocity profiles within the turbulent boundary layer.....	13
2.6	Vortex shedding process.....	14
2.7	Pressure distribution around the cylinder and the total force during vortex shedding.....	16
2.8	Strouhal number dependency with the Reynolds number.....	21
2.9	Response amplitude of a low mass-damping system.....	23
2.10	Experimental response frequency of a submerged oscillating cylinder.....	24
3.1	OpenFOAM case directory structure.....	26
3.2	Graphical representation of Reynolds decomposition to velocity field.....	29
3.3	Generic representation of a control volume.....	30
3.4	Example of unstructured (a) and structured (b) meshes.....	31
3.5	PIMPLE algorithm flowchart.....	33
4.1	Representation of the computational domain.....	36
4.2	Computational mesh for the single cylinder cases: mesh A3 (Table 4.1), 104536 cells.....	39
4.3	Mesh details around the cylinder for the single cylinder cases.....	39
4.4	Computational mesh for the two coupled cylinders cases with $\alpha = 90^\circ$ and $G/D = 0.1$ configuration: mesh B3 (Table 4.4), 114321 cells.....	43
4.5	Mesh details around the cylinders for the two coupled cylinders cases	

	with $\alpha = 90^\circ$ and $G/D = 0.1$ configuration.....	43
4.6	Time-averaged pressure distribution (a) and skin friction distribution (b) around the single stationary cylinder at $Re = 3.6 \times 10^6$ .....	46
5.1	Time-averaged drag coefficient $\bar{C}_D$ (a) and root-mean-square of the drag coefficient $C_{D,rms}$ (b) for the single cylinder and $\alpha = [0^\circ, 90^\circ, 180^\circ]$ configurations .....	48
5.2	Time-averaged lift coefficient $\bar{C}_L$ (a) and root-mean-square of the lift coefficient $C_{L,rms}$ (b) for the single cylinder and $\alpha = [0^\circ, 90^\circ, 180^\circ]$ configurations .....	49
5.3	Normalized maximum cross-flow vibration amplitude $A_{y,max}/D$ (a) and normalized root-mean-square of the in-line vibration amplitude $A_{x,rms}/D$ (b) for the single cylinder and $\alpha = [0^\circ, 90^\circ, 180^\circ]$ configurations .....	50
5.4	Frequency spectra of $C_L$ , $y/D$ , $C_D$ and $x/D$ : single cylinder.....	52
5.5	Frequency spectra of $C_L$ , $y/D$ , $C_D$ and $x/D$ : coupled cylinders $\alpha = 0^\circ$ , $G/D = 0.1$ .....	53
5.6	Frequency spectra of $C_L$ , $y/D$ , $C_D$ and $x/D$ : coupled cylinders $\alpha = 90^\circ$ , $G/D = 0.1$ .....	54
5.7	Frequency spectra of $C_L$ , $y/D$ , $C_D$ and $x/D$ : coupled cylinders $\alpha = 180^\circ$ , $G/D = 0.1$ .....	55
5.8	Frequency spectra of $y/D$ for the single cylinder and $\alpha = [0^\circ, 90^\circ, 180^\circ]$ configurations at selected $U_r$ corresponding to the cases with the largest transverse displacement amplitude.....	56
5.9	$x/D - y/D$ trajectory: single cylinder.....	57
5.10	$x/D - y/D$ trajectory: coupled cylinders $\alpha = 0^\circ$ , $G/D = 0.1$ .....	57
5.11	$x/D - y/D$ trajectory: coupled cylinders $\alpha = 90^\circ$ , $G/D = 0.1$ .....	58
5.12	$x/D - y/D$ trajectory: coupled cylinders $\alpha = 180^\circ$ , $G/D = 0.1$ .....	58
5.13	Contours of (a, c, e, g) the spanwise vorticity and (b, d, f, h) normalized pressure with streamlines for one vortex shedding cycle: single cylinder at $U_r = 8$ .....	60



5.14	Time histories of $C_L$ , $C_D$ , $y/D$ and $x/D$ : single cylinder at $U_r = 8$ .....	61
5.15	Contours of (a, c, e, g) the spanwise vorticity and (b, d, f, h) normalized pressure with streamlines for one vortex shedding cycle: coupled cylinders $\alpha = 0^\circ$ , $G/D = 0.1$ at $U_r = 6$ .....	62
5.16	Time histories of $C_L$ , $C_D$ , $y/D$ and $x/D$ : coupled cylinders $\alpha = 0^\circ$ , $G/D = 0.1$ at $U_r = 6$ .....	63
5.17	Contours of (a, c, e, g) the spanwise vorticity and (b, d, f, h) normalized pressure with streamlines for one vortex shedding cycle: coupled cylinders $\alpha = 90^\circ$ , $G/D = 0.1$ at $U_r = 12$ .....	64
5.18	Time histories of $C_L$ , $C_D$ , $y/D$ and $x/D$ : coupled cylinders $\alpha = 90^\circ$ , $G/D = 0.1$ at $U_r = 12$ .....	65
5.19	Contours of (a, c, e, g) the spanwise vorticity and (b, d, f, h) normalized pressure with streamlines for one vortex shedding cycle: coupled cylinders $\alpha = 180^\circ$ , $G/D = 0.1$ at $U_r = 12$ .....	66
5.20	Time histories of $C_L$ , $C_D$ , $y/D$ and $x/D$ : coupled cylinders $\alpha = 180^\circ$ , $G/D = 0.1$ at $U_r = 12$ .....	67
5.21	Time-averaged drag coefficient $\bar{C}_D$ (a) and the root-mean-square of the drag coefficient $C_{D,rms}$ (b) for the single cylinder and [ $G/D = 0.1, 0.25, 0.5$ ] configurations .....	68
5.22	Time-averaged lift coefficient $\bar{C}_L$ (a) and root-mean-square of the lift coefficient $C_{L,rms}$ (b) for the single cylinder and [ $G/D = 0.1, 0.25, 0.5$ ] configurations .....	69
5.23	Normalized maximum cross-flow vibration amplitude $A_{y,max}/D$ (a) and normalized root-mean-square of the in-line vibration amplitude $A_{x,rms}/D$ (b) for the single cylinder and [ $G/D = 0.1, 0.25, 0.5$ ] configurations .....	70
5.24	Frequency spectra of $C_L$ , $y/D$ , $C_D$ and $x/D$ : coupled cylinders $\alpha = 90^\circ$ , $G/D = 0.25$ .....	71
5.25	Frequency spectra of $C_L$ , $y/D$ , $C_D$ and $x/D$ : coupled cylinders $\alpha = 90^\circ$ , $G/D = 0.5$ .....	72
5.26	Frequency spectra of $y/D$ for the single cylinder and [ $G/D = 0.1, 0.25,$	

0.5]	configurations at selected $U_r$ corresponding to the cases with the largest transverse displacement amplitude.....	73
5.27	$x/D - y/D$ trajectory: coupled cylinders $\alpha = 90^\circ$ , $G/D = 0.25$ .....	74
5.28	$x/D - y/D$ trajectory: coupled cylinders $\alpha = 90^\circ$ , $G/D = 0.5$ .....	74
5.29	Contours of (a, c, e, g) the spanwise vorticity and (b, d, f, h) normalized pressure with streamlines for one vortex shedding cycle: coupled cylinders $\alpha = 90^\circ$ , $G/D = 0.25$ at $U_r = 6$ .....	76
5.30	Time histories of $C_L$ , $C_D$ , $y/D$ and $x/D$ : coupled cylinders $\alpha = 90^\circ$ , $G/D = 0.25$ at $U_r = 6$ .....	77
5.31	Contours of (a, c, e, g) the spanwise vorticity and (b, d, f, h) normalized pressure with streamlines for one vortex shedding cycle: coupled cylinders $\alpha = 90^\circ$ , $G/D = 0.5$ at $U_r = 8$ .....	78
5.32	Velocity profile in the gap between the cylinders: $G/D = 0.1$ at $U_r = 12$ , $G/D = 0.25$ at $U_r = 6$ and $G/D = 0.5$ at $U_r = 8$ .....	79
5.33	Time histories of $C_L$ , $C_D$ , $y/D$ and $x/D$ : coupled cylinders $\alpha = 90^\circ$ , $G/D = 0.5$ at $U_r = 8$ .....	79

## List of Tables

2.1	Flow regimes around a circular cylinder.....	8
2.2	Modes of vortex shedding.....	15
3.1	Coefficient values in $k - \omega$ SST model.....	35
4.1	Mesh convergence study for the stationary single cylinder.....	41
4.2	Mesh convergence study for the vibrating single cylinder.....	42
4.3	Time step convergence study for the vibrating single cylinder.....	42
4.4	Mesh convergence study for the two vibrating rigidly coupled cylinders with $\alpha = 90^\circ$ and $G/D = 0.1$ configuration.....	44
4.5	Numerical and experimental data of a single stationary cylinder at high Reynolds number regime.....	45

# Chapter 1

## Introduction

### 1.1 Background and Motivation

Flow around a circular cylinder is a canonical case in fluid mechanics and has been well studied, both experimentally and numerically. It can be encountered in many engineering applications, for instance in heat exchanger tubes, chimneys, and ocean structures such as marine risers and pipelines. Many complex phenomena can occur due to the interaction of the body with the surrounding fluid flow. An important example of fluid-structure interactions (FSI) is flow-induced vibrations (FIV). A subclass of FIV is denoted as vortex-induced vibrations (VIV), caused by the periodic separation of the flow around the cylinder, known as vortex shedding. In the offshore oil and gas industry, VIV can lead to fatigue failure of deepwater risers. Hence, it is of great significance to investigate the FIV phenomena.

In practice, cylinder-type structures can often be installed in groups. The bodies can have similar diameter or not, and the spacing between them can also vary depending on the application. Consequently, it is known that those different configurations cause changes to the surrounding flow field compared to the flow around a single cylinder (Sumner, 2010). It is expected to observe changes in the hydrodynamic loading due to the distinct interactions between shear layers and wakes depending on the configuration.

Regarding FIV, placing one or more objects close to the main cylinder may lead to the suppression of the vortex shedding behind the main body (Lam and Lin, 2008). One example is the so-called piggyback pipeline, in which a second small pipe is placed in close proximity to the main pipe; both are strapped at certain intervals along their length and laid together. The main one is used to transport oil and gas, while the secondary pipe is employed to transport monitoring signals. The presence of the additional pipeline influences the dynamic response of the main pipe.

Compared with the study of VIV of a single cylinder, which can be found in the extensive reviews of Sarpkaya (1979), Williamson and Govardhan (2004) and Nakamura et al. (2013), less attention has been given to VIV of coupled cylinders under the same flow conditions. To date, there are relatively few experimental studies on the effects of VIV on two rigidly coupled cylinders with different diameters.

The work of Feng (1968) is among the earliest publications on VIV of elastically mounted cylinders. He investigated the one degree-of-freedom (1-DoF) VIV of a single cylinder and demonstrated the lock-in phenomenon. Kalghatgi and Sayer (1997) conducted experiments on piggyback pipelines at the Reynolds numbers between  $9 \times 10^4$  and  $3 \times 10^5$  ( $Re = U_\infty D/\nu$ , where  $U_\infty$  is the free stream velocity,  $D$  denotes the diameter of the large cylinder and  $\nu$  is the flow viscosity). They reported that the drag force is increased with the presence of the secondary pipe compared with that on a single cylinder. Besides, in the subcritical Reynolds number regime, the lift force points downward to the seabed, whereas in the critical Reynolds number regime, it points in the opposite direction. In the case of a single cylinder, the direction of the lift force is always towards the seabed, for the studied flow regimes. Tsutsui et al. (1997) investigated the flow around two stationary coupled cylinders at Reynolds numbers in the order of  $O(10^4)$ . The diameter ratio,  $d/D$  (where  $d$  is the diameter of the small cylinder) and the gap ratio  $G/D$  (where  $G$  is the distance between the cylinders) were kept constant at 0.45 and 0.06, respectively. The position angle  $\alpha$  (defined as the angle between the horizontal plane and the line connecting the cylinders centres) was varied from  $90^\circ$  (cylinders are vertically aligned) to  $180^\circ$  (small cylinder downstream the large one). They noticed that when  $\alpha \geq 150^\circ$ , the drag force on the main cylinder is lower compared to that on a single cylinder, and the lift force becomes zero. This was attributed to the presence of the small cylinder in the wake of the large one. Zang et al. (2012) conducted experiments using particle image velocimetry (PIV) to study vortex shedding and VIV of piggyback pipelines in the subcritical flow regime. Their results showed that the amplitude ratio  $A/D$  (where  $A$  denotes the vibration amplitude of the cylinder) is dependent on the gap ratio  $G/D$ . For  $G/D$  larger than 0.3, the amplitude resembles that of an isolated cylinder, so the influence of the small pipeline on the large one is small. In the work of Zang and Gao (2014), VIV response of piggyback pipelines was investigated using a hydro-elastic facility. Several configuration parameters were studied, such as  $\alpha$ ,  $d/D$  and  $G/D$ , and

different Reynolds number values in the order of  $O(10^4)$  were investigated. They found that VIV is suppressed significantly in the side-by-side configuration ( $\alpha = 90^\circ$ ) and when  $G/D = 0.25$ .

Numerical studies have also been conducted to study cylinders in various flow regimes. Ong et al. (2009) performed two-dimensional (2D) Unsteady Reynolds-Averaged Navier-Stokes (URANS) simulations with the  $k - \varepsilon$  model to investigate the flow around a circular cylinder at  $Re = 3.6 \times 10^6$ . They obtained good agreement with the experimental data published by Achenbach (1968). Zhao et al. (2007) investigated the hydrodynamic loading and vortex shedding frequency of coupled cylinders in the subcritical Reynolds number regime. They solved the 2D Reynolds-Averaged Navier-Stokes (RANS) equations with a Finite Element Method (FEM) and the  $k - \omega$  turbulence model. One of the main findings of the study by Zhao et al. (2007) is the classification of two characteristic modes of the vortex shedding. The first mode was named the one-wake mode in which the cylinders behave as one body and it was observed when  $\alpha$  was close to  $0^\circ$  or  $180^\circ$ . The second mode was named as interaction-shedding mode, in which the vortex shedding is influenced by the shear layers downstream the gap between the cylinders. It was observed for  $\alpha$  close to  $90^\circ$ , but it is dependent on  $G/D$ . Regarding numerical simulations of FIV, Zhao and Yan (2013) investigated the two degree-of-freedom (2-DoF) VIV of two cylinders with different diameters in the low Reynolds number regime ( $Re = 250$ ). They employed the Petrov-Galerkin Finite Element Method to solve the 2D URANS equations and the Arbitrary-Lagrangian-Eulerian to deal with the motion of the bodies. The main analysed parameters were  $\alpha$  and  $G/D$  for a low mass-damping system, in which the mass ratio  $m^*$  ( $m^* = m/m_d$ , where  $m$  and  $m_d$  are the mass of the cylinders and the displaced mass, respectively) was set to 2 and the damping ratio  $\zeta$  ( $\zeta = c/2\sqrt{km}$ ,  $c$  is the structural damping and  $k$ , the structural stiffness) was specified as zero. They reported that the lock-in range was increased for certain  $\alpha$  values, such as  $0^\circ$  (small cylinder downstream the large one),  $22.5^\circ$ ,  $90^\circ$  and  $112.5^\circ$ . Also, at  $G/D = 0.2$ , the vibration amplitude is reduced and the lock-in range is narrowed. In the work of Zhao et al. (2016), three-dimensional (3D) simulations were performed to analyse the VIV of two cylinders with different diameter and arranged side-by-side at  $Re = 1000$ . They applied similar numerical method as used by Zhao and Yan (2013). The values of  $m^*$  and  $\zeta$  were kept at 2 and zero, respectively, and the reduced velocity  $U_r$

( $U_r = U_\infty/f_n D$ , here  $f_n$  is the natural frequency of the system) varied from 2 to 15. Zhao et al. (2016) reported that the observed vortex shedding pattern was the 2S mode throughout the range of investigated  $U_r$ . Besides, at  $U_r = 4$ , the root-mean-square of the lift coefficient attained its maximum value and it was similar to that of a single cylinder. For  $U_r$  larger than 10, the drag and lift coefficients were not influenced by the increase of  $U_r$ .

## 1.2 Research Objectives and Outline of the Thesis

The scope of the present thesis is to investigate the flow around a single cylinder and two rigidly coupled cylinders at  $Re = 3.6 \times 10^6$ . The cylinders are elastically mounted and can vibrate in both the in-line and cross-flow directions. The 2D flow is modelled and numerically solved by using Computational Fluid Dynamics (CFD). The chosen software is OpenFOAM (Open Field Operation And Manipulation), an open source code based on the Finite Volume Method (FVM). The studied parameters are:  $U_r$ ,  $\alpha$  and  $G/D$ .

The main objectives of the present study are described as follows:

- The effect of different position angles on the FIV response of two rigidly coupled cylinders are investigated and compared with that of a single cylinder. The hydrodynamic coefficients, such as drag and lift coefficients, the in-line and cross-flow vibration amplitudes, the motion trajectories and the flow fields are analysed.
- The effect of different gaps on the FIV response of two rigidly coupled cylinders are investigated and compared with that of a single cylinder. The hydrodynamic coefficients, such as drag and lift coefficients, the in-line and cross-flow vibration amplitudes, the motion trajectories and the flow fields are analysed.

The structure of the present thesis is outlined as follows:

**Chapter 2:** The main theory of the present study is summarized. The main topics reviewed in this chapter are flow around a circular cylinder, different flow regimes based on the Reynolds number, boundary layer, hydrodynamic forces and flow-induced vibrations.

**Chapter 3:** The numerical simulation methods are introduced in this chapter.

**Chapter 4:** The numerical set up employed in the present study is described in this chapter. Also, convergence and validation studies are performed.

**Chapter 5:** The results of the simulations are presented and discussed in this chapter. The analysis of hydrodynamic quantities, vibration amplitudes, motion trajectories and flow fields for the different studied configurations is carried out.

**Chapter 6:** The main conclusions are addressed in this chapter in conjunction with recommendations for future work.



## Chapter 2

### Theory

#### 2.1 Flow Around a Circular Cylinder

The flow past a circular cylinder is the canonical case of bluff body flow. It can be characterized by boundary layer separation and the wake region downstream the cylinder due to the fluid's viscosity and the presence of the body. As the flow reaches the cylinder, some fluid particles slow down whereas others continue to flow around the object. According to Zdravkovich (1997), four regions can be identified as shown in Figure 2.1:

- i. The narrow region in front of the cylinder is characterized by retarded flow in which the local time-averaged velocity,  $U$ , is smaller than the free stream velocity,  $U_\infty$ .
- ii. The boundary layer region attached to the cylinder wall. The boundary layer thickness,  $\delta$ , is very small compared to the cylinder diameter,  $D$ , so it results in a region characterized by high velocity gradients and considerable shear stress effects.
- iii. Sideways of the cylinder, the flow is accelerated and  $U > U_\infty$  is observed.
- iv. The wake region extends from the separation point over a distance downstream the cylinder and is characterized by  $U < U_\infty$ .

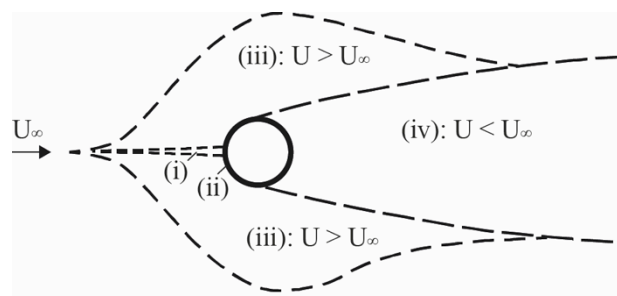


Figure 2.1: Flow field around a circular cylinder (Zdravkovich, 1997)

The non-dimensional quantity known as the Reynolds number is the main governing parameter used to describe the flow behaviour. It represents the ratio between the inertial and viscous forces and can be expressed as:

$$Re = \frac{U_{\infty} D}{\nu} \quad (2.1)$$


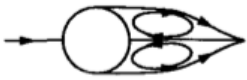


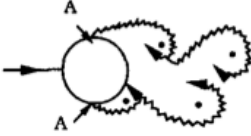
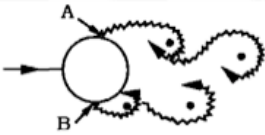
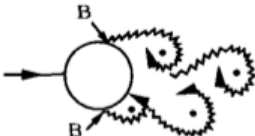
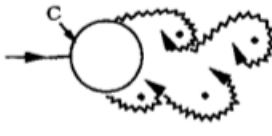

where  $U_{\infty}$  is the free stream velocity,  $\nu$  is the kinematic viscosity and  $D$  is the diameter of the cylinder. As the Reynolds number is increased, the flow experiences changes which can be described by different flow regimes.

### 2.1.1 Flow Regimes

The different flow regimes experienced by the cylinder in a steady current can be classified according to Table 2.1. At very low  $Re$ , the flow is called creeping flow. There is no flow separation, it remains attached to the cylinder surface. At higher  $Re$ ,  $5 < Re < 40$ , the flow begins to separate and two fixed vortices are formed in the wake region. When  $Re$  is further increased, the vortices start to shed alternately on both sides of the cylinder and form the vortex street; this is known as the vortex shedding phenomenon. In the range of  $40 < Re < 200$ , the vortex street is still laminar, the transition to turbulent occurs at  $200 < Re < 300$ . The wake becomes fully turbulent when  $Re$  is further increased, i.e. in the range of  $300 < Re < 3 \times 10^5$ , but the boundary layer is still laminar. This flow regime is called the subcritical regime. The transition to turbulence occurs in the narrow range of  $Re$ ,  $3 \times 10^5 < Re < 3.5 \times 10^5$ , known as the critical or the lower transition regime. At one side of the cylinder, the boundary layer turns turbulent at the separation point and it shifts from side to side intermittently. This phenomenon causes asymmetry in the flow behaviour and consequently, non-zero mean lift coefficient on the body since the hydrodynamic force is changing direction (Schewe, 1983). The turbulent boundary layer separation is observed on both sides of the cylinder at  $3.5 \times 10^5 < Re < 1.5 \times 10^6$ , in the supercritical flow regime. However, the boundary layer becomes turbulent in one side of the body in the upper transition regime, in the range of  $1.5 \times 10^6 < Re < 4 \times 10^6$ . When  $Re > 4.5 \times 10^6$ , the flow regime is called the

transcritical regime and the boundary layer is fully turbulent on both sides of the cylinder.

Table 2.1: Flow regimes around a circular cylinder (Sumer and Fredsøe, 2006)

	No separation. Creeping flow.	$Re < 5$
	A fixed pair of symmetric vortices.	$5 < Re < 40$
	Laminar vortex street.	$40 < Re < 200$
	Transition to turbulence in the wake.	$200 < Re < 300$
	Wake completely turbulent. A: Laminar boundary layer separation.	$300 < Re < 3 \times 10^5$ Subcritical
	A: Laminar boundary layer separation. B: Turbulent boundary layer separation; but boundary layer laminar.	$3 \times 10^5 < Re < 3.5 \times 10^5$ Critical (Lower transition)
	B: Turbulent boundary layer separation; but boundary layer partly laminar partly turbulent.	$3.5 \times 10^5 < Re < 1.5 \times 10^6$ Supercritical
	C: Boundary layer completely turbulent at one side.	$1.5 \times 10^6 < Re < 4 \times 10^6$ Upper transition
	C: Boundary layer completely turbulent at two sides.	$4 \times 10^6 < Re$ Transcritical

## 2.2 Turbulent Flow

In most engineering applications, the flow is turbulent. According to Tennekes and Lumley (1972), it is not an easy task to define turbulent flows, but it is possible to establish a list of the main features that can be observed in such flows:

1. Turbulent flows are irregular and characterized by random fluctuations, which makes it difficult to predict the flow pattern based on deterministic methods; yet stochastic approach is necessary.
2. An important feature of turbulent flow is the diffusivity. It exhibits fast mixing and enhanced rates of heat, momentum and mass transfer. Velocity fluctuations, for example, are transferred along the surrounding fluid.
3. Turbulent flows are observed at high Reynolds numbers in which instabilities in the laminar flow start to appear due to the complex interaction between viscous and inertial terms. The inertia force of the flow is dominant.
4. Three-dimensionality is an intrinsic characteristic of turbulent flows. The presence of the vortex stretching mechanism to maintain the vorticity fluctuations cannot be observed in two-dimensional flows.
5. Turbulent flows are dissipative and turbulence decays rapidly if there is no supply of energy. Viscous shear stresses are responsible for dissipating the kinetic energy into internal energy of the fluid.
6. Turbulence can be described by the continuum mechanics, governed by mass and momentum conservation laws. The smallest scale of turbulence is larger than any molecular length scale.
7. Turbulence depends on the flow characteristics, not on the fluid. Thus, the above features of turbulent flows are the same in all fluids since they are not regulated by molecular properties.

## 2.3 Boundary Layer

In the flow around immersed bodies, the thin region close to the body's surface is known as the boundary layer. One of the main features of the flow in this region is that it adheres to the surface of the object, known as the no-slip condition. Prandtl hypothesized that the viscous forces cannot be neglected across the boundary layer thickness,  $\delta$ , in which the flow experiences a rapid velocity transition, from zero at the wall to the free stream velocity magnitude (Kundu et al. 2012). Thus, potential flow theory is no longer valid inside the boundary layer to obtain the velocity field, and Prandtl proposed how Navier-Stokes equations could be simplified within the boundary layer. For a steady, two-dimensional flow, the boundary-layer equations can be written (Kundu et al. 2012) as:

$$\frac{\partial u}{\partial x} + \frac{\partial v}{\partial y} = 0 \quad (2.2)$$

$$u \frac{\partial u}{\partial x} + v \frac{\partial u}{\partial y} = U \frac{dU}{dx} + \nu \frac{\partial^2 u}{\partial y^2} \quad (2.3)$$

where  $u$  and  $v$  are the horizontal and vertical velocity components, respectively, and  $U = u(x, \infty)$  is the free stream velocity. These equations have a parabolic character, so the boundary conditions depend on the upstream information, and the solution can be obtained numerically. The boundary layer thickness  $\delta$ , shown in Figure 2.2, denotes a generic boundary layer thickness which corresponds to the distance from the wall to a wall-normal location where the horizontal velocity  $u$  is 99% of the local free stream velocity  $U_\infty$ .

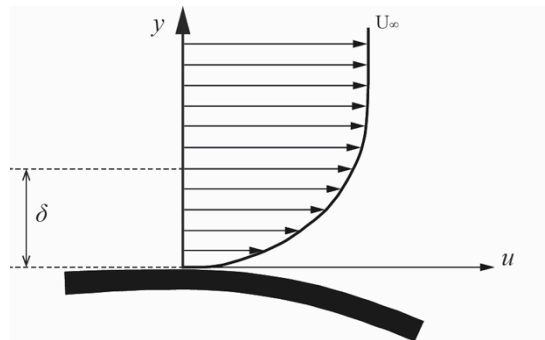


Figure 2.2: Schematic depiction of a velocity profile within the boundary layer

When the pressure gradient changes from favourable to adverse, there is a point where the shear stress is zero, and the flow separates from the wall. Flow separation happens at the so-called separation point (Figure 2.3). From Bernoulli's equation for steady and incompressible flow, and Equation (2.3), one can write:

$$-\rho U \frac{dU}{dx} = \frac{dp}{dx} \quad (2.4)$$

where  $\rho$  is the fluid density and  $p$  denotes the pressure. When the boundary layer equation is evaluated at the surface, where  $u = v = 0$ , Equation (2.3) becomes:

$$\mu \left. \frac{\partial^2 u}{\partial y^2} \right|_{wall} = \frac{dp}{dx} \quad (2.5)$$

where  $\mu$  is the dynamic viscosity of the fluid. Based on Equations (2.4) and (2.5), when there is a positive pressure gradient, the boundary layer flow decelerates, the boundary layer thickness increases, and a point of inflection is created. If this adverse pressure gradient persists over a sufficiently long distance over the surface, backflow close to the wall is generated (Kundu et al. 2012).

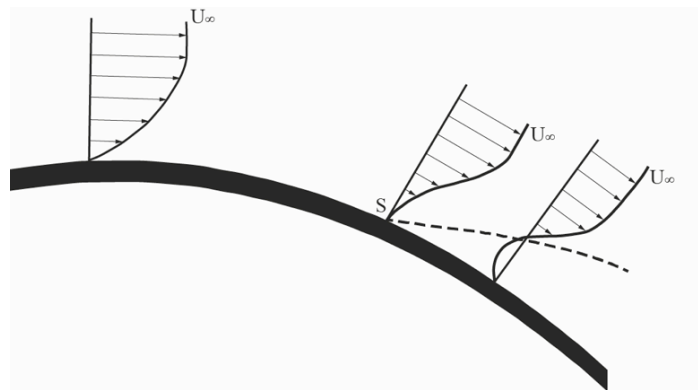


Figure 2.3: Velocity profiles close to the separation point S (Kundu et al. 2012)

### 2.3.1 Turbulent Boundary Layer

As the Reynolds number increases, a transition from laminar to turbulent boundary layer occurs. The Reynolds number at which the transition to turbulence occurs is generally different for different flow cases. It depends on parameters such as wall curvature, surface roughness and local free stream disturbances. Figure 2.4 illustrates the different regions within the boundary layer over a flat plate. The laminar region is characterized by streamlined velocity components. In the transition to the turbulent boundary layer, turbulent eddies appear and the flow becomes unstable. In the turbulent state, the eddies generate fluctuating velocities.

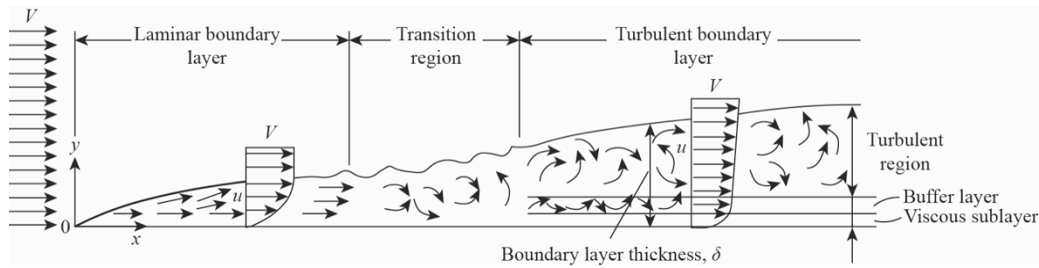


Figure 2.4: Development of the boundary layer along a flat plate (Çengel and Cimbala, 2006)

The turbulent boundary layer can be subdivided into characteristic flow regions. The inner region in which the fluid particles are subjected to the no-slip condition and their velocities are zero is known as the viscous sublayer. It accounts for 10 - 20% of the boundary layer thickness (Versteeg and Malalasekera, 2007). A set of non-dimensional parameters is derived to describe the boundary layer in this region. They are expressed as:

$$U^+ = \frac{U}{u_\tau}, \quad y^+ = \frac{u_\tau y}{\nu}, \quad u_\tau = \sqrt{\frac{\tau_w}{\rho}} \quad (2.6)$$

where  $U^+$  is the dimensionless velocity,  $y^+$  is the dimensionless distance from the surface,  $u_\tau$  is the shear velocity and  $\tau_w$  is the shear stress. The viscous sublayer is

located in the range of  $0 < y^+ < 5$ . The velocity profile close to the wall varies linearly and can be expressed based on the plus units shown in Equation (2.7) as:

$$U^+ = y^+ \quad (2.7)$$

Away from the wall, where  $y^+$  takes values in the range of  $30 < y^+ < 500$ , the effects of viscosity are negligible and the region is known as the log-law region. The velocity profile in this region can be approximated as:

$$U^+ = \frac{1}{\kappa} \ln(y^+) + B \quad (2.8)$$

where  $\kappa = 0.41$  denotes the von Kármán constant and  $B$  is the additive constant which is usually taken as 5.5 for smooth walls (Versteeg and Malalasekera, 2007). Figure 2.5 shows the different velocity profiles usually applied in the inner layer compared with experimental data. Finally, in the buffer region where  $5 < y^+ < 30$ , Equations (2.7) and (2.8) are not applicable.

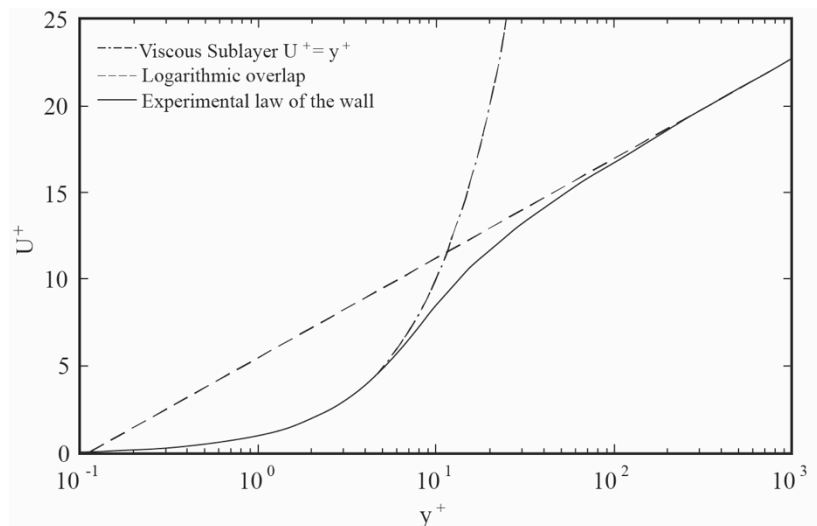


Figure 2.5: Plot of velocity profiles within the turbulent boundary layer



## 2.4 Vortex Shedding

In the external flows around a circular cylinder, the vortex shedding phenomenon is observed at  $Re > 40$ , when the boundary layer separates due to adverse pressure gradient, and the shear layers are released. This mechanism is illustrated in Figure 2.6. The separated shear layers absorb the vorticity from the boundary layer and start to fold into vortices. At both sides of the cylinder, vortices are formed with opposite direction of rotation. They are very unstable, and as a consequence, one becomes larger and stronger than the other, and draws the opposite vortex across the wake. Since the smaller vortex has the opposite vorticity sign, the larger vortex is cut off from the boundary layer and sheds. As a free vortex, it is convected downstream the flow. The smaller vortex keeps on growing and becomes dominant relative to the next vortex that will be formed on the opposite side. The previously described process repeats and the shedding of the vortices occurs alternately behind both sides of the cylinder. Figure 2.6 illustrates the preceding principle.

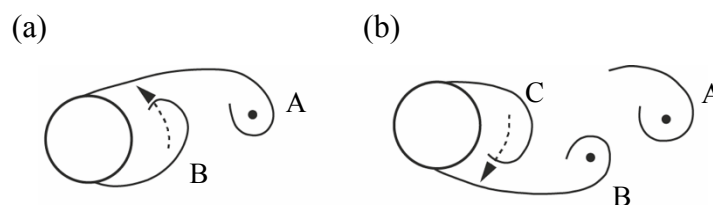
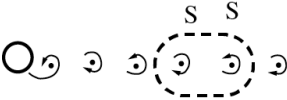
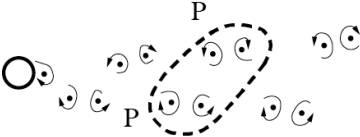
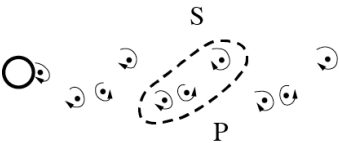
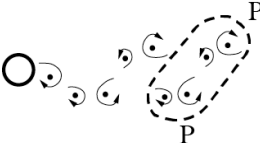
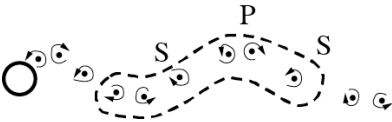
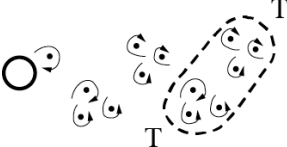



Figure 2.6: Vortex shedding process (Sumer and Fredsøe, 2006)

The vortex shedding mechanism can be observed in many patterns in which the vortices are formed and shed. Table 2.2 shows the classifications of modes according to Williamson and Roshko (1988) and Williamson and Govardhan (2004). In 2S mode, it is observed that a single vortex is shed alternately at each side of the cylinder. A pair of vortices with the same vorticity sign characterizes the 2P mode. In P+S mode, at each cycle, a vortex pair is shed on one side of the cylinder and a single vortex on the opposite side. Similar to 2P mode there is 2Po, in which one of the vortices in the pair is considerably smaller than the other. The 2P+2S mode is formed by pairs of vortices as in 2P, but with singles vortices in between. The 2T mode is

characterized by two triplets of vortices that are shed at each cycle. Compared to 2P, in addition to the vortex pair, there is a third principal vortex. Jauvtis and Williamson (2004) found that this mode is more stable and periodic than 2P. Lastly, in 2C mode it is observed the formation of a doublet of vortices per half cycle.

Table 2.2: Modes of vortex shedding (Williamson and Roshko, 1988 and Williamson and Govardhan, 2004)

Nomenclature	Vortex shedding pattern
2S	
2P	
P+S	
2Po	
2P+2S	
2T	
2C	

## 2.5 Hydrodynamic Forces in Fluid-Structure Interactions

The total force acting on the cylinder can be decomposed into pressure and viscous components. According to Sumer and Fredsøe (2006), an expression for the total forces acting in the in-line and cross-flow directions is obtained by summing the integral of the orthogonal components of the time-averaged pressure and the time-averaged wall shear-stress on the cylinder surface. The force acting in-line is the so-called mean drag force,  $\bar{F}_D$ , and the cross-flow component is known as mean lift force,  $\bar{F}_L$ . When the cylinder is in free flow,  $\bar{F}_L$  is equal to zero due to flow symmetry. When  $Re$  is greater than 40, the vortex shedding mechanism is observed and it causes non-zero instantaneous  $F_L$ .

During the vortex shedding process, the pressure distribution and consequently, the forces around the cylinder undergo a periodic variation. According to Figure 2.7, the resultant force  $F$  points upwards when a vortex is shed at the bottom of the cylinder.

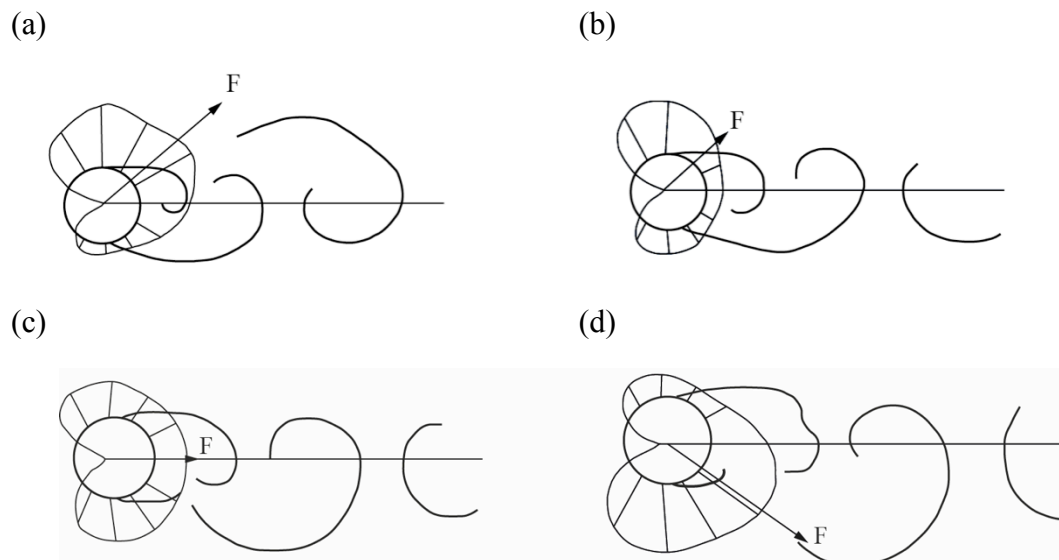


Figure 2.7: Pressure distribution around the cylinder and the total force during vortex shedding (Sumer and Fredsøe, 2006)

The pressure is larger in this region compared with the opposite side. As a vortex is formed on the upper edge of the cylinder, the inverse is observed. The force points

downward and the pressure is higher on the top region. When the pressure distribution changes from upper region to lower region of the cylinder, there is a moment in which zero lift force and reduced drag are observed.

### 2.5.1 Drag and Lift Coefficients

Expressions for the dimensionless drag coefficient,  $\bar{C}_D$ , and the dimensionless lift coefficient,  $\bar{C}_L$ , can be written as:

$$\bar{C}_D = \frac{\bar{F}_D}{\frac{1}{2}\rho DU_\infty^2} \quad (2.9)$$

$$\bar{C}_L = \frac{\bar{F}_L}{\frac{1}{2}\rho DU_\infty^2} \quad (2.10)$$

It can be noted that both formulations are a function of  $Re$ .

### 2.5.2 Pressure and Skin Friction Coefficients

Besides the drag and lift coefficients, two other important dimensionless numbers are the time-averaged pressure and the skin friction coefficients. They are defined, respectively, as:

$$C_p = \frac{p - p_\infty}{\frac{1}{2}\rho U_\infty^2} \quad (2.11)$$

$$C_f = \frac{\tau_w}{\frac{1}{2}\rho U_\infty^2} \quad (2.12)$$

where  $p$  is the static pressure at the angle  $\theta$  measured on the surface of the cylinder, clockwise from the stagnation point,  $p_\infty$  is the static pressure in the free stream and  $\tau_w = \mu \frac{\partial u}{\partial y}$  is the local wall shear stress.

## 2.6 Flow-Induced Vibrations

At Reynolds numbers larger than 40, the vortex shedding mechanism is observed. It causes pressure imbalance between the upper and lower regions of the cylinder and thus, fluctuating hydrodynamic forces. If the cylinder is flexible or elastically supported, these forces induce vibrations. This phenomenon is known as FIV. The two most common types of FIV are VIV and galloping. According to Ding et al. (2018), the first is a self-excited vibration induced by the alternated vortex shedding, and is a self-limiting phenomenon. The latter is mostly influenced by the dynamics of shear layers and is characterized by high amplitudes.

### 2.6.1 Equation of Motion

The motions of an oscillating structure in 1-DoF are described by the dynamic equation of motion:

$$m\ddot{y}(t) + c\dot{y}(t) + ky(t) = 0 \quad (2.13)$$

where  $m$  is the total mass of the system,  $c$  is the damping coefficient,  $k$  is the spring coefficient,  $\ddot{y}(t)$  is the acceleration,  $\dot{y}(t)$  is the velocity and  $y(t)$  is the displacement.

All the terms are in the considered direction of motion. A solution of Equation (2.13) can be written as:

$$y = Ae^{\lambda t} \quad (2.14)$$

where  $A$  and  $\lambda$  are constants which depend on the boundary conditions of the system. Thus, Equation (2.13) assumes the following form:

$$m\lambda^2 + c\lambda + k = 0 \quad (2.15)$$

The two solutions of the quadratic equation are expressed as:

$$\lambda_{1,2} = -\frac{c}{2m} \pm \frac{1}{2m} \sqrt{c^2 - 4km} \quad (2.16)$$

When the term  $c^2 - 4km$  is equal to zero, there is only one solution to Equation (2.16), and it yields the critical damping condition. Correspondingly, the critical damping coefficient,  $c_{cr}$ , can be written as:

$$c_{cr} = 2\sqrt{km} = 2m\omega_n \quad (2.17)$$

where  $\omega_n$  denotes the undamped natural frequency. The dimensionless parameter damping ratio,  $\zeta$ , is defined as:

$$\zeta = \frac{c}{c_{cr}} = \frac{c}{2\sqrt{km}} \quad (2.18)$$

The damping ratio governs the behaviour of the oscillating system. When  $\zeta$  is in the range of  $0 < \zeta < 1$ , the system is underdamped, for  $\zeta > 1$ , the system is overdamped, and it is critically damped if  $\zeta = 1$ .

In the case of a structure vibrating with 2-DoF, the equation of motion can be written to represent the dynamics in  $x$  and  $y$  directions. The equations can be expressed in the following forms:

$$m\ddot{x}(t) + c_x\dot{x}(t) + k_x x(t) = F_x(t) \quad (2.19)$$

$$m\ddot{y}(t) + c_y\dot{y}(t) + k_y y(t) = F_y(t) \quad (2.20)$$

where  $F_x$  is the force in the  $x$  direction and  $F_y$  is the force in the  $y$  direction.

## 2.6.2 Added Mass

A moving body submerged in a fluid flow is subjected to an external force due to its motion. The disturbed fluid exerts a force on the structure that is in phase with the relative acceleration between the body and the fluid, and is known as the added mass force. In the case of an object vibrating in fluid, this force is accounted in the equation of motion as follows:

$$(m + m_a)\ddot{x} + c\dot{x} + kx = F_x \quad (2.21)$$

where the hydrodynamic added mass is denoted by  $m_a$  and the mass of the structure in vacuum is  $m$ . Accordingly, the natural frequency of the system,  $\omega_n$ , can be expressed as:

$$\omega_n = \sqrt{\frac{k}{m + m_a}} \quad (2.22)$$

## 2.6.3 Strouhal Number

For a stationary cylinder, the frequency at which the lift force oscillates is considered to be the same as the vortex-shedding frequency,  $f_{st}$ . When normalized by the cylinder diameter,  $D$ , and free stream flow velocity,  $U$ , it gives the Strouhal number:

$$St = \frac{f_{st} D}{U} \quad (2.23)$$

where  $f_{st}$  is the vortex shedding frequency of a static body.  $St$  expresses the ratio between local flow velocity to average flow velocity and is dependent on the Reynolds number. Figure 2.8 illustrates how  $St$  changes as a function of  $Re$ . When  $Re = 40$ ,  $St$  is taken at approximately 0.1. From  $Re = 300$ ,  $St$  increases to 0.2 and remains approximately constant in the subcritical regime.  $St$  experiences a rapid increase in the critical regime. During the transition from laminar to turbulent boundary layer, the separation points move downstream the cylinder and as a consequence, the vortex shedding occurs at a higher frequency. In the upper transition and transcritical regimes,  $St$  is approximately in the range of 0.25 – 0.30.

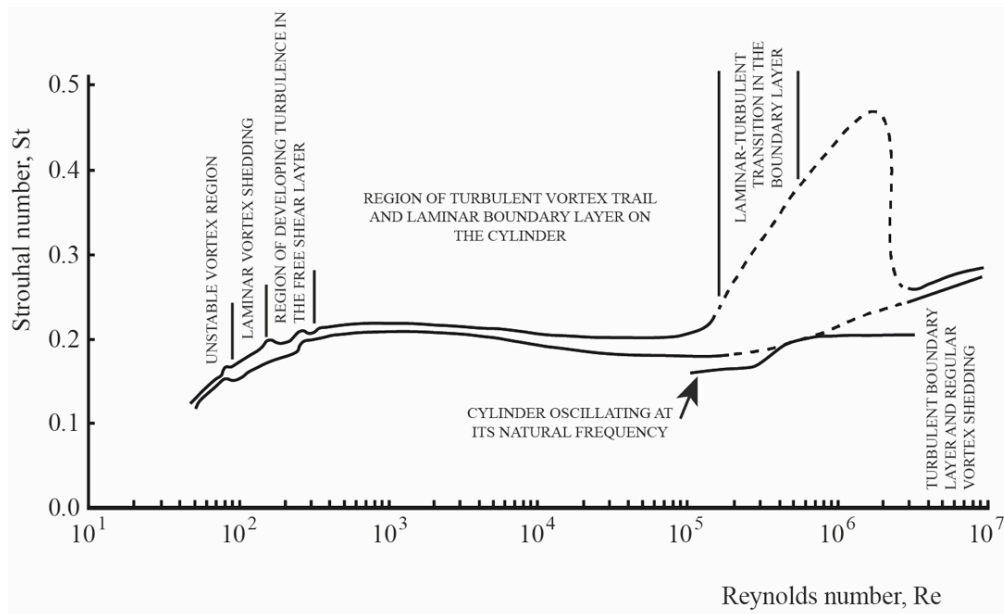


Figure 2.8: Strouhal number dependency with the Reynolds number (Lienhard, 1966)



### 2.6.4 Reduced Velocity

The dimensionless reduced velocity is the ratio of the free stream flow velocity  $U_\infty$  to the natural frequency  $f_n$  (of a system immersed in a fluid), normalized by the cylinder diameter,  $D$ . The reduced velocity can be expressed as:

$$U_r = \frac{U_\infty}{f_n D} \quad (2.24)$$

It should be noted that the ratio  $U_\infty/f_n$  represents the length of vibration path of a vibrating object in a fluid flow.

### 2.6.5 Mass Ratio

The dimensionless mass ratio denotes the ratio of the mass of the oscillating cylinder to the mass of displaced fluid, and is defined as:

$$m^* = \frac{m}{\rho \pi \frac{D^2}{4} L} \quad (2.25)$$

where  $L$  is the characteristic length of the cylinder. The value of  $m^*$  indicates the relative importance of buoyancy and added mass effects on the body. Moreover,  $m^*$  expresses how prone is the structure to VIV. Structures with low mass ratio are more susceptible to resonance over a large range of  $U_r$ .

### 2.6.6 Amplitude Ratio

The dimensionless amplitude ratio represents the vibration amplitude,  $A$ , normalized by the diameter of the cylinder,  $D$ , and can be expressed as:

$$\frac{A_i}{D} \quad (2.26)$$

where  $i = x, y$  are the in-line and cross-flow directions, respectively. The motion amplitude varies with  $U_r$  as shown in Figure 2.9. The response amplitude is

characterized by a hysteresis behaviour which consists in jumps of the vibration amplitude as  $U_r$  is varied. According to Khalak and Williamson (1999), for low mass-damping structures, three distinct branches of response can be observed, i.e. initial, upper and lower. When  $U_r$  is increased, discontinuities are observed in the maximum  $A_y$  response of the cylinder. From initial to upper branch, the transition is hysteretic, and between upper and lower branches, the switching is intermittent. During the transition between the branches, phase shifts occur between the dynamics of the cylinder and the exciting force. These influence not only the branch jumps, but also the interaction of transverse and in-line vibrations.

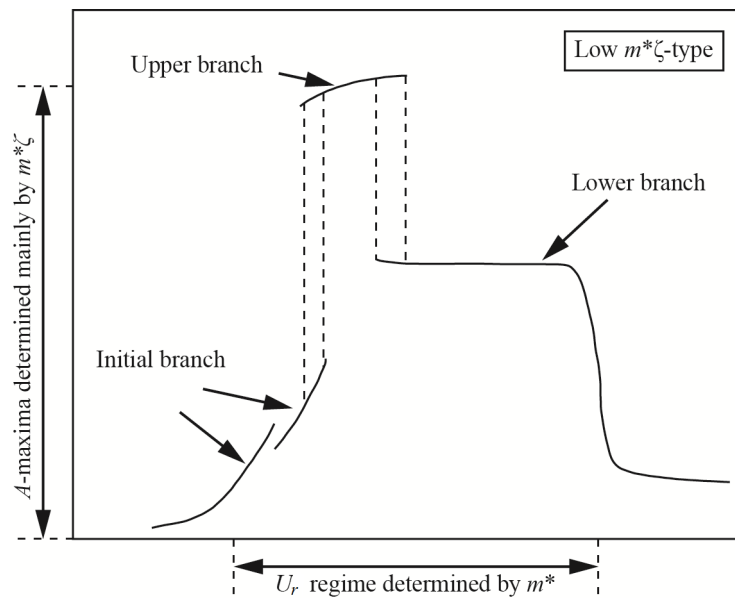


Figure 2.9: Response amplitude of a low mass-damping system (Khalak and Williamson, 1999)

### 2.6.7 Lock-in

The lock-in phenomenon occurs due to the synchronization between the vortex shedding frequency,  $f_{vs}$ , and the natural frequency,  $f_n$ , of the oscillating system when they approach a common value. Accordingly, the cylinder starts to vibrate at an oscillation frequency,  $f_{osc}$ . Over a certain range of reduced velocities,  $f_{vs}$  locks on to  $f_{osc}$  and large amplitude oscillations are observed. The frequency lock-in is

represented in Figure 2.10 and can be observed when the reduced velocity is in the range of  $5 < U_r < 8$ . During this process, the flow velocity and amplitude ratio play an important role. As  $U_r$  increases, the system receives energy from vortex shedding which leads to increase in oscillation amplitude (Figure 2.9). The response amplitude reaches its maximum value when energy equilibrium is achieved, and the system is in lock-in. A further increase in  $U_r$  causes the vortex shedding frequency  $f_{vs}$  to desynchronize with the oscillation frequency  $f_{osc}$ , and lock-in terminates.

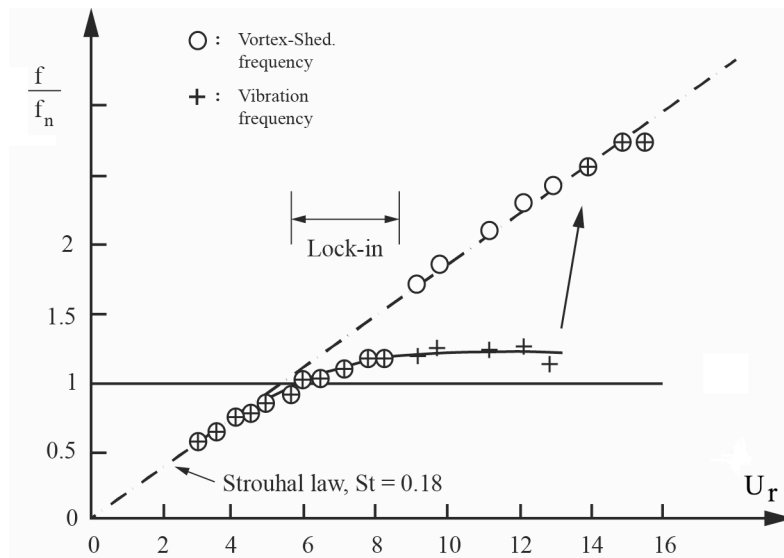


Figure 2.10: Experimental response frequency of a submerged oscillating cylinder (Sumer and Fredsøe, 2006)

## Chapter 3

### Numerical Method

#### 3.1 Computational Fluid Dynamics

##### 3.1.1 Introduction

Computational science has expanded and become popular due to its capability of providing results with acceptable accuracy and low cost, when compared with experimental analysis. Among the computational tools is Computational Fluid Dynamics (CFD), an increasingly reliable approach to perform different flow analyses. There are distinct numerical techniques in CFD which can be employed to simulate the flow and solve the Navier-Stokes equations. In the case of turbulent flows, examples of the available methods are: Direct Numerical Simulation (DNS), Large Eddy Simulation (LES) and Reynolds-Averaged Navier-Stokes (RANS). In the present study, high Reynolds number flows are investigated. Hence, RANS approach in conjunction with turbulence modelling is employed due to its reduced computational cost compared with DNS and LES methods.

##### 3.1.2 OpenFOAM

OpenFOAM (Open Field Operation And Manipulation) is an object-oriented library written in the C++ programming language, used to perform numerical simulations within the continuum mechanics. OpenFOAM code is based on Finite Volume Method (FVM). Besides, it is an open source CFD software adopted by both the academia and the industry.

The use of OpenFOAM involves three main steps: pre-processing, solving and post-processing. Pre-processing consists in setting up appropriately the text files contained in the case directories and defining the computational domain. Solving implies running the simulation using a suitable solver. Finally, in post-processing, the generated simulation data is analysed numerically and graphically. All the information related to the simulation is stored in the case directory. An example of the structure of a case directory is given in Figure 3.1. Accordingly, the 0 folder stores the information necessary to initialize the flow simulation. It is where the boundary conditions and initial values of the pressure field  $p$ , the mesh motion `pointDisplacement` and the velocity field  $U$  are defined. In the `constant` directory, data related to the mesh and choice of turbulence model are stored. The `polymesh` folder contains the settings of the grid. The `dynamicMeshDict` defines the patches and area of the mesh which are morphed by the mesh motion solver, and in the `turbulenceProperties` the properties of turbulence model are specified. Lastly, the `system` directory stores the `controlDict` text file in which the time step and total simulation time are defined, the `fvSchemes`, which contains the selected discretization schemes, and the `fvSolutions`, where the numerical solvers are defined.

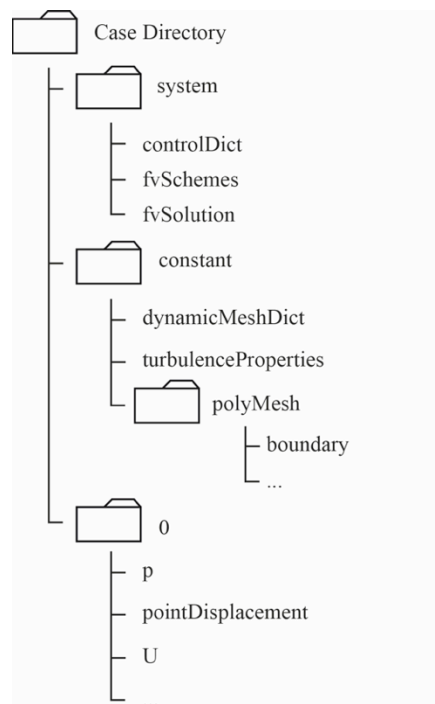


Figure 3.1: OpenFOAM case directory structure

## 3.2 Governing Equations

### 3.2.1 Conservation of Mass and Momentum

The flow investigated in the present study is considered to be incompressible and viscous. The incompressibility condition holds true because the Mach number ( $Ma = U/c$ , where  $U$  is the flow velocity and  $c$  is the speed of sound) is low for the studied flow ( $Ma < 0.3$ ), so compressibility effects are negligible and the fluid density remains constant. Besides, the flow is governed by the continuity equation and the so-called Navier-Stokes equations. Thus, from the conservation of mass, the continuity equation can be written as:

$$\frac{\partial u}{\partial x} + \frac{\partial v}{\partial y} = 0 \quad (3.1)$$

where  $x$  and  $y$  denote the in-line and cross-flow directions, respectively, and  $u$  and  $v$  are the corresponding velocity components. The  $x$ - and  $y$ -components of the Navier-Stokes momentum equation are given as follows:

$$\frac{\partial u}{\partial t} + u \frac{\partial u}{\partial x} + v \frac{\partial u}{\partial y} = -\frac{1}{\rho} \frac{\partial p}{\partial x} + \nu \left( \frac{\partial^2 u}{\partial x^2} + \frac{\partial^2 u}{\partial y^2} \right) + f_x \quad (3.2)$$

$$\frac{\partial v}{\partial t} + u \frac{\partial v}{\partial x} + v \frac{\partial v}{\partial y} = -\frac{1}{\rho} \frac{\partial p}{\partial y} + \nu \left( \frac{\partial^2 v}{\partial x^2} + \frac{\partial^2 v}{\partial y^2} \right) + f_y \quad (3.3)$$

where  $p$  denotes the pressure, and  $f_x$  and  $f_y$  represent body forces acting in  $x$  and  $y$  directions, respectively.

### 3.2.2 Reynolds-Averaged Navier-Stokes Equations

Turbulent flows are characterized by random velocity fluctuations and motions with a large range of length and time scales. The largest scales are associated with the mean flow and it is in the smallest scales where dissipation occurs. The full spectrum of turbulent scales is accounted by the Navier-Stokes equations, and it can be costly to fully solve them numerically. Therefore, there are distinct numerical methods available in CFD which are employed to model turbulence and solve the momentum equations. Direct Numerical Simulation solves instantaneous Navier-Stokes equations, resolving all length scales without the use of any models. The computer requirements of DNS are extremely high, and increase rapidly with the Reynolds number. Large Eddy Simulation employs a spatial filtering operation in which the large eddies are separated from the small ones. In the LES methodology, the large-scale motions are resolved and the small ones are modelled. The Reynolds-Averaged Navier-Stokes approach consists in averaging the flow quantities and modelling the effects of instantaneous turbulent motion. Reynolds decomposition is used to separate instantaneous flow variables into mean and fluctuating values (Figure 3.2). Accordingly, expressions for the velocity and pressure fields are written, respectively, as:

$$\tilde{u}_i = U_i + u'_i \quad (3.4)$$

$$\tilde{p} = P + p' \quad (3.5)$$

where  $i, j = 1, 2$  are the streamwise and cross-stream directions, respectively;  $\tilde{u}_i$  denotes the instantaneous velocity,  $U_i$  is the average flow velocity and  $u'_i$  is the fluctuating term associated with the velocity. In Equation (3.5),  $\tilde{p}$  represents the instantaneous pressure,  $P$  is the mean pressure and  $p'$  is the fluctuating component of pressure. Thus, the mean and fluctuating terms are substituted in the governing

equations of the flow and this yields the Reynolds averaged equations of motion, given by:

$$\frac{\partial U_i}{\partial x_i} = 0 \quad (3.6)$$

$$\frac{\partial U_i}{\partial t} + U_j \frac{\partial U_i}{\partial x_j} = -\frac{1}{\rho} \left( \frac{\partial P}{\partial x_i} \right) + \nu \frac{\partial^2 U_i}{\partial x_j^2} - \frac{\partial \overline{u_i' u_j'}}{\partial x_j} \quad (3.7)$$

where the term  $\overline{u_i' u_j'}$  represents the Reynolds stress tensor. Based on the Boussinesq eddy viscosity assumption, the Reynolds stress tensor is expressed by:

$$\overline{u_i' u_j'} = \tau_{ij} = \nu_t \left( \frac{\partial U_i}{\partial x_j} + \frac{\partial U_j}{\partial x_i} \right) - \frac{2}{3} k \delta_{ij} \quad (3.8)$$

where  $\nu_t$  denotes the turbulent viscosity,  $k$  represents the turbulent kinetic energy and  $\delta_{ij}$  is the Kronecker delta. There are different turbulence models to treat the unknown variables in the time-averaged momentum equations. They are classified based on the number of transport equations they introduce which ranges from zero (e.g. the Mixing length model), up to seven (e.g. the Reynolds Stress Model). The present study employs the  $k - \omega$  Shear Stress Transport (SST) model.

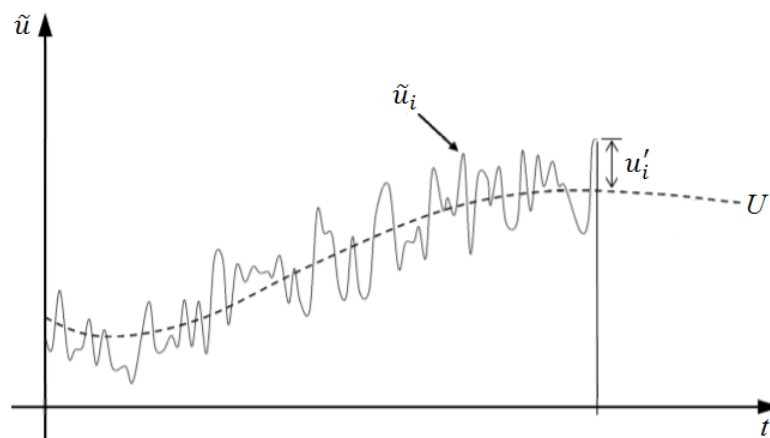


Figure 3.2: Graphical representation of Reynolds decomposition to velocity field



### 3.3 Finite Volume Method

The Finite Volume Method is employed in OpenFOAM to obtain the numerical solution of the partial differential equations describing the fluid flow. According to Schäfer (2006), the methodology of FVM consists firstly, in the decomposition of the computational domain into subdomains, or control volumes (CVs). Accordingly, for each CV, the equations are formulated based on an integral balance as shown in Equation (3.9) for a generic unknown variable  $\phi$ .

$$\frac{\partial}{\partial t} \left( \int_{CV} \rho \phi dV \right) + \int_A \mathbf{n} \cdot (\rho \phi \mathbf{u}) dA = \int_A \mathbf{n} \cdot (\Gamma_\phi \nabla \phi) dA + \int_{CV} S_\phi dV \quad (3.9)$$

$V$  denotes the volume,  $A$  is the surface,  $\Gamma_\phi$  represents a diffusive term associated with  $\phi$  and  $S_\phi$  expresses a source term associated with  $\phi$ . The integrals are approximated based on numerical integration, and the functions values and derivatives, on interpolation of the nodal values. Finally, the system of algebraic equations is solved iteratively.

#### 3.3.1 Spatial Discretization

In the first step of FVM, the domain is discretized into a finite number of control volumes. Figure 3.3 shows an example of a CV built around a generic grid node  $P$ .

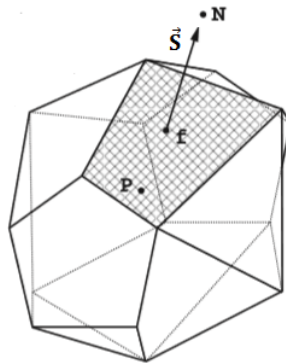


Figure 3.3: Generic representation of a control volume (Jasak, 1996)

The centroid of the CV is where the calculated information of the variables is stored. Besides,  $f$  denotes the centre of the face,  $N$  is the centroid of a neighbouring volume and  $\vec{S}$  is the surface vector. Accordingly, expressions for the centroids  $P$  and  $f$  are given by Equation (3.10).

$$\int_{V_P} (x - x_P) dV = 0, \quad \int_{S_f} (x - x_P) dS = 0 \quad (3.10)$$

Interpolation schemes are used to compute the quantities on the cell faces. The present study employs second order accurate linear interpolation scheme, which can be expressed for a generic scalar  $\phi$  as:

$$\phi_f = f_x \phi_P + (1 - f_x) \phi_N \quad (3.11)$$

where the linear interpolation factor  $f_x$  is expressed by:

$$f_x = \frac{|x_f - x_N|}{|x_f - x_N| + |x_f - x_P|} \quad (3.12)$$

Moreover, a computational domain is classified as structured or unstructured. Figure 3.4 shows an example of each type of mesh. Structured meshes are characterized by

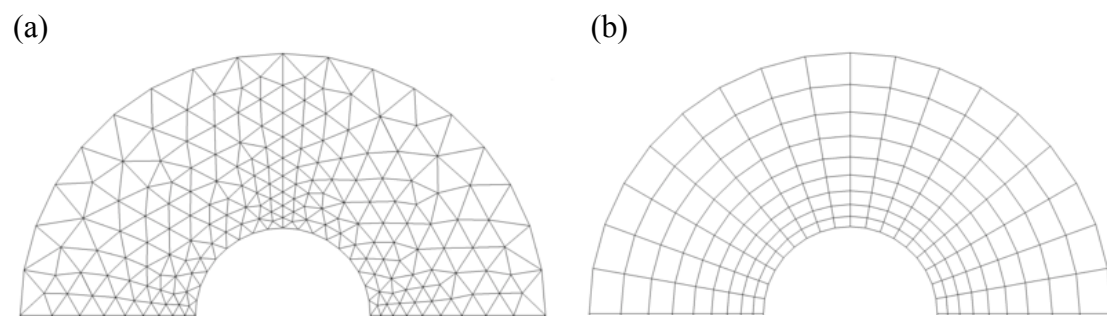


Figure 3.4: Example of unstructured (a) and structured (b) meshes

quadrilateral elements, in 2D domains, or hexahedral cells in 3D domains. On the other hand, unstructured meshes can be formed by cells with any shape, such as triangular and quadrilateral, in 2D domains, or tetrahedral, pyramids and hexahedra,

in 3D domains. Structured meshes are usually employed in regular geometries, while the unstructured type of cells is used to mesh complex geometries.

### 3.3.2 Temporal Discretization

Unsteady flow problems require temporal discretization schemes to define how the field variables are integrated with respect to time. The present study uses the Crank-Nicolson time-stepping scheme which is second order accurate in time and relies on the central differencing method. For a general quantity  $\phi$ , the Crank-Nicolson method can be written as:

$$\phi^{n+1} = \phi^n + \frac{1}{2}[f(t^n, \phi^n) + f(t^{n+1}, \phi^{n+1})]\Delta t \quad (3.13)$$

The face values in the new time-level are dependent on the past and the new time levels, thus a system of equations must be solved for each cell. Moreover, the stability of the solution can be controlled by the dimensionless Courant number. It expresses how fast the flow information transverses a computational grid cell in a given time step and is defined as:

$$Co = \frac{|U|\Delta t}{\Delta x} \quad (3.14)$$

where  $U$  is the flow velocity magnitude,  $\Delta t$  is the time step size and  $\Delta x$  is the computational grid cell size in the direction of the flow.

## 3.4 PIMPLE

In the present study, unsteady Reynolds-Averaged Navier-Stokes equations are solved with the use of the PIMPLE algorithm. The PIMPLE solution procedure consists in

employing the Semi-Implicit Method for Pressure-Linked Equations (SIMPLE) combined with the Pressure-Implicit Split-Operator (PISO). The flowchart for PIMPLE is given in Figure 3.5.

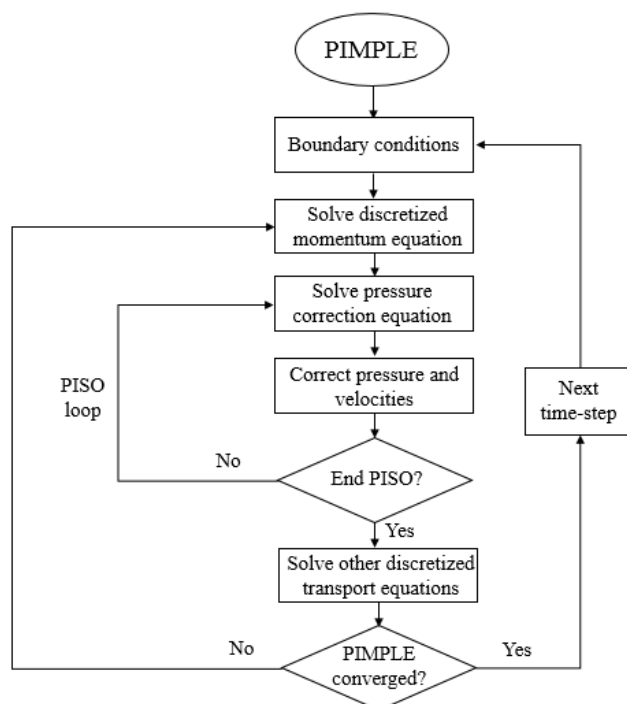


Figure 3.5: PIMPLE algorithm flowchart

PIMPLE is implemented in OpenFOAM and it is the pressure coupling solution of the solver `pimpleFOAM`. The latter is chosen as the solver for the present analysis due to its capability to compute mesh motion.

## 3.5 Turbulence Modelling

### 3.5.1 $k - \omega$ SST Turbulence Model

The  $k - \omega$  SST model (Menter, 1994 and Menter et al. 2003) belongs to the group of two-equation turbulent-viscosity models. It combines the original  $k - \omega$  and the classic  $k - \epsilon$  models. In far field regions of the flow, the  $k - \epsilon$  is activated whereas

$k - \omega$  is applied in wall proximity regions. The expressions for the turbulent kinetic energy  $k$  and the specific dissipation rate  $\omega$  are written as:

$$\frac{Dk}{Dt} = \tilde{P}_k - \beta^* k \omega + \frac{\partial}{\partial x_i} \left[ (\nu + \sigma_k \nu_t) \frac{\partial k}{\partial x_i} \right] \quad (3.15)$$

$$\tilde{P}_k = \min \left[ \nu_t \frac{\partial u_i}{\partial x_j} \left( \frac{\partial u_i}{\partial x_j} + \frac{\partial u_j}{\partial x_i} \right), 10\beta^* k \omega \right] \quad (3.16)$$

$$\frac{D\omega}{Dt} = \alpha S^2 - \beta \omega^2 + \frac{\partial}{\partial x_i} \left[ (\nu + \sigma_\omega \nu_t) \frac{\partial \omega}{\partial x_i} \right] + 2(1 - F_1) \frac{\sigma_{\omega 2}}{\omega} \frac{\partial k}{\partial x_i} \frac{\partial \omega}{\partial x_i} \quad (3.17)$$

where the corresponding constant values are defined in Table 3.1,  $S$  is the strain rate invariant and the expression for the turbulent viscosity  $\nu_t$  is given as:

$$\nu_t = \frac{a_1 k}{\max(a_1 \omega, SF_2)} \quad (3.18)$$

where  $a_1 = 0.31$ . The application of either  $k - \epsilon$  or  $k - \omega$  is determined based on the blending functions  $F_1$  and  $F_2$  and the constant  $\phi$  defined as:

$$\phi = F_1 \phi_1 + (1 - F_1) \phi_2 \quad (3.19)$$

$$F_1 = \tanh \left\{ \left\{ \min \left[ \max \left( \frac{\sqrt{k}}{\beta^* \omega y}, \frac{500\nu}{y^2 \omega} \right), \frac{4k\sigma_{\omega 2}}{CD_{k\omega} y^2} \right] \right\}^4 \right\} \quad (3.20)$$

$$F_2 = \tanh \left\{ \left[ \max \left( 2 \frac{\sqrt{k}}{\beta^* \omega y}, \frac{500\nu}{y^2 \omega} \right) \right]^2 \right\} \quad (3.21)$$

Away from the wall,  $F_1$  tends to zero and  $k - \epsilon$  is gradually activated. On the other hand, the  $k - \omega$  is activated in the viscous sublayer and logarithmic layer, and in this case,  $F_1$  becomes one. Finally, the  $CD_{k\omega}$  denotes the positive portion of the cross-diffusion term and it is defined in Equation (3.22).

$$CD_{k\omega} = \max\left(2\sigma_{\omega^2} \frac{1}{\omega} \frac{\partial k}{\partial x_i} \frac{\partial \omega}{\partial x_i}, 10^{-10}\right) \quad (3.22)$$

Table 3.1: Coefficient values in  $k - \omega$  SST model

$\phi$	$\sigma_k$	$\sigma_\omega$	$\beta^*$	$\beta$	$\alpha$
$\phi_1$	0.85	0.5	0.09	0.075	0.555
$\phi_2$	1	0.856	0.09	0.083	0.44

## Chapter 4

### Numerical Model

#### 4.1 Numerical Set-up

The computational domain employed in the present analyses is shown in Figure 4.1. The domain is defined as a rectangular box with overall size of  $40D \times 20D$ , where  $D$  is the diameter of the large cylinder. The upstream length is set as  $10D$  from the inlet to the centre of the large cylinder, and the downstream length is set as  $30D$  from the centre of the large cylinder to the outlet. In the transverse direction, the domain size extends  $10D$  from the centre of the large cylinder to the top and bottom boundaries, respectively. Ong et al. (2009) used a domain size of  $27D \times 14D$  and reported that such distances to the boundaries show negligible influence on the flow in the vicinity of the body. Thus, the domain size used in the present study is considered to be sufficiently large.

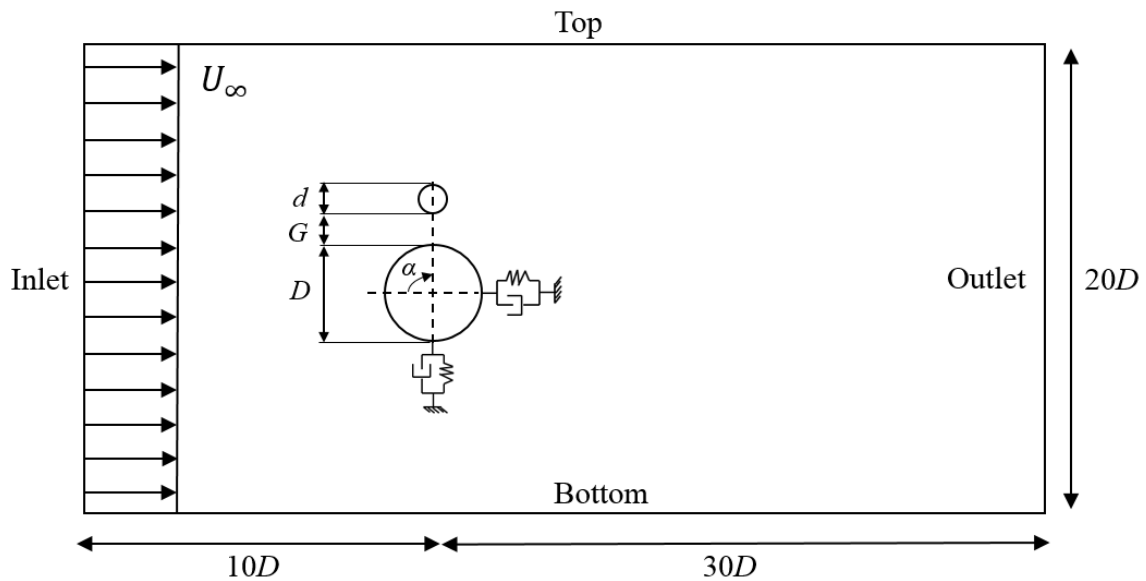


Figure 4.1: Representation of the computational domain

The  $d/D$  value is kept constant throughout the study at  $d/D = 0.25$  which is a typical value for offshore applications. Besides, a similar  $d/D$  was used in the previous works by Zhao et al. (2005), Zang et al. (2012) and Zang et al. (2013). The gap between the cylinders is defined as  $G$  and the position angle of the small cylinder relative to the large cylinder is denoted as  $\alpha$ , as shown in Figure 4.1. The two cylinders are rigidly coupled together so they vibrate as one body. Moreover, they are modelled as one system elastically supported by dampers and springs, and free to experience FIV with 2-DoF. The stiffness of the springs is the same in both the streamwise and transverse directions  $k_x = k_y$ . The mass ratio is set as  $m^* = 2$  and the damping ratio as  $\zeta = 0$  for all the simulations. Thus, this low mass-damping system can reach large displacement amplitudes.

The imposed boundary conditions are given as follows:

1. Uniform flow with  $u_x = U_\infty$  and  $u_y = 0$  is prescribed at the inlet. The inlet values for  $k$  and  $\omega$  are specified based on the following expressions:

$$k = \frac{3(U_\infty I)^2}{2} \quad (4.1)$$

$$\omega = \frac{\sqrt{k}}{l} \quad (4.2)$$

where the turbulence intensity  $I$  is set as 1% and the turbulent length scale  $l$  as  $D$ .

2. At the outlet, zero gradient condition is imposed for  $u_x$ ,  $u_y$ ,  $k$  and  $\omega$ . The pressure is set to zero.
3. On the cylinders walls, the no-slip condition is applied with  $u_x = u_y = 0$ . For  $k$  and  $\omega$ , standard wall functions are specified as:

$$k = \frac{u_*^2}{\sqrt{C_\mu}} \quad (4.3)$$



$$\omega = \frac{\sqrt{k}}{\sqrt[4]{C_\mu \kappa h_p}} \quad (4.4)$$

where  $u_*$  denotes the friction velocity, the model constant is  $C_\mu = 0.09$ , the von Kármán constant is  $\kappa = 0.41$  and  $h_p$  denotes the radial length between the cylinders surface and the centre of the first cell adjacent to the cylinders surface.

4. At top and bottom boundaries, zero normal gradient is prescribed for  $u_x$ ,  $u_y$ , pressure,  $k$  and  $\omega$ .

## 4.2 Convergence Studies

The convergence studies are performed in two steps. Firstly, mesh and time step dependence studies are carried out for a single cylinder. In this step, a series of simulations of a stationary cylinder is conducted to investigate the necessary mesh density to accurately model the flow around the cylinder and in the wake region. New simulations are then performed for a vibrating single cylinder using the same set of grid resolution from the simulations of the stationary cylinder. In this case, due to the motion solver, the mesh is deformed during the simulations, and as a consequence the size of the cells can vary significantly in some regions of the domain. Hence, time step convergence study is also carried out for the case with the vibrating single cylinder to find the maximum Courant number setting that minimizes time step errors.

Secondly, grid convergence study is carried out for two coupled cylinders with  $\alpha = 90^\circ$  and  $G/D = 0.1$  configuration, and free to vibrate with 2-DoF. The selected mesh densities are based on the study carried out for the single cylinder cases. Based on the obtained results, similar grid resolutions are used for the other investigated configurations with two cylinders.

Figure 4.2 presents a complete view of a typical mesh used in the first stage of the convergence studies. The domain is composed of structured hexahedral elements. A high refinement is applied in the region around the cylinder and in the cylinder's

wake. In the far field, the mesh is coarsened in order to reduce the computational cost. In Figure 4.3, detailed views of the mesh around the cylinder are shown. The first cell height near the surface of the cylinder is set as  $0.0005D$  which yields approximately averaged  $y^+$  (here  $y^+ = h_p u_* / \nu$ ) values in the range of  $30 - 40$  which is appropriate for the use of wall function.

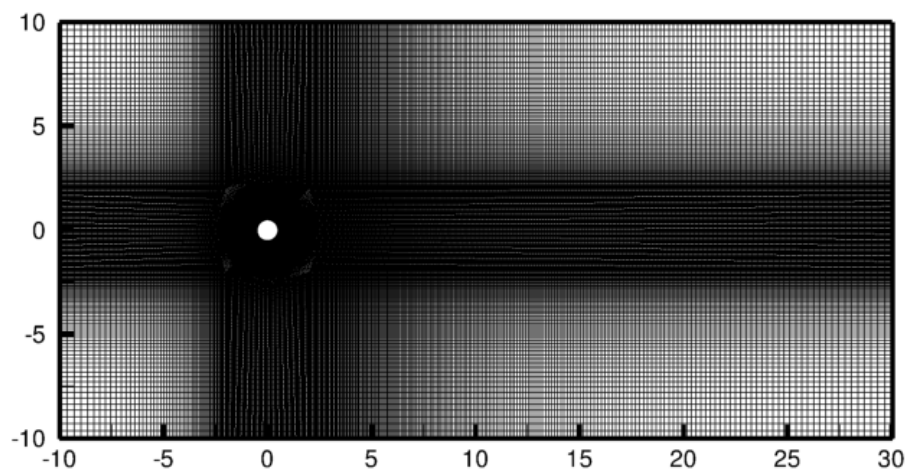


Figure 4.2: Computational mesh for the single cylinder cases: mesh A3 (Table 4.1), 104536 cells

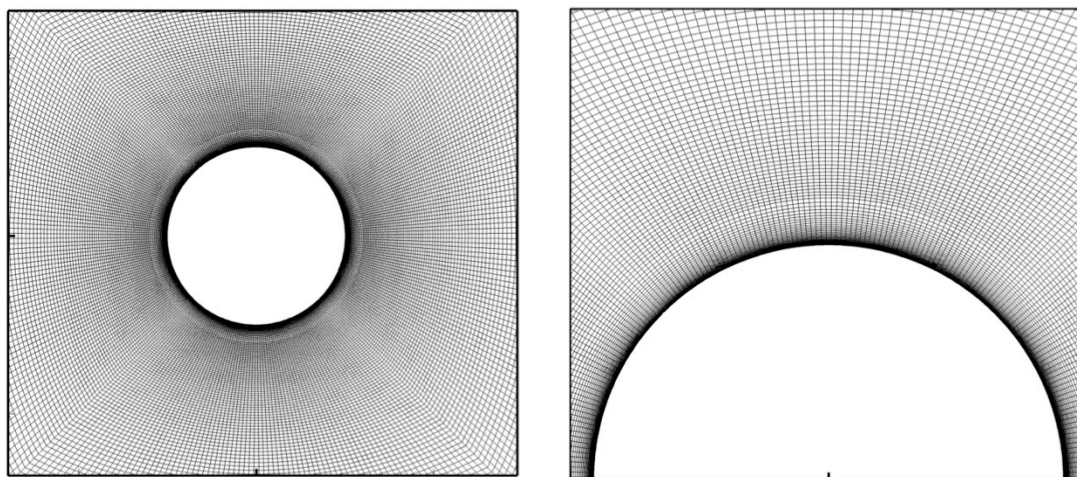


Figure 4.3: Mesh details around the cylinder for the single cylinder cases

For the simulations with the stationary cylinder, hydrodynamic force coefficients and the Strouhal number are used to evaluate the convergence. OpenFOAM has the built-

in function object `forceCoeffs` which extracts the hydrodynamic coefficients  $C_D$  and  $C_L$  of the cylinder at each time step. Expressions for the mean drag and mean lift coefficients are given as follows:

$$\bar{C}_D = \frac{1}{n} \sum_{i=1}^n C_{D,i} \quad (4.5)$$

$$\bar{C}_L = \frac{1}{n} \sum_{i=1}^n C_{L,i} \quad (4.6)$$

where  $C_{D,i}$  and  $C_{L,i}$  corresponds to  $C_D$  and  $C_L$  values, respectively, at  $i$ th time step and  $n$  is the total number of time steps averaged.

The corresponding root-mean-square values for the drag and lift coefficients are obtained by:

$$C_{D,rms} = \sqrt{\frac{1}{n} \sum_{i=1}^n (C_{D,i} - \bar{C}_D)^2} \quad (4.7)$$

$$C_{L,rms} = \sqrt{\frac{1}{n} \sum_{i=1}^n (C_{L,i} - \bar{C}_L)^2} \quad (4.8)$$

In the grid resolution test for the stationary single cylinder case, four sets of meshes with an increment of approximately 40% in the total number of elements are assessed. A time step of  $\Delta t = 0.002$  is employed in the simulations keeping the maximum Courant number below 0.60. The total non-dimensional duration of the simulations is set to  $\tau = 200$ , where the dimensionless time is defined as:

$$\tau = \frac{tU_\infty}{D} \quad (4.9)$$

Table 4.1 summarizes the mesh parameters along with the corresponding results for the analysed hydrodynamic quantities. The differences between the results obtained on the meshes A3 and A4 are smaller than 0.5% for  $\overline{C}_D$ ,  $C_{L,rms}$  and  $St$ .

Table 4.1: Mesh convergence study for the stationary single cylinder

Mesh	No. of cells	Time Step	$\overline{C}_D$	$C_{L,rms}$	$St$
A1	53595	$\Delta t = 0.002$	0.4492	0.153	0.3204
A2	74889	$\Delta t = 0.002$	0.4547	0.162	0.3204
A3	104536	$\Delta t = 0.002$	0.4616	0.175	0.3204
A4	146092	$\Delta t = 0.002$	0.4625	0.174	0.3204

In the convergence study of the vibrating single cylinder,  $U_r = 6$  is selected for the simulations where high vibration amplitudes of the cylinder, both in-line and transverse, are expected. In the grid resolution analysis, the maximum Courant number is constrained to  $Co_{max} = 0.5$ . Besides the hydrodynamic force coefficients, displacement amplitudes are also used to compare the results obtained from the simulations. The normalized maximum vertical vibration amplitude is given by:

$$\frac{A_{y,max}}{D} = \frac{1}{2} \frac{|A_{y,max} - A_{y,min}|}{D} \quad (4.10)$$

The mesh settings along with the corresponding results for the analysed parameters are given in Table 4.2. The differences in the calculated  $\overline{C}_D$ ,  $C_{L,rms}$  and  $St$  obtained on the meshes A3 and A4 are smaller than 1%. The  $A_{y,max}/D$  values differ 1.44% between the simulations using the meshes A3 and A4.

In the time step sensitivity analysis, three simulations with the mesh A3 (see Table 4.2) are carried out with different maximum Courant numbers,  $Co_{max} = [0.25, 0.5, 1.0]$ , and the obtained results are presented in Table 4.3. The discrepancies in the observed  $\overline{C}_D$  and  $St$  values between the simulations using  $Co_{max} = 0.5$  and  $Co_{max} = 0.25$  are within 1%. The differences in the calculated

$A_{y,max}/D$  and  $C_{L,rms}$  using  $Co_{max} = 0.25$  compared with the values obtained using  $Co_{max} = 0.5$  are approximately 1.80% and 3.10%, respectively. Thus, based on the convergence studies with the vibrating single cylinder, it is concluded that the mesh A3 with 104536 elements and  $Co_{max} = 0.5$  provides sufficient grid and time step convergence. This setting of mesh and time step is selected for the present simulations of FIV of a single cylinder.

Table 4.2: Mesh convergence study for the vibrating single cylinder

Mesh	No. of cells	Time Step	$\bar{C}_D$	$C_{L,rms}$	$St$	$A_{y,max}/D$
A1	53595	$Co_{max} = 0.5$	1.2848	0.3659	0.4992	1.1701
A2	74889	$Co_{max} = 0.5$	1.3120	0.4728	0.4898	1.2907
A3	104536	$Co_{max} = 0.5$	1.2503	0.5134	0.4844	1.2937
A4	146092	$Co_{max} = 0.5$	1.2529	0.5185	0.4844	1.2751

Table 4.3: Time step convergence study for the vibrating single cylinder

Mesh	No. of cells	Time Step	$\bar{C}_D$	$C_{L,rms}$	$St$	$A_{y,max}/D$
A3	104536	$Co_{max} = 1.0$	1.3188	0.5194	0.5033	1.3274
A3	104536	$Co_{max} = 0.5$	1.2503	0.5182	0.4844	1.3055
A3	104536	$Co_{max} = 0.25$	1.2612	0.4997	0.4844	1.3170

In the grid resolution analyses for the cases with two coupled cylinders, the computational domain is the same as that for the single cylinder cases. It consists of structured hexahedral elements. Figures 4.4 and 4.5 show a typical mesh for  $\alpha = 90^\circ$  and  $G/D = 0.1$  configuration used in the convergence studies. Three meshes with an increment of approximately 40% in the total number of elements are assessed. Similarly to the cases with a single cylinder, the mesh is highly refined close the cylinders, and coarser cells are used in the far-field regions.

In the Table 4.4, the results of the grid sensitivity study for two vibrating coupled cylinders are presented. The maximum Courant number is constrained to 0.5 based on the results obtained from the time step convergence studies with the vibrating single

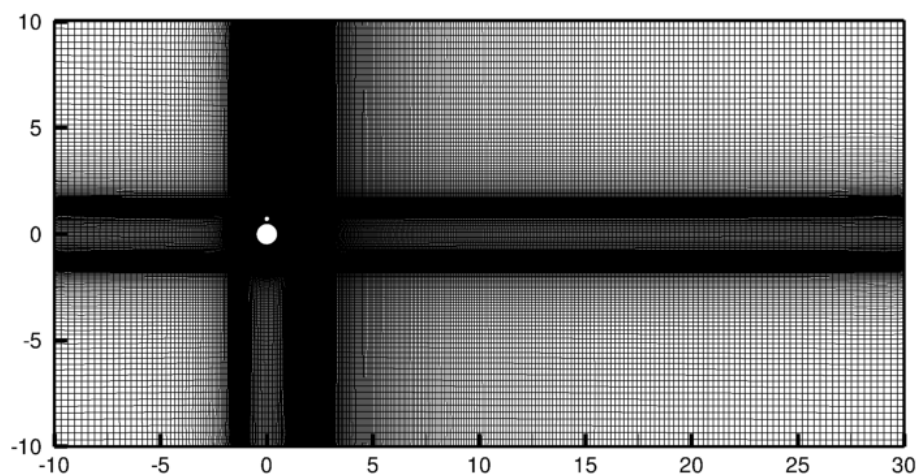


Figure 4.4: Computational mesh for the two coupled cylinders cases with  $\alpha = 90^\circ$  and  $G/D = 0.1$  configuration: mesh B3 (Table 4.4), 114321 cells

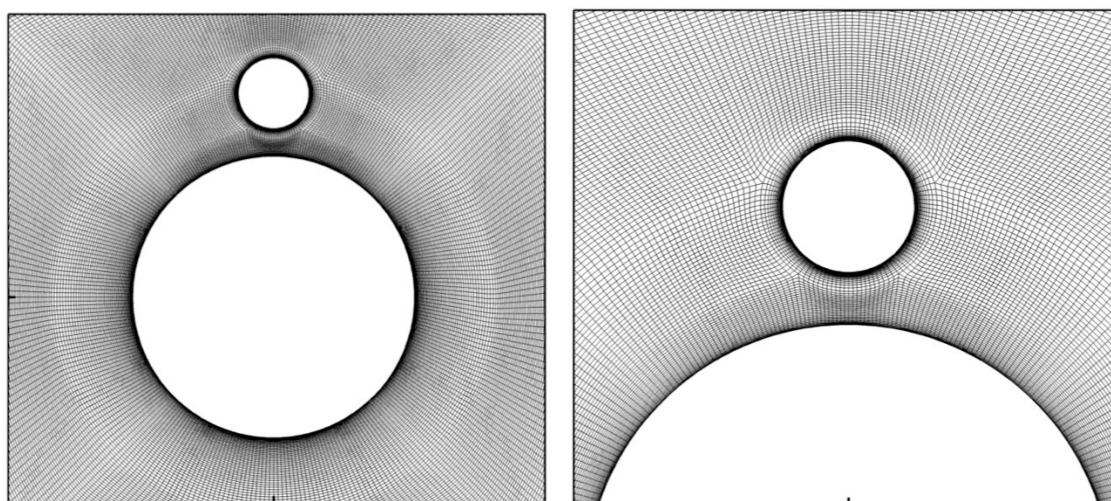


Figure 4.5: Mesh details around the cylinders for the two coupled cylinder cases with  $\alpha = 90^\circ$  and  $G/D = 0.1$  configuration

cylinder (Table 4.3). The reduced velocity  $U_r = 6$  is used in the simulations. At this  $U_r$ , high amplitudes of the cylinder's vibration are expected, facilitating the assessment of the dynamic simulations convergence. Discrepancies in the results between the meshes B2 and B3 are within 1.45% for  $\bar{C}_D$ ,  $C_{L,rms}$  and  $St$ . The deviation in the observed  $A_{y,max}/D$  using the mesh B3 compared to the obtained result using the mesh B2 is 2.38%. Considering that further mesh refinement results in negligible

Table 4.4: Mesh convergence study for the two vibrating rigidly coupled cylinders with  $\alpha = 90^\circ$  and  $G/D = 0.1$  configuration

Large Cylinder						
Mesh	No. of cells	Time Step	$\bar{C}_D$	$C_{L,rms}$	$St$	$A_{y,max}/D$
B1	57833	$Co_{max} = 0.5$	1.6392	0.5218	0.5033	1,4678
B2	80163	$Co_{max} = 0.5$	1.4844	0.5601	0.5033	1,4355
B3	114321	$Co_{max} = 0.5$	1.4808	0.5534	0.5033	1,4013
Small Cylinder						
Mesh	No. of cells	Time Step	$\bar{C}_D$	$C_{L,rms}$	$St$	$A_{y,max}/D$
B1	57833	$Co_{max} = 0.5$	3.1914	1.9453	0.0841	1,4678
B2	80163	$Co_{max} = 0.5$	3.6173	2.0196	0.0841	1,4355
B3	114321	$Co_{max} = 0.5$	3.6290	1.9945	0.0841	1,4013

change of the compared parameters, the mesh B3 is selected for the present simulations of FIV of two coupled cylinders with different  $\alpha$  and  $G/D$ .

### 4.3 Model Validation

The numerical model employed in the present study is validated by comparing the present model predictions with the published experimental and numerical studies in the upper transition regime. The number of published data in the upper transition regime is very limited since the required experimental setup and numerical simulations to reproduce such flows are very complex and expensive. The predicted values of  $\bar{C}_D$ ,  $C_{L,rms}$ ,  $-C_{pb}$  and  $St$  for the single stationary cylinder are compared with previous published results in Table 4.5. Here  $C_{pb}$  is the base pressure coefficient which is the value of  $C_p$  at  $\theta = 180^\circ$ . The predicted  $\bar{C}_D$  shows good agreement with the published numerical results by Catalano et al. (2003) and Ong et al. (2009), and is in the range of values reported by the experimental studies of Roshko (1961) and Achenbach (1968). The present result obtained for  $C_{L,rms}$  differs significantly from the value predicted by Ong et al. (2009). The predicted  $-C_{pb}$  agrees well with the values reported by Porteous et al. (2015). The value of  $St$ , on the other hand, is higher

than the value predicted by Porteous et al. (2015) but close to the value reported by Ong et al. (2009).

Table 4.5: Numerical and experimental data of a single stationary cylinder at high Reynolds number regime

Author	Description	$\bar{C}_D$	$C_{L,rms}$	$-C_{pb}$	$St$
Present study	URANS $k - \omega$ SST $Re = 3.6 \times 10^6$	0.4616	0.175	0.5527	0.3204
Catalano et al. (2003)	URANS $k - \epsilon$ $Re = 4 \times 10^6$	0.46	-	-	-
Ong et al. (2009)	URANS $k - \epsilon$ $Re = 3.6 \times 10^6$	0.4573	0.0766	-	0.3052
Porteous et al. (2015)	URANS $k - \omega$ SST $Re = 3.6 \times 10^6$	0.4206	-	0.495	0.148
Roshko (1961)	Experimental studies $Re = (1 - 3.5) \times 10^6$	0.30 - 0.70	-	0.62 - 0.85	-
Achenbach (1968)	Experimental studies $Re = (1 - 5) \times 10^6$	0.37 - 0.68	-	0.85	-

Figure 4.6 shows the time-averaged pressure distribution and skin friction distribution around the cylinder compared with the experimental data reported by Achenbach (1968) and the numerical results reported by Ong et al. (2009). The time averaged pressure distribution shows very good agreement with the results reported by Ong et al. (2009). Compared with the data reported by Achenbach (1968), it seems that the present model underpredicts  $C_p$  at  $60^\circ < \theta < 80^\circ$  and  $110^\circ < \theta < 180^\circ$ . In Figure 4.8 (b), the skin friction distribution has a satisfactory prediction between the present simulation and the published data by Ong et al. (2009) and Achenbach (1968) for the region of separated flow,  $113^\circ < \theta < 250^\circ$ . The discrepancies observed in the region of attached flow may be explained by the use of wall function in predicting the turbulent flow around a single cylinder. The present model combined with the wall function assumes a fully turbulent boundary layer. However, for  $Re < 4 \times 10^6$  the boundary layer around the cylinder is not fully turbulent yet, especially before the separation point, and there is a transition from laminar to turbulent boundary layer.

Overall, the present numerical model is in good agreement with the published numerical and experimental data.



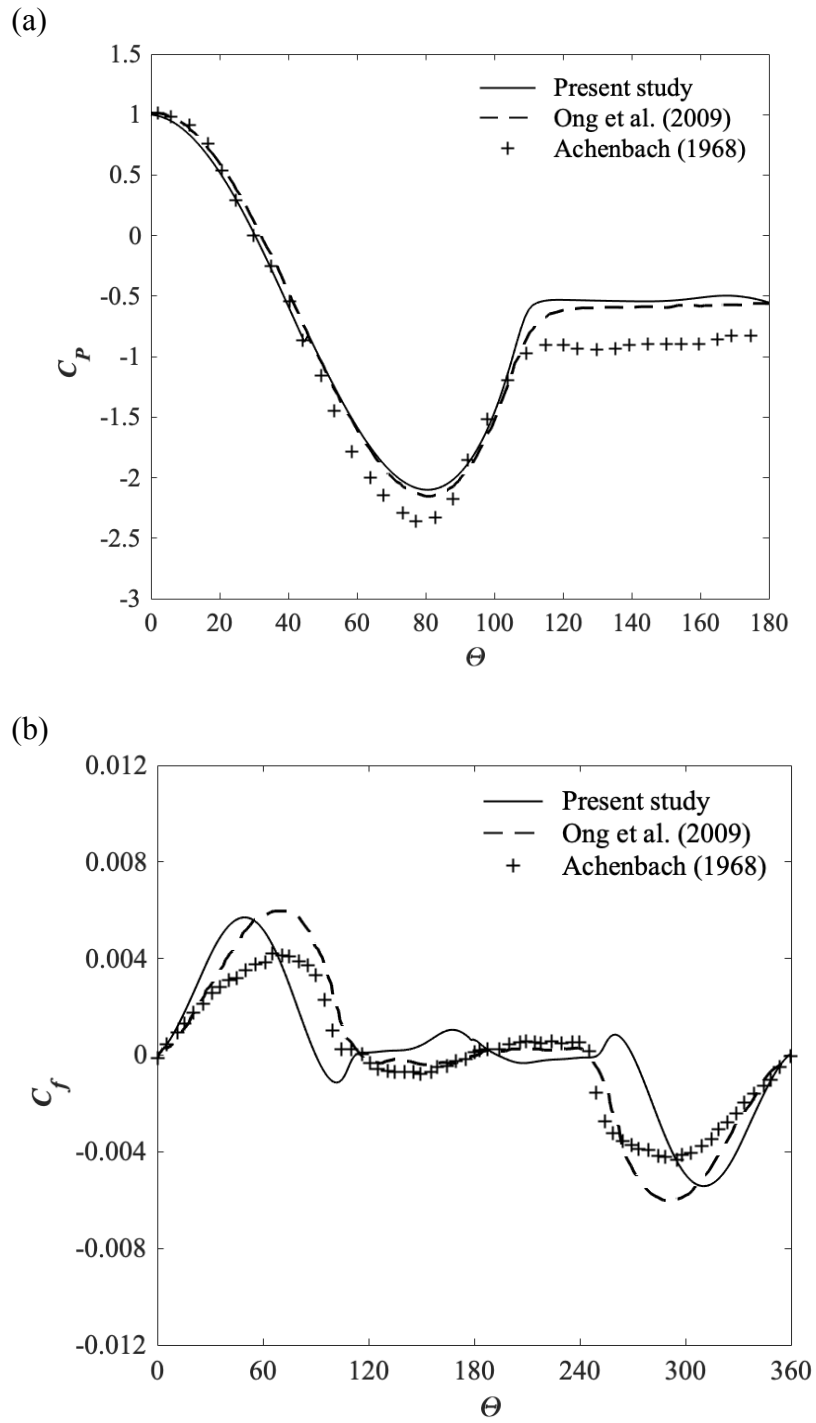


Figure 4.6: Time-averaged pressure distribution (a) and skin friction distribution (b) around the single stationary cylinder at  $Re = 3.6 \times 10^6$

## Chapter 5

# Flow-Induced Vibrations of Two Rigidly Coupled Cylinders at $Re = 3.6 \times 10^6$

### 5.1 Introduction

A parametric study is carried out to investigate the dynamic response of the single cylinder configuration and different configurations of two rigidly coupled cylinders with respect to  $\alpha$ ,  $G/D$  and  $U_r$ . Three values of  $\alpha$  are studied [ $\alpha = 0^\circ, 90^\circ, 180^\circ$ ] at a fixed  $G/D = 0.1$ . For the  $\alpha = 90^\circ$  configuration, two additional  $G/D$  values are studied [ $G/D = 0.25, 0.5$ ]. The simulations are performed for  $2.5 \leq U_r \leq 12$  for the single cylinder configuration. The coupled cylinders configurations are analysed for  $2 \leq U_r \leq 12$ . The time of simulation is sufficiently long in order to capture at least 30 cycles of oscillation when it is regular and periodic. For irregular vibration, the simulation time is extended until statistically stationary state is reached.

### 5.2 Effect of the Position Angle $\alpha$

The effect of  $\alpha$  on the FIV response of two rigidly coupled cylinders is analysed with respect to the hydrodynamic coefficients, vibration amplitude, response frequencies and flow fields. The results obtained from the analysed quantities are compared with those of the single cylinder configuration.

#### 5.2.1 Hydrodynamic Force Coefficients

The hydrodynamic force coefficients of the cylinder bundle and the single cylinder configuration are discussed. For the cases with two cylinders,  $\bar{C}_D$ ,  $\bar{C}_L$ ,  $C_{D,rms}$  and  $C_{L,rms}$  are obtained based on the total force value for both cylinders and their

projected area to the flow direction. Figure 5.1 shows the variation of  $\bar{C}_D$  and  $C_{D,rms}$  with  $U_r$  for the single cylinder configuration and all the investigated  $\alpha$  configurations. It can be seen that the presence of the small cylinder has a strong influence on  $\bar{C}_D$  which has also been reported by Zang and Gao (2014). For the single cylinder configuration, the  $\bar{C}_D$  values are around 1.2 for  $2.5 \leq U_r \leq 6.5$  and tend to decrease for  $U_r > 6.5$ . Compared with the single cylinder configuration, when the small cylinder is placed upstream the large cylinder ( $\alpha = 0^\circ$ ), an increased magnitude of  $\bar{C}_D$  is observed for  $4 \leq U_r \leq 5$  with a peak at  $U_r = 5$ . A decreased magnitude of  $\bar{C}_D$  is observed by placing the small cylinder downstream the large cylinder ( $\alpha = 180^\circ$ ) for  $U_r < 10$ , compared with the single cylinder configuration. For  $U_r \geq 11$ , the values of  $\bar{C}_D$  for the single cylinder and the  $\alpha = 0^\circ$  configurations are similar. The highest values of  $\bar{C}_D$  are observed when the cylinders are vertically aligned ( $\alpha = 90^\circ$ ) for  $4 \leq U_r \leq 6$ .

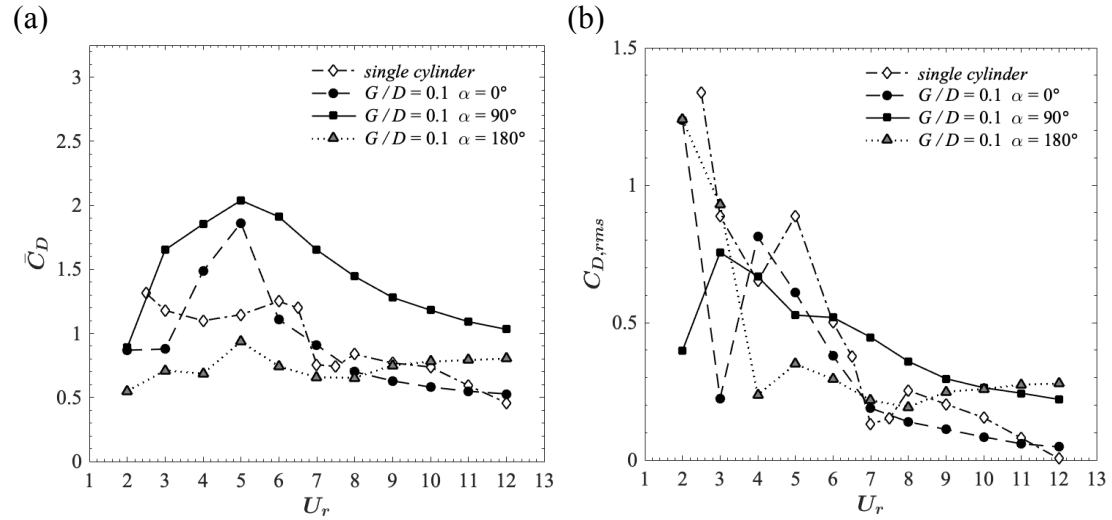


Figure 5.1: Time-averaged drag coefficient  $\bar{C}_D$  (a) and root-mean-square of the drag coefficient  $C_{D,rms}$  (b) for the single cylinder and  $\alpha = [0^\circ, 90^\circ, 180^\circ]$  configurations

The plot of  $C_{D,rms}$  presented in Figure 5.1 (b) shows peak values at low reduced velocities ( $U_r \leq 3$ ) for all the investigated configurations. This is characteristic of in-line lock-in. The highest peak in  $C_{D,rms}$  is observed for the single cylinder configuration at  $U_r = 2.5$  and it is followed by a sharp decrease with increasing  $U_r$ . Similar behaviour is observed for the  $\alpha = 0^\circ$  and  $\alpha = 180^\circ$  configurations, where a

peak in  $C_{D,rms}$  is observed at  $U_r = 2$  for both configurations. The  $\alpha = 90^\circ$  configuration has the lowest peak in  $C_{D,rms}$  observed at  $U_r = 3$ , and it is followed by a monotonic decrease.

Figure 5.2 shows  $\bar{C}_L$  and  $C_{L,rms}$  against  $U_r$  for the single cylinder configuration and different  $\alpha$  configurations. As expected,  $\bar{C}_L$  is approximately zero in the configurations characterized by geometric symmetry aligned with the flow direction (single cylinder,  $\alpha = 0^\circ$ ,  $\alpha = 180^\circ$ ). For the  $\alpha = 90^\circ$  configuration, the effect of the small cylinder on  $\bar{C}_L$  is significant. Positive values of  $\bar{C}_L$  are observed for  $4 \leq U_r \leq 10$  with a peak at  $U_r = 5$ , and negative values of  $\bar{C}_L$  are found for  $U_r \leq 3$  and  $U_r \geq 11$ .

The peak values of the  $C_{L,rms}$  response curve for the single cylinder,  $\alpha = 0^\circ$  and  $\alpha = 90^\circ$  configurations are found for  $U_r \leq 5$ , and a sudden decrease occurs with increasing  $U_r$ . The  $C_{L,rms}$  curve for the  $\alpha = 180^\circ$  configuration shows less variability in the range of studied  $U_r$ , compared with the other configurations. Also, for  $6 \leq U_r \leq 12$ , the observed  $C_{L,rms}$  values for the  $\alpha = 180^\circ$  cases are higher than those for the other configurations.

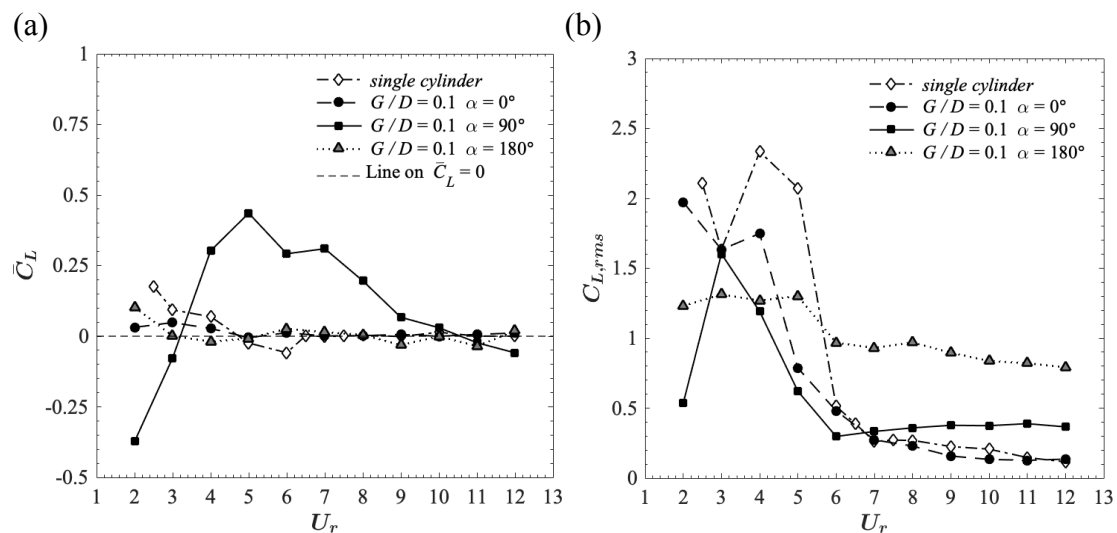


Figure 5.2: Time-averaged lift coefficient  $\bar{C}_L$  (a) and root-mean-square lift coefficient  $C_{L,rms}$  (b) for the single cylinder and  $\alpha = [0^\circ, 90^\circ, 180^\circ]$  configurations

## 5.2.2 Amplitude Response

The variation of  $A_{y,max}/D$  and the root-mean-square of the in-line vibration amplitude  $A_{x,rms}/D$  with  $U_r$  is presented in Figure 5.3. The expression for the normalized root-mean-square of the in-line vibration amplitude is given by:

$$\frac{A_{x,rms}}{D} = \frac{\sqrt{\left[\sum_{i=1}^n (A_{x,i} - \bar{A}_x)^2\right]/n}}{D} \quad (5.1)$$

Based on the plot of  $A_{y,max}/D$ , the lock-in regime of the single cylinder configuration is observed in the range of  $2.5 \leq U_r \leq 11$  with a peak value of approximately  $A_{y,max}/D = 1.52$  at  $U_r = 8$ . The lock-in regime of the three investigated  $\alpha$  configurations extends beyond the studied range of  $U_r$ . For the  $\alpha = 0^\circ$  configuration, the peak of  $A_{y,max}/D = 1.26$  occurs at  $U_r = 5$  and the lock-in starts at  $U_r = 2$ .

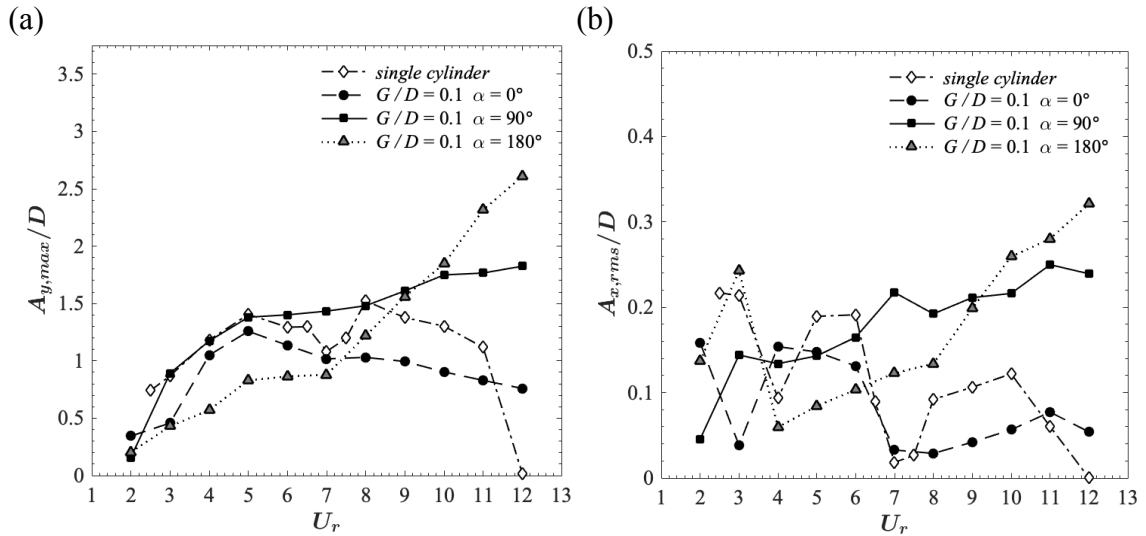


Figure 5.3: Normalized maximum cross-flow vibration amplitude  $A_{y,max}/D$  (a) and normalized root-mean-square of the in-line vibration amplitude  $A_{x,rms}/D$  (b) for the single cylinder and  $\alpha = [0^\circ, 90^\circ, 180^\circ]$  configurations

For the  $\alpha = 90^\circ$  and  $\alpha = 180^\circ$  configurations,  $A_{y,max}/D$  values increase monotonically over the range of investigated  $U_r$ . This is characteristic of the

galloping response, in which  $A_{y,max}/D$  continues increasing with increasing  $U_r$ . The highest  $A_{y,max}/D$  is observed for the  $\alpha = 180^\circ$  configuration with  $A_{y,max}/D = 2.61$  at  $U_r = 12$ .

The  $A_{x,rms}/D$  curves for the single cylinder and the  $\alpha = 0^\circ$  configurations (Figure 5.3 (b)) are characterized by a non-monotonic behaviour. However, there is a visible trend of decrease in the  $A_{x,rms}/D$  values with an increase of  $U_r$ . On the other hand, for the  $\alpha = 90^\circ$  and  $\alpha = 180^\circ$  configurations, the values of  $A_{x,rms}/D$  show a trend of increase in  $A_{x,rms}/D$  with an increase of  $U_r$ .

### 5.2.3 Frequency Analysis

The Fast Fourier Transform (FFT) is used to compute the frequency spectra of  $C_L$ ,  $C_D$ ,  $y/D$  and  $x/D$ . The frequency spectra are shown in Figures 5.4 - 5.7 for the single cylinder,  $\alpha = 0^\circ$ ,  $\alpha = 90^\circ$  and  $\alpha = 180^\circ$  configurations, respectively. The frequency spectra are presented in the  $U_r - fD/U$  plane. For the single cylinder,  $\alpha = 0^\circ$  and  $\alpha = 90^\circ$  configurations, the initial branch is characterized by distinct  $C_L$  peak frequencies. For the  $\alpha = 180^\circ$  configuration, the  $C_L$  peak frequencies are observed for the entire  $U_r$  range due to the extended initial branch compared with the other configurations. This behaviour is in accordance with Figure 5.3 (a). Moreover, the dominant frequencies of  $y/D$  correspond to the lock-in regimes observed for all the configurations. It is observed that the highest amplitudes in the  $y/D$  spectra are located in the low frequency range of  $fD/U < 0.4$ . For all the configurations, the peak frequencies of the spectra decrease with the increase of  $U_r$ . The frequency spectra of  $y/D$  for the single cylinder,  $\alpha = 0^\circ$ ,  $\alpha = 90^\circ$  and  $\alpha = 180^\circ$  configurations is shown in Figure 5.8 for the corresponding  $U_r$  cases with the largest cross-flow amplitude. It is observed that  $\alpha$  influences the peak frequency of  $y/D$ . The lowest dominant frequency of  $fD/U = 0.05$  is observed for the  $\alpha = 180^\circ$  configuration at  $U_r = 12$ . The  $\alpha = 0^\circ$  configuration at  $U_r = 5$  has the highest dominant frequency of  $fD/U = 0.18$ . The single cylinder at  $U_r = 8$  and the  $\alpha = 90^\circ$  configuration at  $U_r = 12$  have a similar dominant frequency of  $fD/U = 0.12$ .

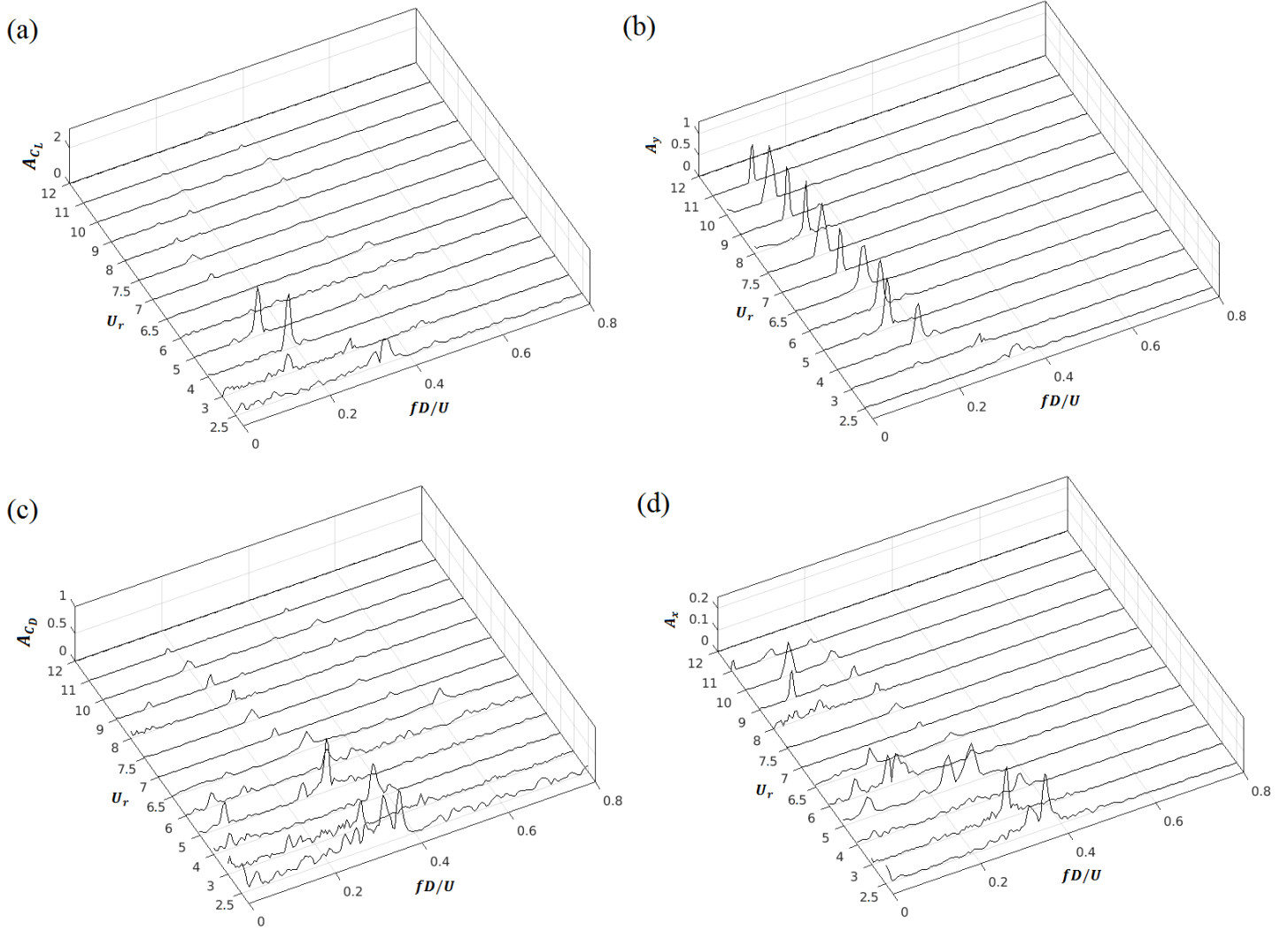


Figure 5.4: Frequency spectra of  $C_L$ ,  $y/D$ ,  $C_D$  and  $x/D$ : single cylinder

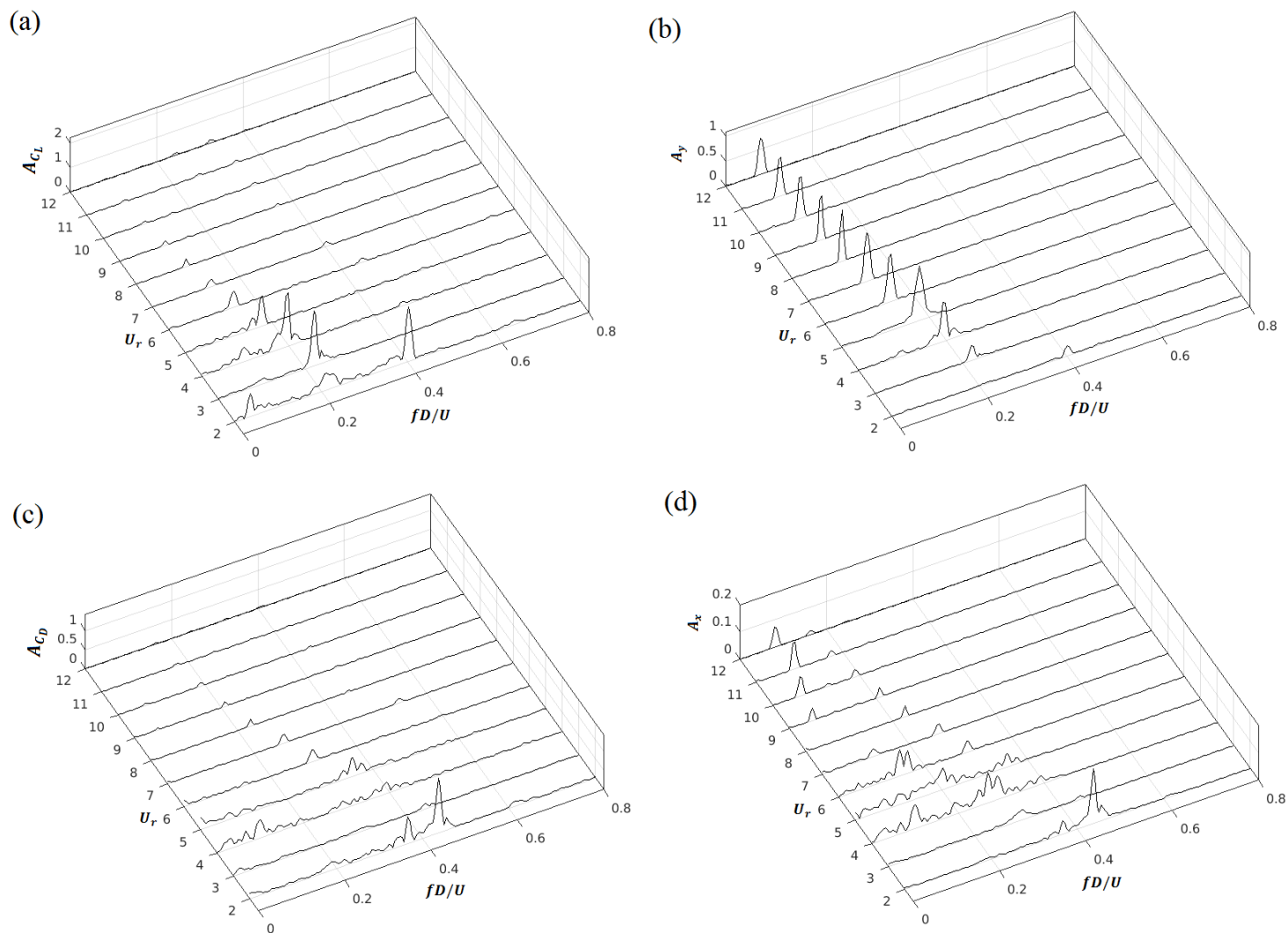


Figure 5.5: Frequency spectra of  $C_L$ ,  $y/D$ ,  $C_D$  and  $x/D$ : coupled cylinders  $\alpha = 0^\circ$ ,  $G/D = 0.1$



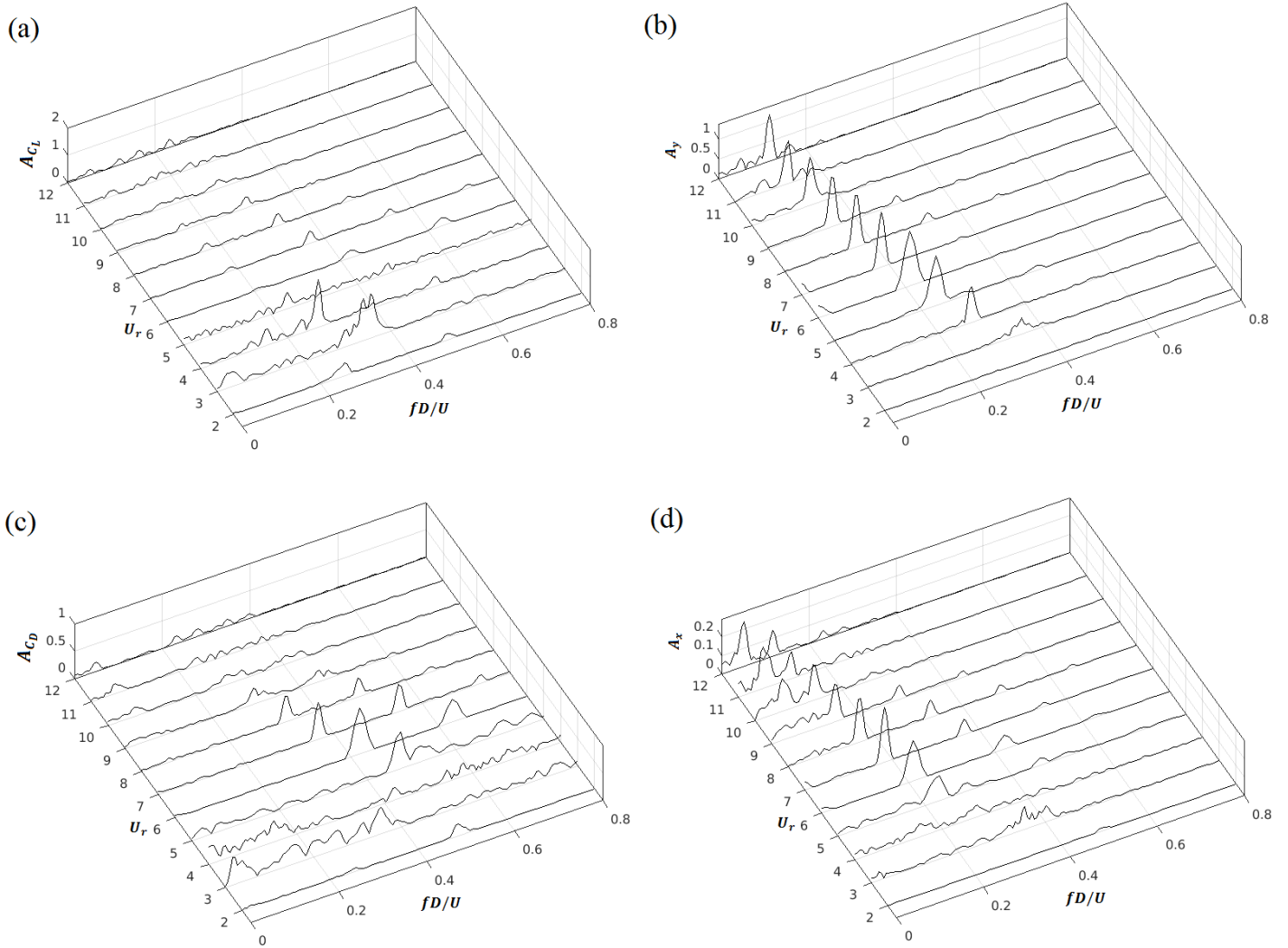


Figure 5.6: Frequency spectra of  $C_L$ ,  $y/D$ ,  $C_D$  and  $x/D$ : coupled cylinders  $\alpha = 90^\circ$ ,  $G/D = 0.1$

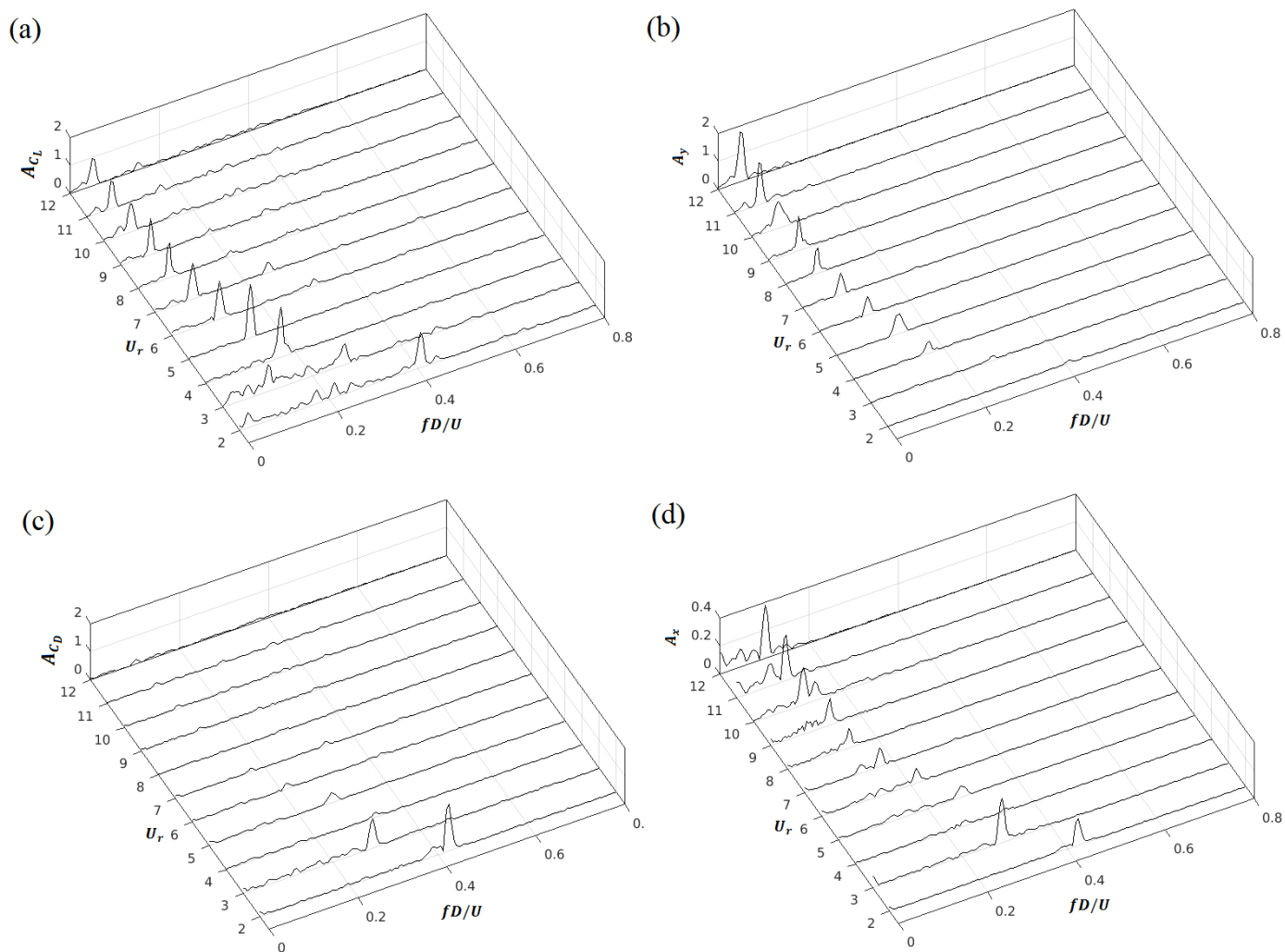


Figure 5.7: Frequency spectra of  $C_L$ ,  $y/D$ ,  $C_D$  and  $x/D$ : coupled cylinders  $\alpha = 180^\circ$ ,  $G/D = 0.1$

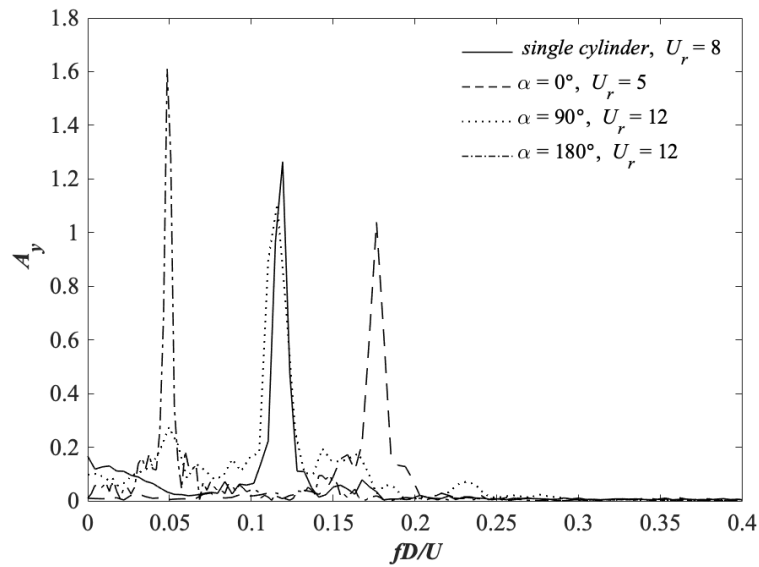


Figure 5.8: Frequency spectra of  $y/D$  for the single cylinder and  $\alpha = [0^\circ, 90^\circ, 180^\circ]$  configurations at selected  $U_r$  corresponding to the cases with the largest transverse displacement amplitude

## 5.2.4 Motion Trajectories

Figures 5.9 - 5.12 show the motion trajectories on the  $x/D - y/D$  plane for the single cylinder,  $\alpha = 0^\circ$ ,  $\alpha = 90^\circ$  and  $\alpha = 180^\circ$  configurations, respectively. The duration of the displacement time series used to plot the motion trajectories is  $\tau = 100$ . For low  $U_r$  values, the trajectory of the single cylinder is characterized by an irregular motion due to large in-line displacement, as shown in Figure 5.9. According to Jauvtis and Williamson (2004), in the VIV of a low-mass ratio system with 2-DoF, the characteristic “figure of eight” trajectory is often observed in the initial branch. This trajectory is seen for  $U_r = 4$  and  $U_r = 5$ . For  $U_r \geq 6.5$ , the trajectory is characterized by small in-line motion. At  $U_r = 12$ , the structural response is desynchronized from the vortex shedding (see Figure 5.3 (a)), thus the in-line and cross-flow amplitudes are almost zero.

For the  $\alpha = 0^\circ$  configuration at  $U_r = 2$  (Figure 5.10), an irregular trajectory is observed. For  $U_r \geq 7$ , the trajectories are regular and characterized by small in-line motion. The trajectories in  $U_r = 11$  and  $U_r = 12$  cases have a skewed oval shape.

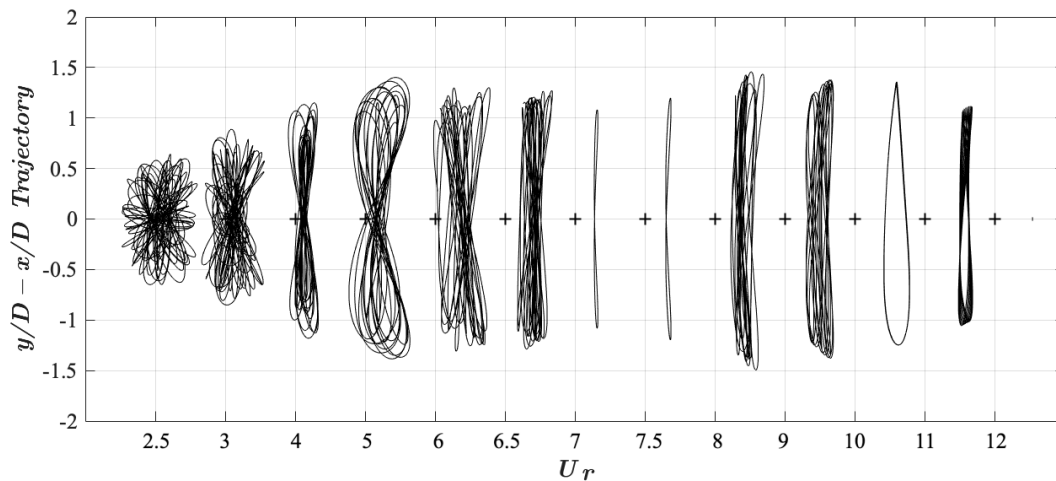


Figure 5.9:  $x/D - y/D$  trajectory: single cylinder

The  $\alpha = 90^\circ$  cases, shown in Figure 5.11, have the most irregular trajectories compared with the single cylinder and  $\alpha = 0^\circ$  configurations. The presence of the small cylinder on top of the large cylinder causes the structure at  $U_r = 2$  to experience almost zero displacement amplitude, both in the in-line and cross-flow directions. The  $U_r = 6, 7$  and  $8$  cases are characterized by the “figure of eight” trajectory. For  $U_r \geq 7$ , the trajectories become more chaotic. This may be explained by the galloping response experienced by the  $\alpha = 90^\circ$  configuration.

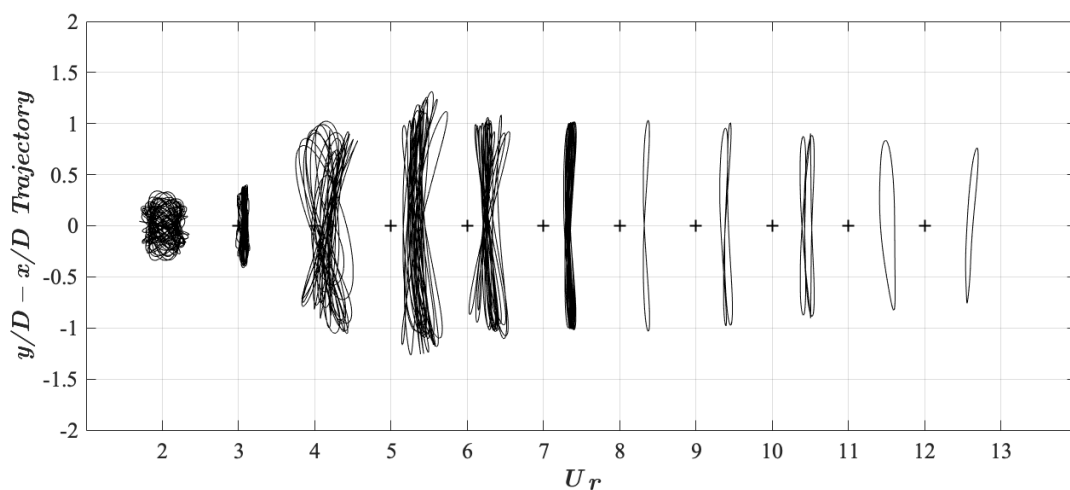


Figure 5.10:  $x/D - y/D$  trajectory: coupled cylinders  $\alpha = 0^\circ$ ,  $G/D = 0.1$

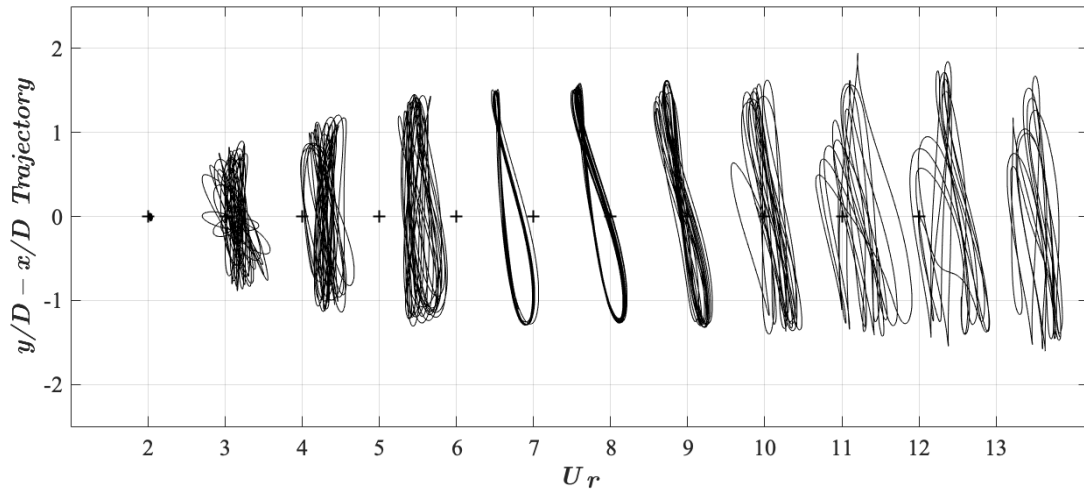


Figure 5.11:  $x/D - y/D$  trajectory: coupled cylinders  $\alpha = 90^\circ$ ,  $G/D = 0.1$

The trajectories of the  $\alpha = 180^\circ$  configuration at  $U_r = 2$  and  $U_r = 3$  are irregular, as shown in Figure 5.12. For  $5 \leq U_r \leq 9$ , the trajectories resemble the crescent shape (Jauvtis and Williamson, 2004). The “figure of eight” trajectory is observed for  $U_r \geq 10$ . Overall, with the increase of  $U_r$ , the cross-flow amplitude increases as observed in Figure 5.3 (a).

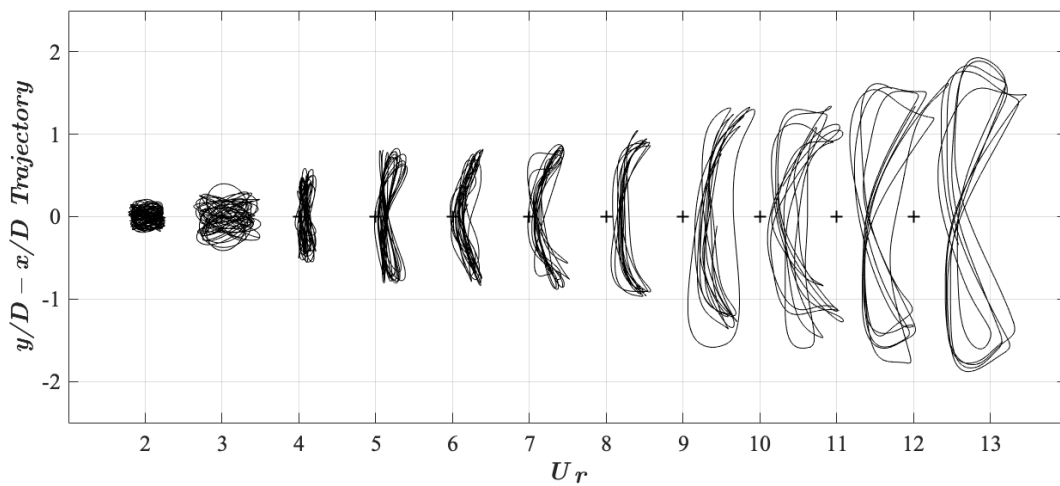


Figure 5.12:  $x/D - y/D$  trajectory: coupled cylinders  $\alpha = 180^\circ$ ,  $G/D = 0.1$

### 5.2.5 Flow Field Analysis

The flow characteristics around the single cylinder and the different  $\alpha$  configurations of the cylinder bundle are analysed. Contours of the spanwise vorticity and the normalized pressure with streamlines are investigated at selected time instances within one oscillation cycle. The presented flow fields correspond to the cases with the largest transverse amplitude of displacement found in the respective configurations. Firstly, the flow features of the single cylinder configuration at  $U_r = 8$  are shown in Figure 5.13. It is observed that two vortex triplets are shed in one cycle (see Figure 5.13 (e)). The vortex shedding mode can be classified as 2T. When the cylinder reaches the highest vertical displacement, a high negative pressure is observed on the upper side of the cylinder (see Figure 5.13 (b)). The opposite is true when the cylinder is at the lowest vertical position (see Figure (f)). Also, when the cylinder is located around  $y/D = 0$ , the negative pressure forces on both sides of the cylinder are balanced. In Figure 5.14, the time histories of the hydrodynamic coefficients,  $C_L$  and  $C_D$ , and the normalized displacements,  $x/D$  and  $y/D$ , for the single cylinder configuration at  $U_r = 8$  are presented. It is observed that the  $C_D$  frequency is twice the  $C_L$  frequency which is characteristic of the flow around an isolated cylinder (Sumer and Fredsøe, 2006). Moreover,  $C_L$  is in phase with  $y/D$  and  $C_D$  is out of phase with  $x/D$ .

Figure 5.15 shows the spanwise vorticity and pressure contours for the  $\alpha = 0^\circ$  configuration at  $U_r = 5$ . The vorticity contours (Figure 5.15 (a) – (g)) reveal that the vortex shedding occurs both behind the small cylinder and the large cylinder. During downward motion of the cylinder bundle (Figure 5.15 (c) and (e)), the vortex street from the small cylinder rolls on top of the large cylinder and breaks the clockwise vortex, which is shed from the upper surface of the large cylinder, into small vortical structures. The same mechanism is observed when the two cylinders move upwards (Figure 5.15 (a) and (g)). In this case, the presence of the small cylinder affects the vortex shedding on the bottom surface of the large cylinder. The vortex street from the small cylinder suppresses the development of a third vortex. Thus, every half cycle of oscillation, a pair of vortices is shed with a residual vorticity from the suppressed vortex. The vortex shedding pattern can be classified as 2P. The pressure contours at selected time instances during one oscillation are shown in Figure 5.15 (b) – (h). It is

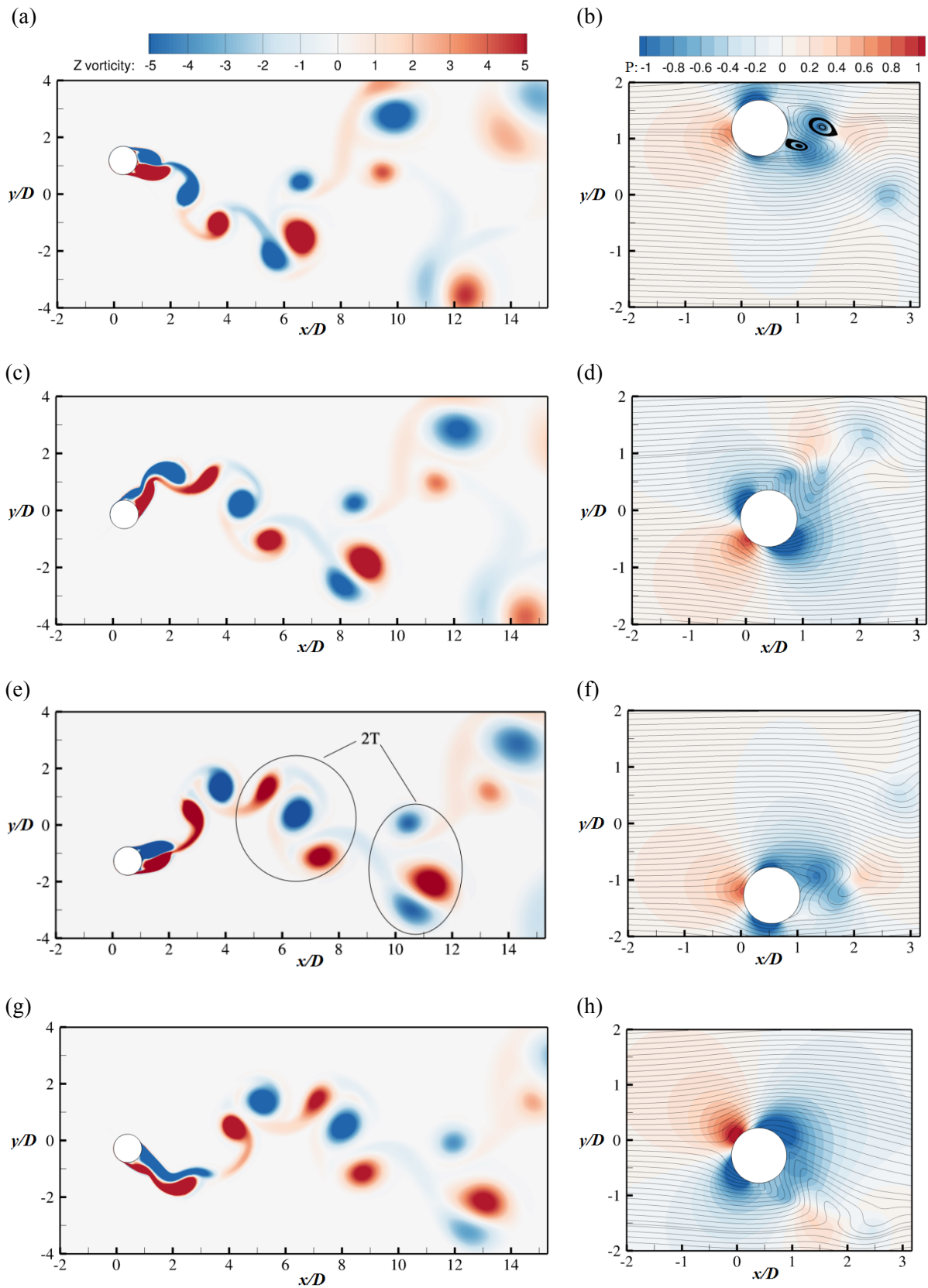


Figure 5.13: Contours of (a, c, e, g) the spanwise vorticity and (b, d, f, h) normalized pressure with streamlines for one vortex shedding cycle: single cylinder at  $U_r = 8$

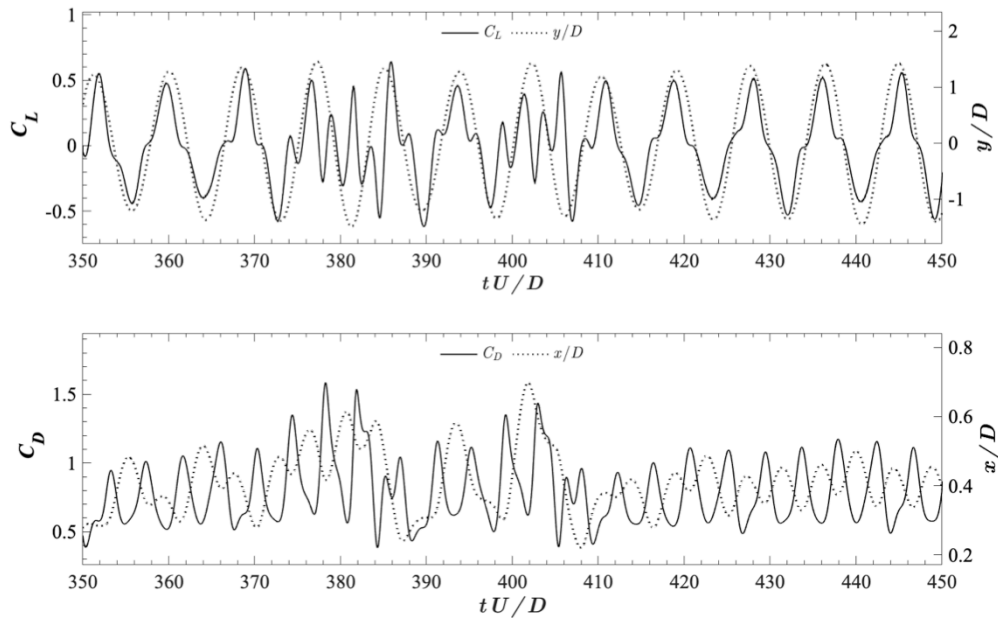


Figure 5.14: Time histories of  $C_L$ ,  $C_D$ ,  $y/D$  and  $x/D$ : single cylinder at  $U_r = 8$

observed that the vortex street from the small cylinder reduces the maximum vertical amplitude of the cylinder bundle as shown in Figure 5.3 (a). The time histories of the hydrodynamic coefficients and the displacements of the  $\alpha = 0^\circ$  configuration at  $U_r = 5$  are presented in Figure 5.16. Similar to the observations made for the single cylinder configuration, it is seen that for the  $\alpha = 0^\circ$  configuration at  $U_r = 5$ ,  $C_L$  is in phase with  $y/D$  and  $C_D$  is out of phase with  $x/D$ .

The flow field around the  $\alpha = 90^\circ$  configuration at  $U_r = 12$  is shown in Figure 5.17. Similar to the observations made for the  $\alpha = 0^\circ$  configuration (see Figure 5.15), the vortex formation (Figure 5.17) behind the large cylinder is influenced by the vortex street developed behind the small cylinder. The vortex shedding from the small cylinder is seen when the cylinder bundle moves upwards and a long vortex street is observed (see Figure 5.17 (a) and (g)). As the coupled cylinders go downward (Figure 5.17 (c) and (e)), the vortex street behind the small cylinder is shortened and this facilitates the detachment of the counter-clockwise vortex from the bottom surface of the large cylinder. A regular vortex shedding mode is not observed. This can be explained by the galloping response experienced by the  $U_r = 12$  case. When  $U_r$  is high, the galloping response is dominant compared with VIV. A region with a high negative pressure is observed around the small cylinder, which is in accordance with



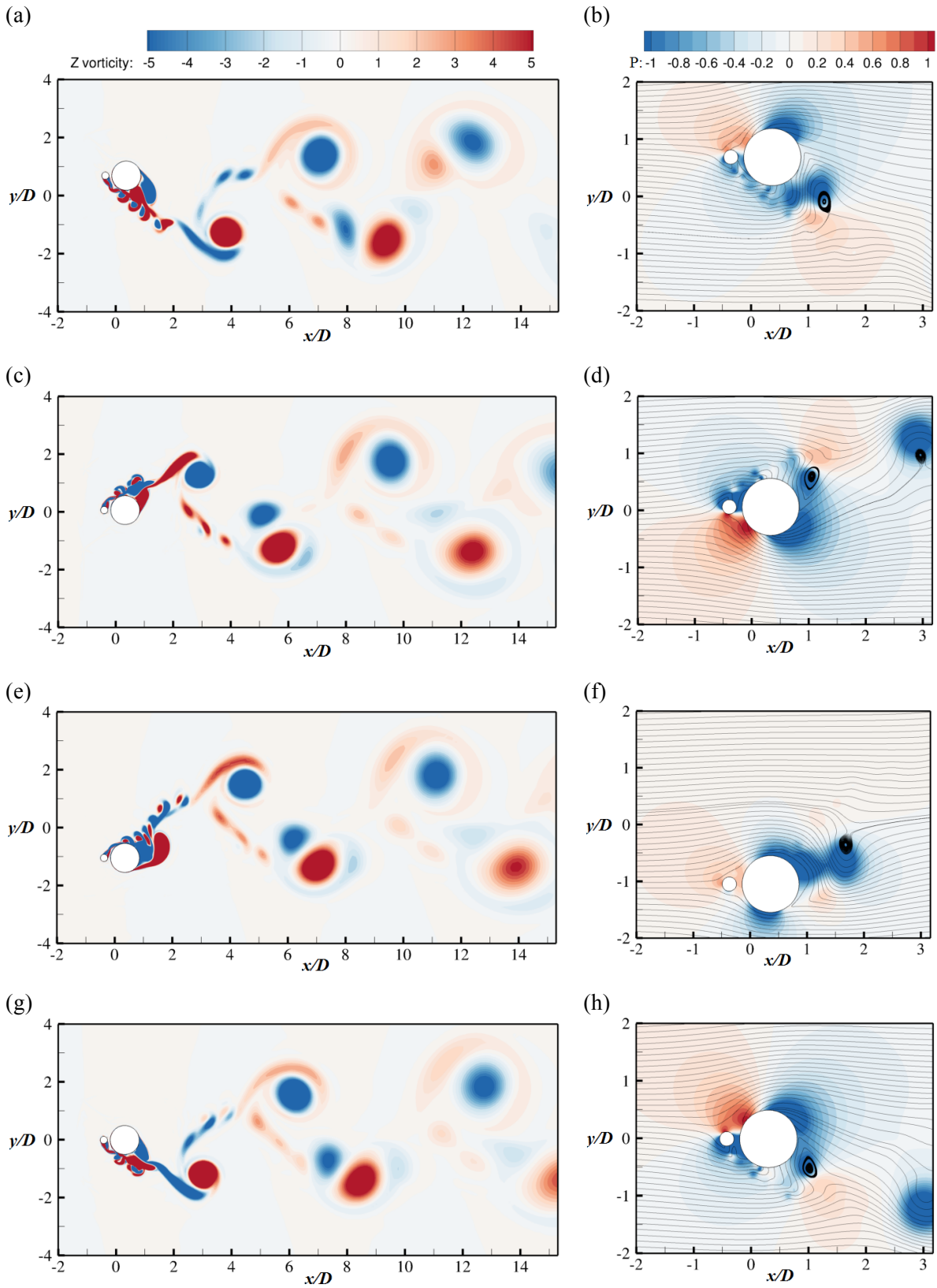


Figure 5.15: Contours of (a, c, e, g) the spanwise vorticity and (b, d, f, h) normalized pressure with streamlines for one vortex shedding cycle: coupled cylinders  $\alpha = 0^\circ$ ,  $G/D = 0.1$  at  $U_r = 5$

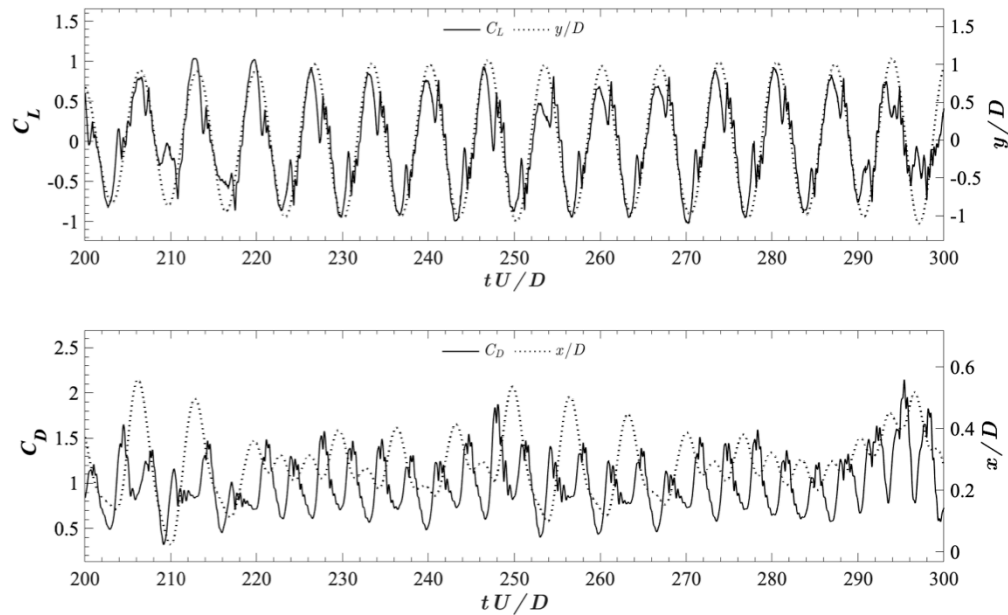


Figure 5.16: Time histories of  $C_L$ ,  $C_D$ ,  $y/D$  and  $x/D$ : coupled cylinders  $\alpha = 0^\circ$ ,  $G/D = 0.1$  at  $U_r = 5$

the larger vertical amplitude compared with the single cylinder and the  $\alpha = 0^\circ$  cases. Figure 5.18 presents the time histories of the hydrodynamic force coefficients and the displacements of the  $\alpha = 90^\circ$  configuration at  $U_r = 12$ . It is revealed that  $C_L$  is not in phase with  $y/D$  and it is explained by the presence of the small cylinder on the top of the large cylinder which creates an asymmetric flow around the bundle. Moreover, larger amplitudes of  $x/D$  are observed compared with those of the single cylinder (see Figure 5.14) and the  $\alpha = 0^\circ$  (see Figure 5.16) cases.

Figure 5.19 shows the spanwise vorticity and pressure contours with streamlines for the  $\alpha = 180^\circ$  configuration at  $U_r = 12$ . The vortex formation length is longer compared with that of the  $\alpha = 0^\circ$  (see Figure 5.15) and  $\alpha = 90^\circ$  (see Figure 5.17) configurations, which explains the lower frequency of the cylinders oscillations (see Figure 5.8). Also, in contrast to the  $\alpha = 0^\circ$  and  $\alpha = 90^\circ$  configurations, the vortex street from the small cylinder is not revealed. Similar to the observations made for the  $\alpha = 90^\circ$  configuration, a regular vortex shedding pattern, which is typical of VIV, is not observed for the  $U_r = 12$  case, due to the galloping response. A strong negative pressure is also observed on the upper and bottom sides of the large cylinder when it is located at the maximum (Figure 5.19 (b)) and the minimum (Figure 5.19 (f)) vertical positions, respectively. The time histories of the hydrodynamic coefficients and the displacements of the  $\alpha = 180^\circ$  configuration at  $U_r = 12$  are presented in

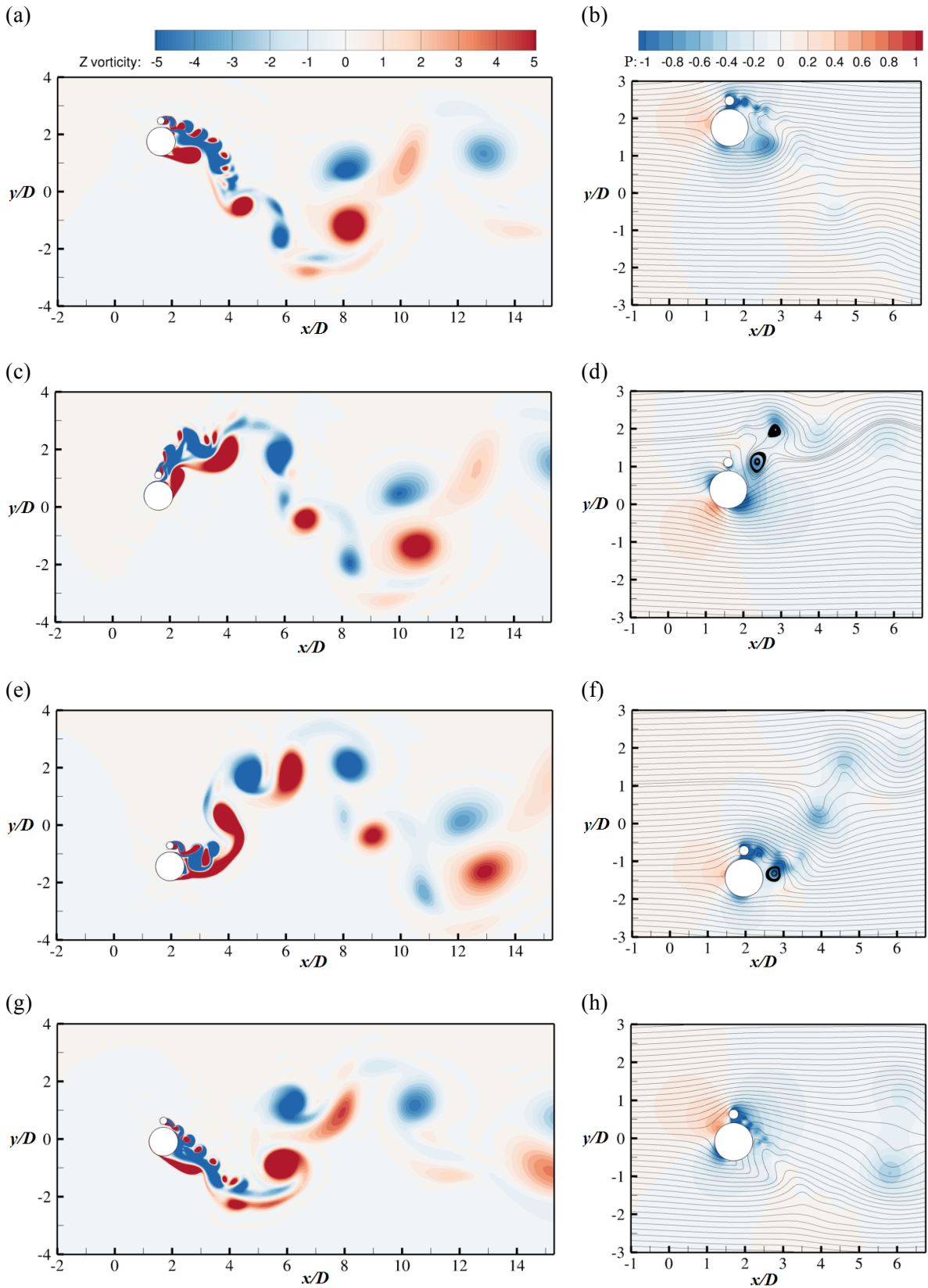


Figure 5.17: Contours of (a, c, e, g) the spanwise vorticity and (b, d, f, h) normalized pressure with streamlines for one vortex shedding cycle: coupled cylinders  $\alpha = 90^\circ$ ,  $G/D = 0.1$  at  $U_r = 12$

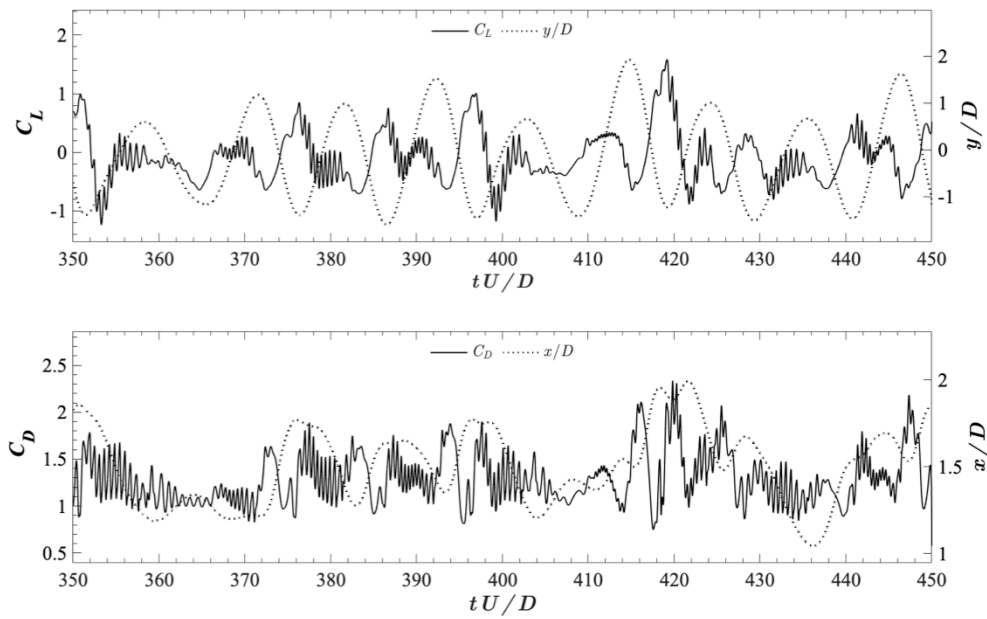


Figure 5.18: Time histories of  $C_L$ ,  $C_D$ ,  $y/D$  and  $x/D$ : coupled cylinders  $\alpha = 90^\circ$ ,  $G/D = 0.1$  at  $U_r = 12$

Figure 5.20. It is observed that  $C_L$  is in phase with  $y/D$  as seen in the single cylinder (see Figure 5.14) and the  $\alpha = 0^\circ$  (see Figure 5.16) cases. In the time history of  $x/D$ , larger in-line displacement amplitudes are observed compared with the  $\alpha = 0^\circ$  configuration (see Figure 5.16).

The time histories of  $C_L$ ,  $C_D$ ,  $y/D$  and  $x/D$  for the single cylinder and the  $\alpha = [0^\circ, 90^\circ, 180^\circ]$  cases that are not presented in this section, are provided in Appendix A.

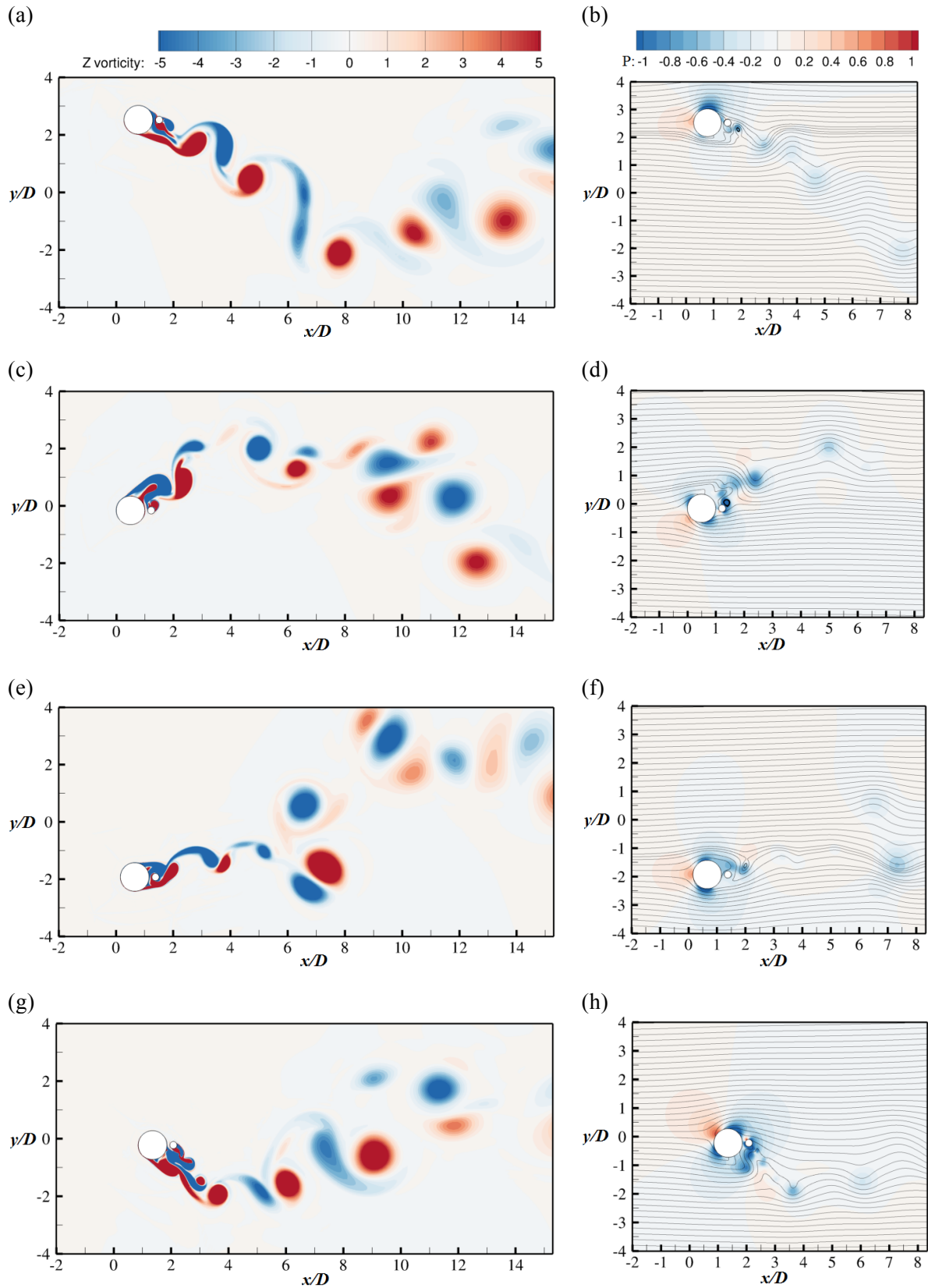


Figure 5.19: Contours of (a, c, e, g) the spanwise vorticity and (b, d, f, h) normalized pressure with streamlines for one vortex shedding cycle: coupled cylinders  $\alpha = 180^\circ$ ,  $G/D = 0.1$  at  $U_r = 12$

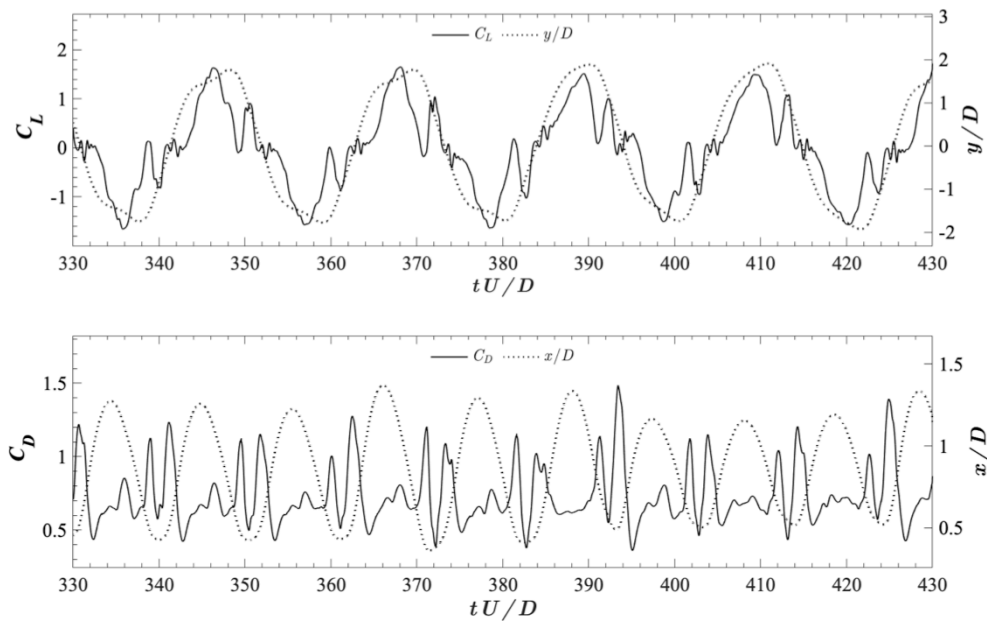


Figure 5.20: Time histories of  $C_L$ ,  $C_D$ ,  $y/D$  and  $x/D$ : coupled cylinders  $\alpha = 180^\circ$ ,  $G/D = 0.1$  at  $U_r = 12$

### 5.3 Effect of the Gap Ratio $G/D$

The effect of  $G/D$  on the FIV response of two rigidly coupled cylinders is analysed with respect to the hydrodynamic coefficients, vibration amplitude, response frequencies and flow fields. In addition to the  $\alpha = 90^\circ$  configuration with  $G/D = 0.1$  presented in the previous section, two additional values of  $G/D$  are investigated, 0.25 and 0.5.

#### 5.3.1 Hydrodynamic Force Coefficients

Figure 5.21 illustrates the values of  $\overline{C_D}$  and  $C_{D,rms}$  versus  $U_r$  for the single cylinder and the studied  $G/D$  configurations. It can be observed that with the increase of  $G/D$ ,

$\bar{C}_D$  is approximating to the values observed for the single cylinder configuration. For  $3 \leq U_r \leq 9$ , the  $G/D = 0.1$  configuration has the highest values of  $\bar{C}_D$ , with a peak at  $U_r = 5$ . Among the coupled cylinder configurations, the  $G/D = 0.5$  configuration has the lowest values of  $\bar{C}_D$ , and the response curve of  $\bar{C}_D$  is the closest to that of the single cylinder configuration. The  $\bar{C}_D$  response curve for the  $G/D = 0.25$  configuration lies in between those of the  $G/D = 0.1$  and  $G/D = 0.5$  configurations. The  $C_{D,rms}$  values observed for the single cylinder configuration (Figure 5.21 (b)) show considerably more fluctuations compared with those for the other investigated configurations. The  $C_{D,rms}$  response curves of the coupled cylinder cases are characterized by peak values at low  $U_r$ , and a monotonic decrease. The peak in  $C_{D,rms}$  for the  $G/D = 0.1$  and  $G/D = 0.5$  configurations occurs at  $U_r = 3$ , and for the  $G/D = 0.25$  case, it is observed at  $U_r = 2$ .

Figure 5.22 presents the  $\bar{C}_L$  and  $C_{L,rms}$  response curves of the single cylinder and the investigated  $G/D$  configurations. It is shown in Figure 5.22 (a), that the presence of the small cylinder at different  $G/D$  values causes non-zero values of  $\bar{C}_L$ . The highest values of  $\bar{C}_L$  are observed for the  $G/D = 0.1$  and  $G/D = 0.25$  configurations. For the  $G/D = 0.5$  configuration, the  $\bar{C}_L$  curve is closer to that of the single cylinder

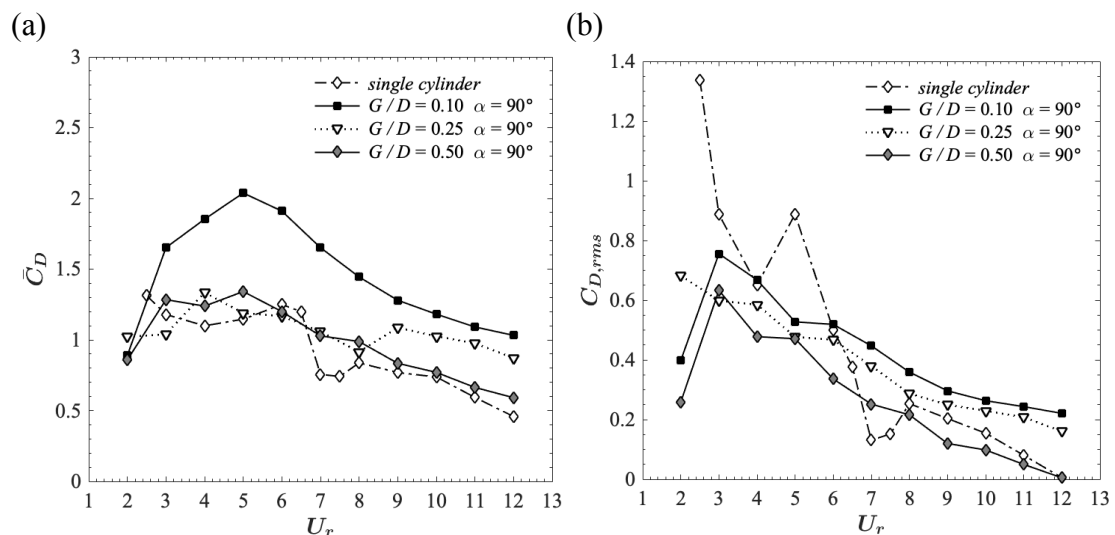


Figure 5.21: Time-averaged drag coefficient  $\bar{C}_D$  (a) and the root-mean-square of the drag coefficient  $C_{D,rms}$  (b) for the single cylinder and  $[G/D = 0.1, 0.25, 0.5]$  configurations

compared with the  $G/D = 0.1$  and  $G/D = 0.25$  configurations. This is in accordance with Zang and Gao (2014), who reported that the magnitude of  $\overline{C}_L$  increases with increasing  $G/D$  until approximately  $G/D = 0.25$ . For  $G/D > 0.25$ ,  $\overline{C}_L$  decreases and converges to the values observed for the single cylinder configuration.

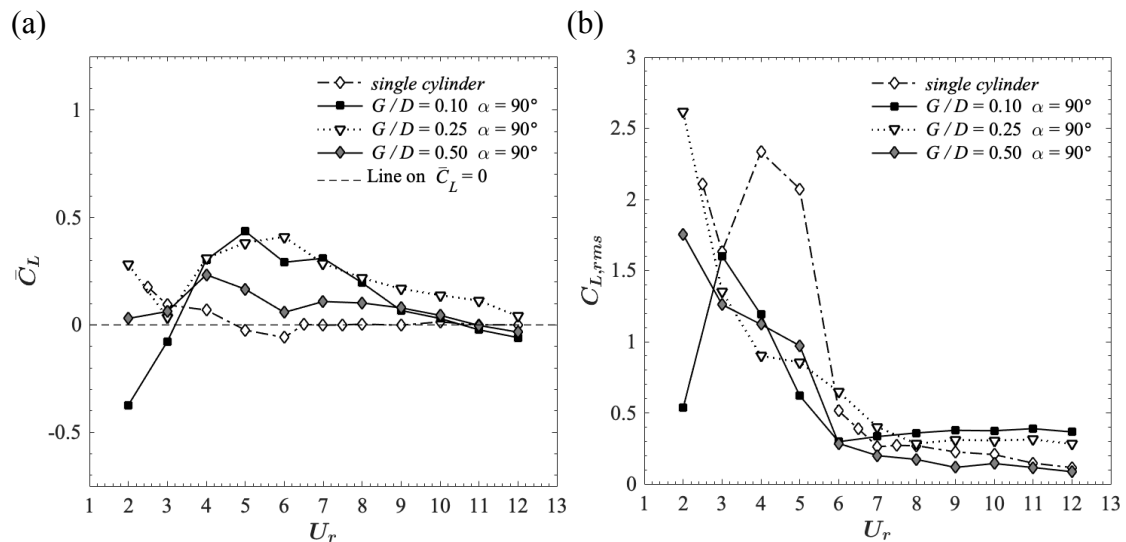


Figure 5.22: Time-averaged lift coefficient  $\overline{C}_L$  (a) and root-mean-square of the lift coefficient  $C_{L,rms}$  (b) for the single cylinder and  $[G/D = 0.1, 0.25, 0.5]$  configurations

The shape of the  $C_{L,rms}$  response curve (Figure 5.22 (b)) for the  $G/D = 0.5$  and  $G/D = 0.25$  configurations is characterized by a peak value at  $U_r = 2$  followed by a sharp decrease. The peak in  $C_{L,rms}$  observed for the  $G/D = 0.25$  configuration is significantly higher than the predicted values of  $C_{L,rms}$  for the other configurations. For  $U_r > 6$ , the  $C_{L,rms}$  values for the single cylinder and the  $G/D = 0.5$  configurations converge to similar values. Finally, the  $C_{L,rms}$  values for the  $G/D = 0.1$  configuration at  $U_r > 7$  cases are the highest among the investigated configurations.



### 5.3.2 Amplitude Response

The  $A_{y,max}/D$  and  $A_{x,rms}/D$  response curves for the single cylinder and the different  $G/D$  configurations are presented in Figure 5.23. It is observed (see Figure 5.23 (a)), that the lock-in regime for the single cylinder and the  $G/D = 0.5$  configurations are captured within the range of studied  $U_r$ . For the  $G/D = 0.5$  configuration, the maximum  $A_{y,max}/D$  is approximately  $A_{y,max}/D = 1.40$  at  $U_r = 8$ , which is lower than the peak value observed for the single cylinder configuration of  $A_{y,max}/D = 1.52$ . The lock-in range for the  $G/D = 0.1$  and  $G/D = 0.25$  configurations extend beyond  $U_r = 12$ . The maximum observed value of  $A_{y,max}/D$  for the  $G/D = 0.25$  configuration is approximately  $A_{y,max}/D = 1.59$  at  $U_r = 6$ . Based on the observations made in the present study,  $G/D$  has significant influence on the vibration response of the cylinder bundle. For small  $G/D$  values ( $G/D \leq 0.25$ ),  $A_{y,max}/D$  is increased at high  $U_r$  ( $U_r > 8$ ).

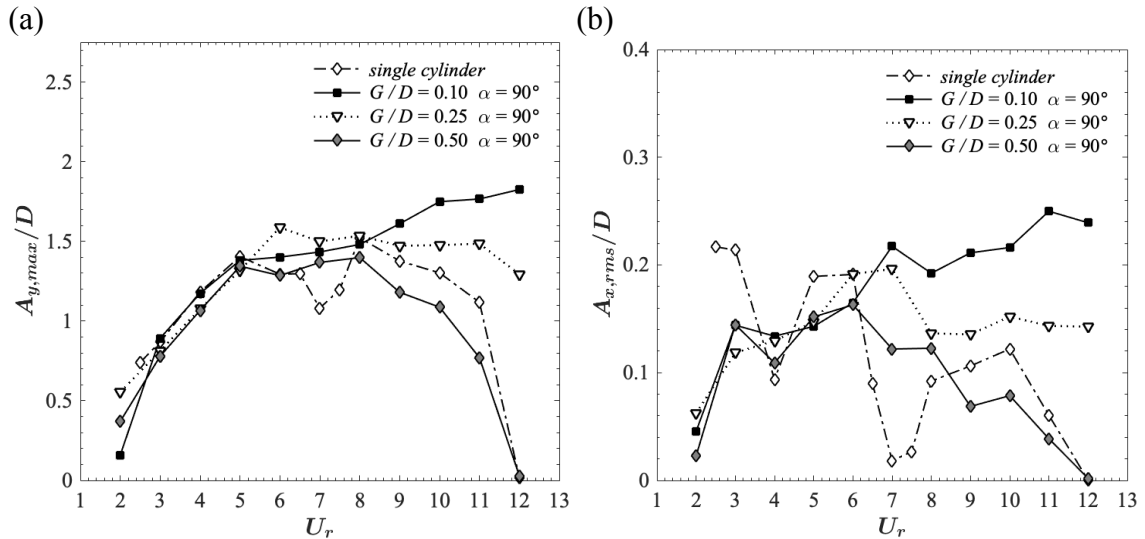


Figure 5.23: Normalized maximum cross-flow vibration amplitude  $A_{y,max}/D$  (a) and normalized root-mean-square of the in-line vibration amplitude  $A_{x,rms}/D$  (b) for the single cylinder and [ $G/D = 0.1, 0.25, 0.5$ ] configurations

### 5.3.3 Frequency Analysis

The frequency spectra of  $C_L$ ,  $C_D$ ,  $y/D$  and  $x/D$  are shown in Figures 5.24 and 5.25 for the  $G/D = 0.25$  and  $G/D = 0.5$  configurations, respectively. The frequency spectra are presented in the  $U_r - fD/U$  plane. In the  $C_L$  spectra of  $G/D = 0.25$  and  $G/D = 0.5$  configurations, the highest amplitudes are observed at low  $U_r$  which correspond to the initial branch of VIV. The  $y/D$  spectra show peak frequencies in

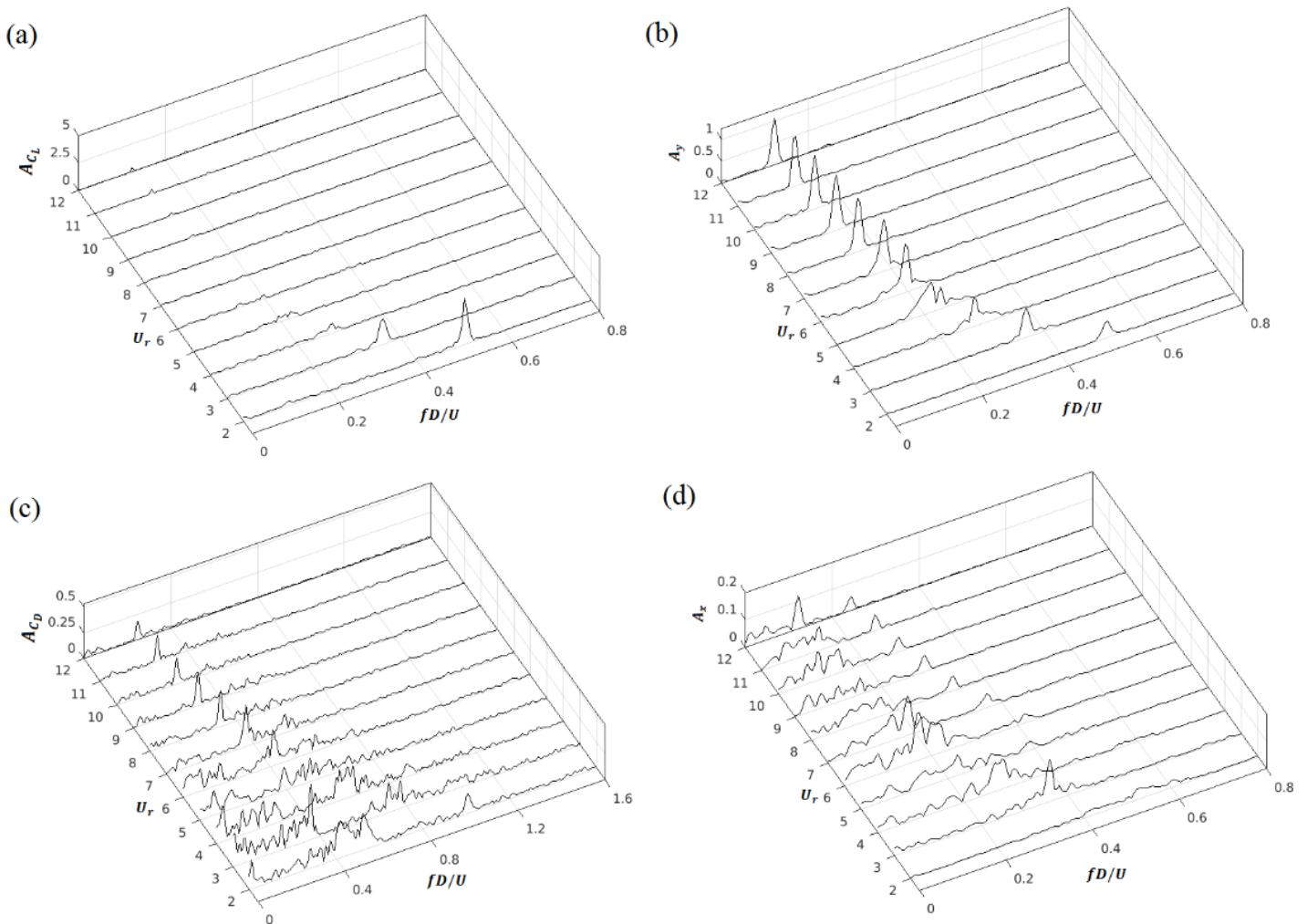


Figure 5.24: Frequency spectra of  $C_L$ ,  $y/D$ ,  $C_D$  and  $x/D$ : coupled cylinders  $\alpha = 90^\circ$ ,  $G/D = 0.25$

the lock-in regime observed in Figure 5.23 (a). Overall, the  $C_D$  and  $x/D$  spectra are broad-banded compared with the corresponding spectra of the single cylinder and  $G/D = 0.1$  configurations (see Figure 5.4 and Figure 5.5). The frequency spectra of  $y/D$  for the single cylinder,  $G/D = 0.1$ ,  $G/D = 0.25$  and  $G/D = 0.5$  configurations are shown in Figure 5.26 for the corresponding  $U_r$  cases with the largest cross-flow amplitude.

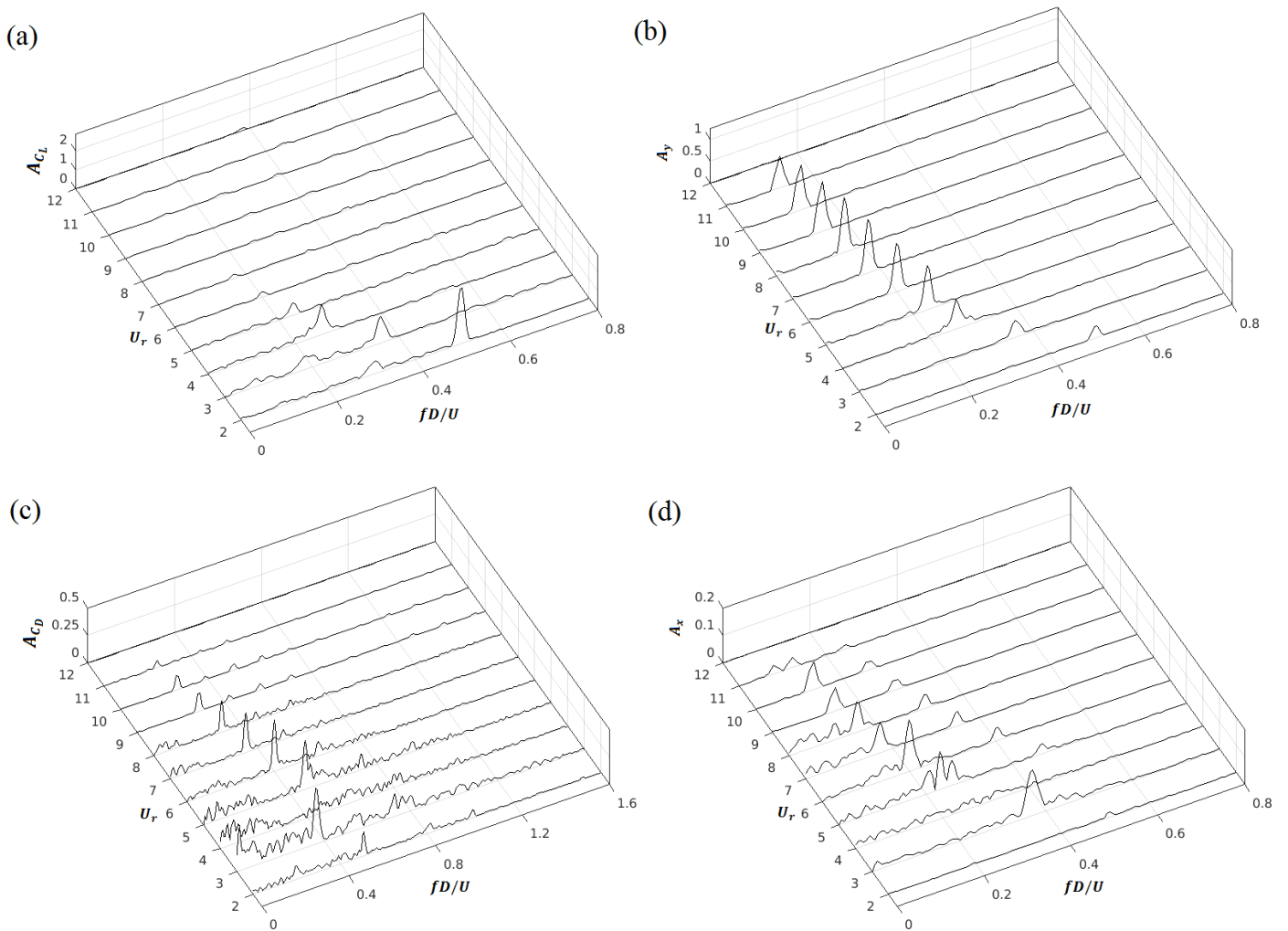


Figure 5.25: Frequency spectra of  $C_L$ ,  $y/D$ ,  $C_D$  and  $x/D$ : coupled cylinders  $\alpha = 90^\circ$ ,  $G/D = 0.5$

Similar to the observations made for the effect of  $\alpha$ ,  $G/D$  influences the peak frequency of  $y/D$ . The highest dominant frequency of  $fD/U = 0.19$  is observed for the  $G/D = 0.25$  configuration at  $U_r = 6$ . The  $G/D = 0.5$  configuration at  $U_r = 8$  has

a dominant frequency of  $fD/U = 0.15$ . This value is closer to the dominant frequency observed for the single cylinder at  $U_r = 8$  and the  $G/D = 0.1$  configuration at  $U_r = 12$ .

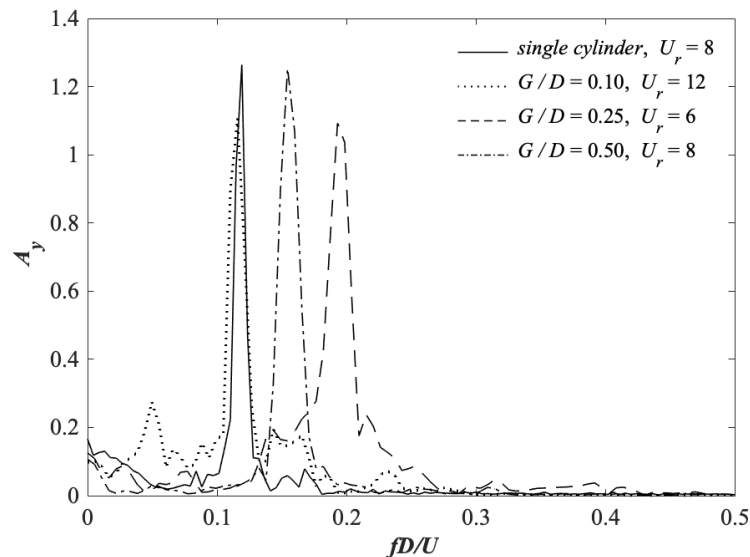


Figure 5.26: Frequency spectra of  $y/D$  for the single cylinder and [ $G/D = 0.1, 0.25, 0.5$ ] configurations at selected  $U_r$  corresponding to the cases with the largest transverse displacement amplitude

### 5.3.4 Motion Trajectories

Figures 5.27 and 5.28 present the motion trajectories in the  $x/D - y/D$  plane for the  $G/D = 0.25$  and  $G/D = 0.5$  configurations, respectively. The duration of the displacement time series used to plot the motion trajectories is  $\tau = 100$ . It is observed that the trajectories of  $G/D = 0.25$  and  $G/D = 0.5$  configurations are narrower compared with the  $G/D = 0.1$  configuration (see Figure 5.14). The in-line motion experienced by  $G/D = 0.25$  and  $G/D = 0.5$  configurations is smaller compared with the  $G/D = 0.1$  configuration. The  $U_r = 2$  cases of the  $G/D = 0.25$  and  $G/D = 0.5$  configurations have lower in-line amplitude compared with the  $U_r = 2$  case of the single cylinder configuration. Overall, it is seen that with the increase in  $G/D$ , the trajectories converge to those observed for the single cylinder cases (see Figure 5.9).

This is explained by the decreased influence of the vortex shedding from the small cylinder on the large cylinder, with increasing  $G/D$ .

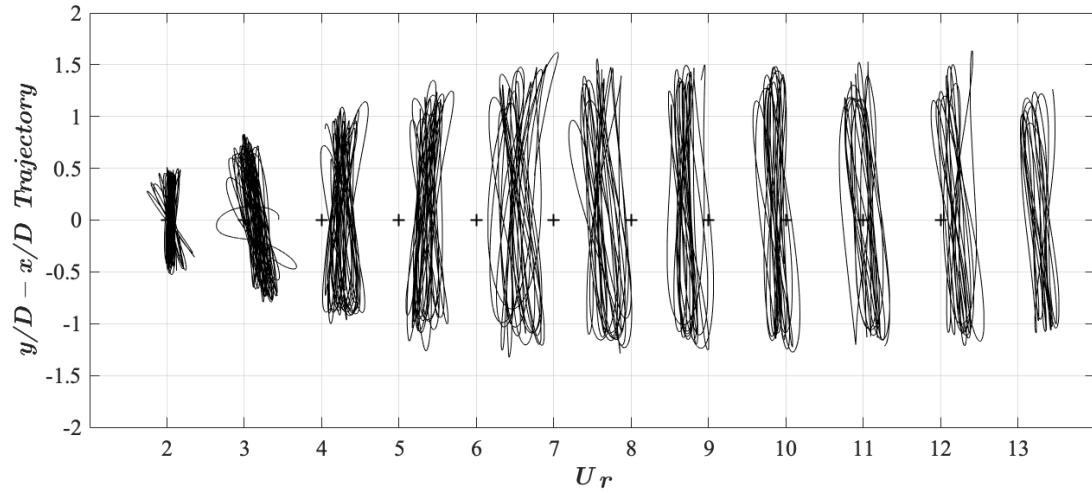


Figure 5.27:  $x/D - y/D$  trajectory: coupled cylinders  $\alpha = 90^\circ$ ,  $G/D = 0.25$

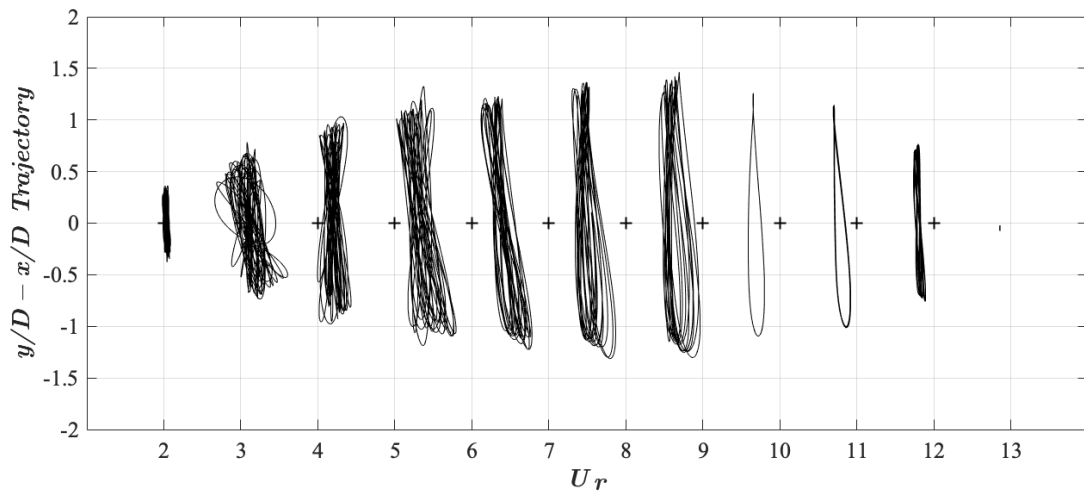


Figure 5.28:  $x/D - y/D$  trajectory: coupled cylinders  $\alpha = 90^\circ$ ,  $G/D = 0.5$

### 5.3.5 Flow Field Analysis

The contours of the spanwise vorticity and the normalized pressure with streamlines for the  $G/D = 0.25$  and  $G/D = 0.5$  configurations are investigated at selected time instances within one oscillation cycle. The presented flow fields correspond to the cases with the largest transverse amplitude of displacement found in respective configurations. The flow features around the  $G/D = 0.25$  configuration at  $U_r = 6$  are presented in Figure 5.29. A vortex street behind the small cylinder is observed, similarly to the  $G/D = 0.1$  configuration (see Figure 5.17). During the downward movement of the cylinder bundle (Figure 5.29 (c) and (e)), the vortices shed from the large cylinder follow the shear layers of the small cylinder. As the clockwise vortex, shed from the top of the large cylinder, merges with the vortex street behind the small cylinder, it is observed the formation of many vortical structures behind the cylinder bundle. It is seen that the presence of the small cylinder suppresses the vortex shedding from the top of the large cylinder and this causes a positive lift on the cylinder bundle, as reported by Jauvtis and Williamson (2004). When the cylinders move upwards (Figure 5.29 (a) and (g)), the vortex formation length from the small cylinder is elongated before it merges with the newly formed vortices on the backside of the large cylinder. There is a region of strong negative pressure around the small cylinder (Figure 5.29 (b)). However, it is slightly weaker than the negative pressure observed for the  $G/D = 0.1$  configuration (see Figure 5.17). This explains the lower vertical amplitude of displacement observed for the  $G/D = 0.25$  configuration compared with the  $G/D = 0.1$  configuration. Figure 5.30 presents the time histories of the hydrodynamic coefficients and displacements for the  $G/D = 0.25$  configuration at  $U_r = 6$ . It is observed that  $C_L$  is in phase with  $y/D$  as opposed to the observations made for the  $G/D = 0.1$  configuration (see Figure 5.18). Overall, the amplitudes of  $x/D$  are lower compared with the  $G/D = 0.1$  case shown in Figure 5.18.

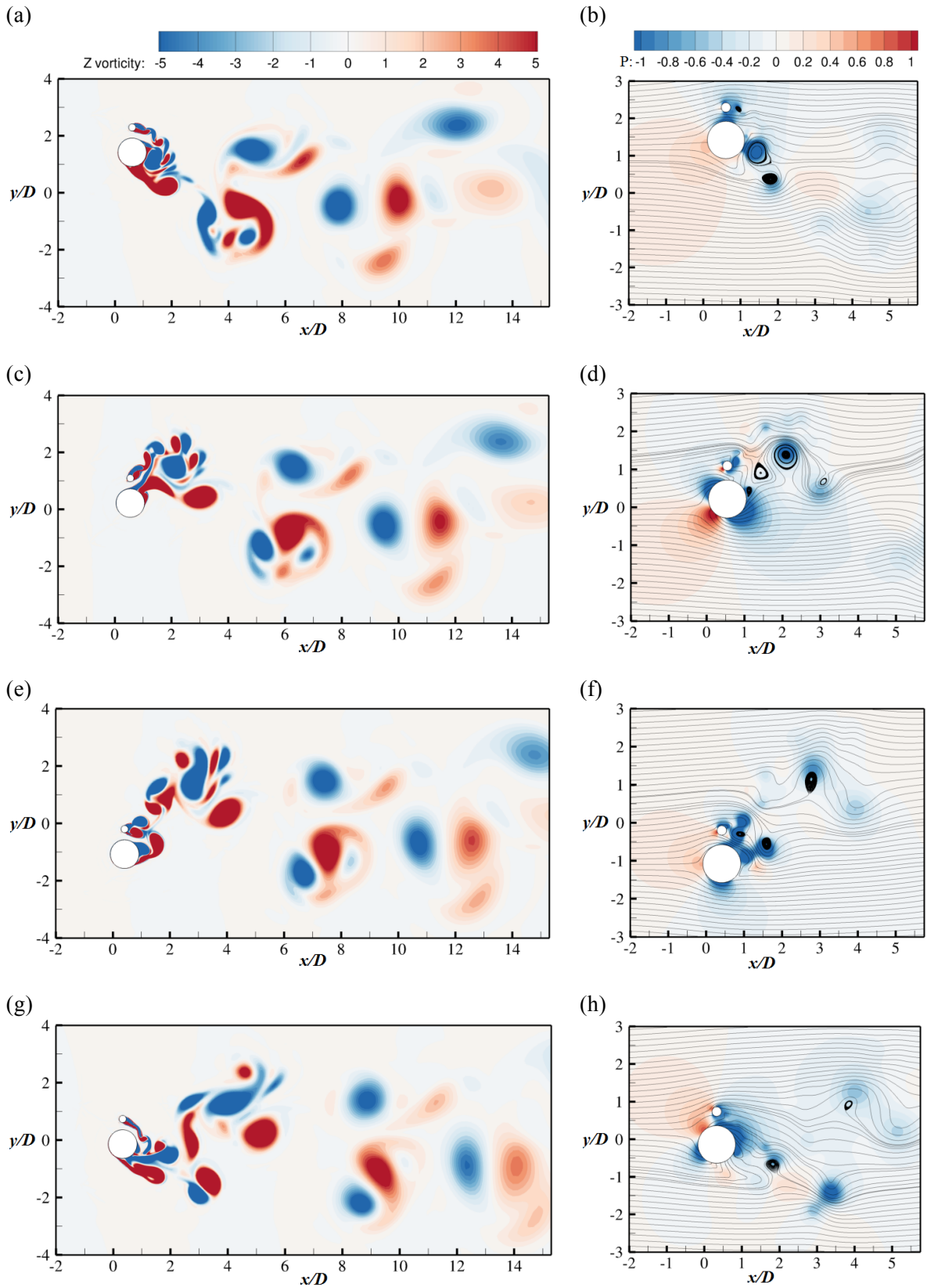


Figure 5.29: Contours of (a, c, e, g) the spanwise vorticity and (b, d, f, h) normalized pressure with streamlines for one vortex shedding cycle: coupled cylinders  $\alpha = 90^\circ$ ,  $G/D = 0.25$  at  $U_r = 6$

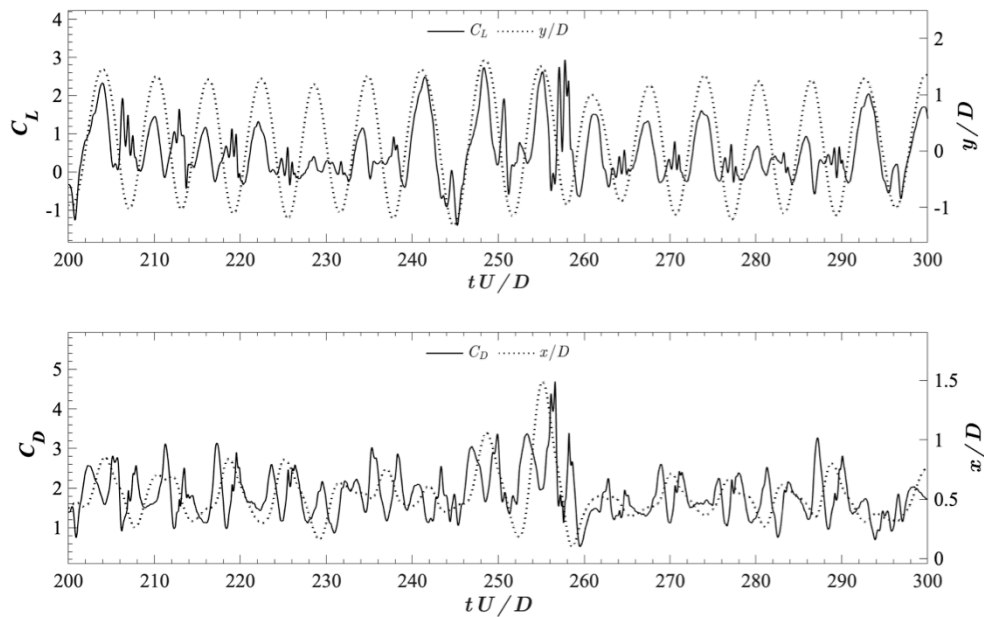


Figure 5.30: Time histories of  $C_L$ ,  $C_D$ ,  $y/D$  and  $x/D$ : coupled cylinders  $\alpha = 90^\circ$ ,  $G/D = 0.25$  at  $U_r = 6$

Figure 5.31 shows the contours of the spanwise vorticity and the pressure with streamlines for the  $G/D = 0.5$  configuration at  $U_r = 8$ . Compared with the  $G/D = 0.1$  and  $G/D = 0.25$  configurations, the vortex formation length from the small cylinder is increased and larger vortical structures are formed due to the increased  $G/D$  value. These vortices from the small cylinder merge with the vortical structures from the large cylinder (Figure 5.31 (a) – (g)). As the cylinder bundle goes downward (Figure 5.31 (c) and (e)), the newly formed vortices from the large cylinder break the vortex street from the small cylinder. The velocity profiles between the small cylinder and the large cylinder for the [ $G/D = 0.1, 0.25, 0.5$ ] configurations are presented in Figure 5.32. It is observed that with the increase of  $G/D$ , the mean velocity decreases in the gap region. This is in accordance with the pressure contours for the respective configurations (see Figure 5.17 (b) – (h), Figure 5.29 (b) – (h) and Figure 5.31 (b) – (h)), where it is seen that the regions of negative pressure around the small cylinder weakens with the increase of  $G/D$ .



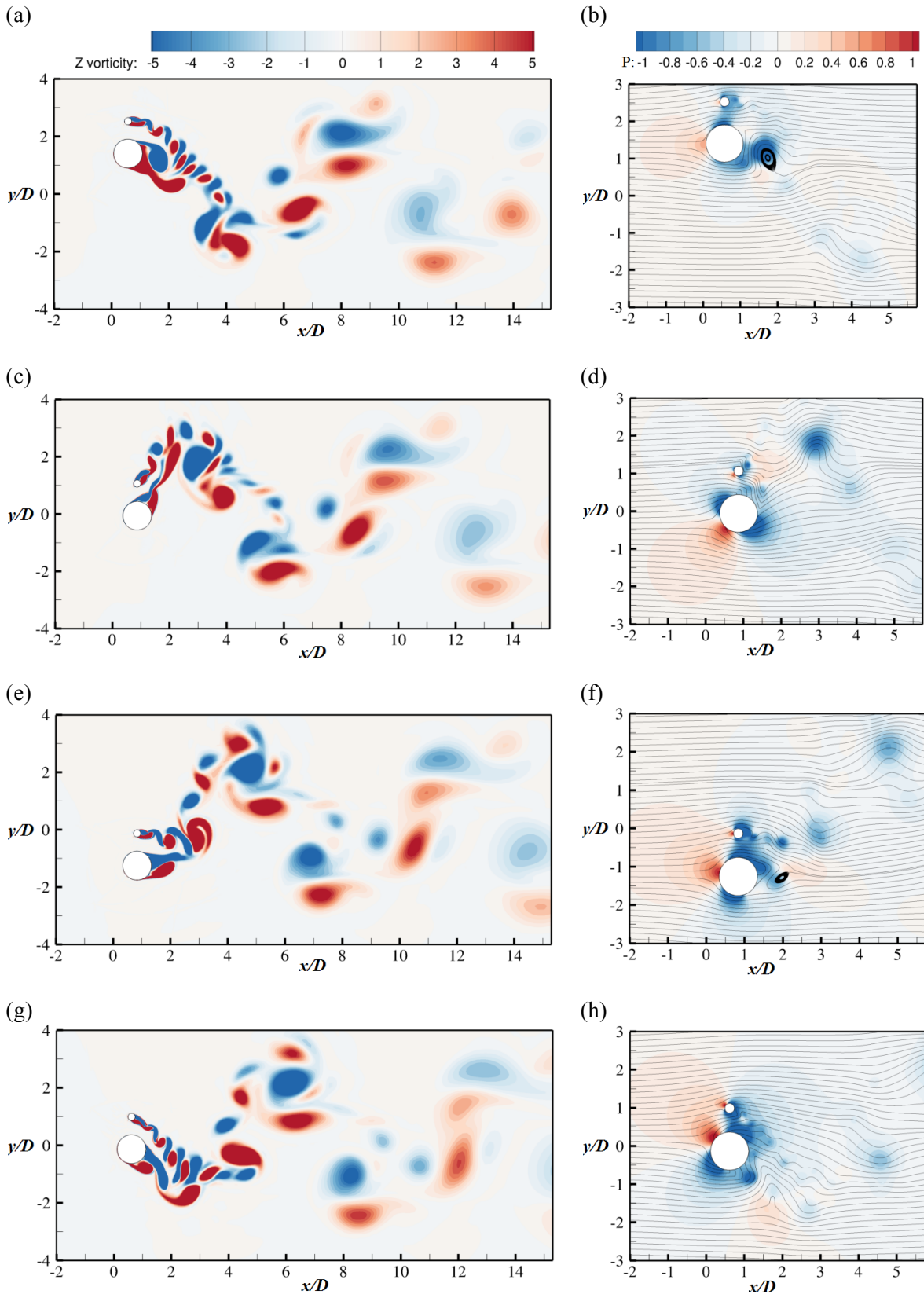


Figure 5.31: Contours of (a, c, e, g) the spanwise vorticity and (b, d, f, h) normalized pressure with streamlines for one vortex shedding cycle: coupled cylinders  $\alpha = 90^\circ$ ,  $G/D = 0.5$  at  $U_r = 8$

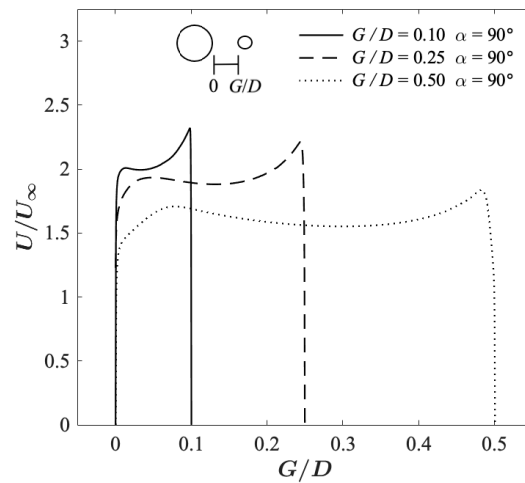


Figure 5.32: Velocity profile in the gap between the cylinders:  $G/D = 0.1$  at  $U_r = 12$ ,  $G/D = 0.25$  at  $U_r = 6$  and  $G/D = 0.5$  at  $U_r = 8$

The time histories of the hydrodynamic coefficients and displacements for the  $G/D = 0.5$  configuration at  $U_r = 8$  are presented in Figure 5.33. It is observed that  $C_L$  is in phase with  $y/D$  and  $C_D$  is out of phase with  $x/D$ . Finally, the time histories of  $C_L$ ,  $C_D$ ,  $y/D$  and  $x/D$  for the  $[G/D = 0.1, 0.25, 0.5]$  cases that are not presented in this section, are provided in Appendix A.

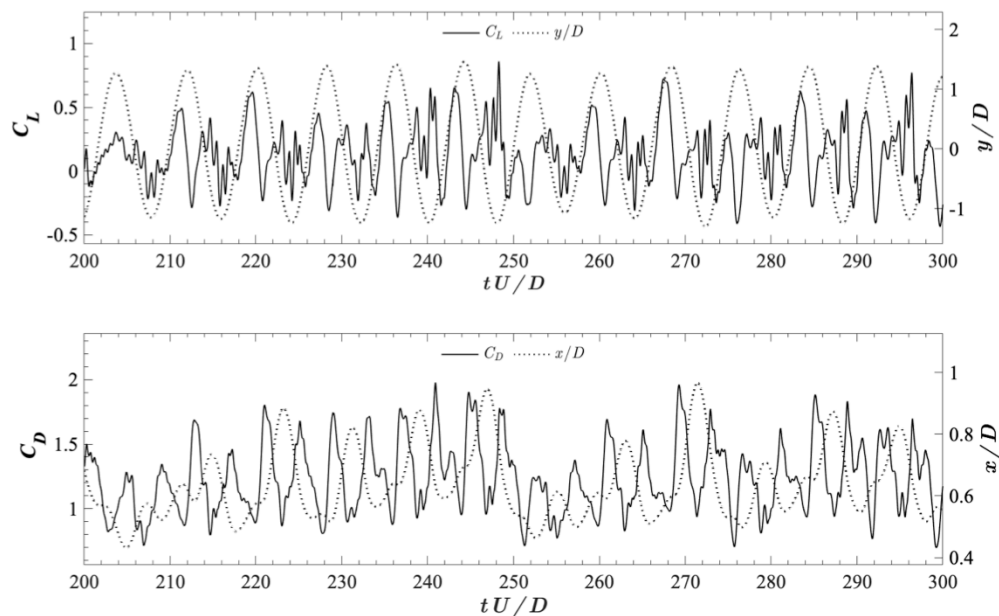


Figure 5.33: Time histories of  $C_L$ ,  $C_D$ ,  $y/D$  and  $x/D$ : coupled cylinders  $\alpha = 90^\circ$ ,  $G/D = 0.5$  at  $U_r = 8$

## Chapter 6

# Conclusions and Recommendations for Future Work

### 6.1 Conclusions

In the present study, the flows around a single cylinder and two rigidly coupled cylinders are analysed at  $Re = 3.6 \times 10^6$ . The 2D URANS equations are solved combined with the  $k - \omega$  SST turbulence model. Different configurations of the two rigidly coupled cylinders are simulated and their influence on the FIV response of the system is investigated and compared with the single cylinder response. Grid convergence studies are carried out for the single cylinder and the  $\alpha = 90^\circ$  configuration with  $G/D = 0.1$ , and a good balance between the computational cost and discretization error is obtained with 104536 and 114321 cells, respectively. The numerical model is validated for a stationary single cylinder against published numerical and experimental studies in the high Reynolds number regime with a satisfactory agreement. The drag and lift coefficients, the in-line and cross-flow vibration amplitudes, the frequency responses, the motion trajectories and the flow fields are discussed. The main conclusions are summarized as follows:

#### 1. Effect of $\alpha$ :

- In general, the highest  $\overline{C}_D$  values occur for the  $\alpha = 90^\circ$  configuration, and the lowest are observed for the  $\alpha = 180^\circ$  configuration. When the cylinders are in tandem, the results obtained for  $\overline{C}_L$  tend to that of the single cylinder, which are found to be around zero. For the  $\alpha = 90^\circ$  configuration, the cylinder bundle experiences negative  $\overline{C}_L$  for  $U_r \leq 3$  and  $U_r \geq 11$ , and positive  $\overline{C}_L$  for  $4 \leq U_r \leq 10$ .

- It is found that for the  $\alpha = 0^\circ$ ,  $\alpha = 90^\circ$  and  $\alpha = 180^\circ$  configurations, the presence of the small cylinder widens the lock-in regime compared with that of the single cylinder. The  $\alpha = 0^\circ$  configuration has the lowest  $A_{y,max}/D$  value of 1.26, and the highest  $A_{y,max}/D$  value of 2.61 is found for the  $\alpha = 180^\circ$  configuration. The galloping response is observed for the  $\alpha = 90^\circ$  and  $\alpha = 180^\circ$  configurations.
- The frequency analysis shows that  $\overline{C}_L$  has a peak frequency in the initial branch of FIV for all the configurations. Moreover, the peak frequencies of all the spectra are in the low frequency range of  $fD/U < 0.4$  and tend to decrease with the increase of  $U_r$ .
- The  $\alpha = 90^\circ$  configuration has the most irregular motion trajectories, compared with those of the single cylinder,  $\alpha = 0^\circ$  and  $\alpha = 180^\circ$  configurations.
- The flow field of the single cylinder case at  $U_r = 8$  shows the 2T vortex shedding mode. This is characteristic of the VIV of a single cylinder with low mass-damping in the high Reynolds number regime. For the coupled cylinders configurations, the vortex street around the small cylinder is observed for the  $\alpha = 0^\circ$  and  $\alpha = 90^\circ$  configurations. In addition, the presence of the small cylinder downstream the large cylinder elongates the vortex formation length behind the cylinder bundle. The  $\alpha = 0^\circ$  configuration at  $U_r = 5$  exhibits the 2P vortex shedding mode. For the  $\alpha = 90^\circ$  configuration at  $U_r = 12$  and the  $\alpha = 180^\circ$  configuration at  $U_r = 12$ , a regular vortex shedding mode is not observed due to the galloping response.

## 2. Effect of $G/D$ :

- It is found that with the increase of  $G/D$ ,  $\overline{C}_D$  values decrease and converge to those observed for the single cylinder. The highest magnitudes of  $\overline{C}_L$  are observed for  $G/D = 0.1$  and  $G/D = 0.25$  configurations. The  $\overline{C}_L$  response curve for the  $G/D = 0.5$  configuration is closer to that of the single cylinder.
- The lock-in range of the  $G/D = 0.5$  configuration is similar to that of the single cylinder. For the  $G/D = 0.25$  and  $G/D = 0.1$  configurations, the lock-

in regime extends beyond  $U_r = 12$ . The highest  $A_{y,max}/D$  value of 1.82 is observed for the  $G/D = 0.1$  configuration at  $U_r = 12$ .

- The effect of  $G/D$  on the FIV response of the cylinder bundle is observed in the motion trajectory. With the increase of  $G/D$ , the trajectories become more regular and more similar to those observed for the single cylinder.
- Finally, the velocity in the gap between the cylinders decreases with the increase of  $G/D$ .

## 6.2 Recommendations for Future Work

The following recommendations would contribute to the knowledge of FIV of two coupled cylinders:

- Extend the  $U_r$  range in order to investigate in depth the galloping response of the  $\alpha = 90^\circ$  and  $\alpha = 180^\circ$  configurations. Hence, the lock-in could be fully captured for a complete analysis.
- Extend the present study of the FIV response of the two coupled cylinders for the staggered position,  $0^\circ < \alpha < 90^\circ$  and  $90^\circ < \alpha < 180^\circ$ . Moreover, analyse the effect of  $G/D$  for the  $\alpha = 0^\circ$  and  $\alpha = 180^\circ$  configurations.
- Perform 3D LES of the FIV of two coupled cylinders in the critical regime of  $Re = 1 \times 10^6$ . In addition, study the coherent structures of the flow by carrying out dynamic mode decomposition.

## References

- Achenbach, E. (1968) Distribution of local pressure and skin friction around a circular cylinder in cross-flow up to  $Re = 5 \times 10^6$ . *Journal of Fluid Mechanics*, 34(4), 625–639.
- Catalano, P., Wang, M., Iaccarino, G. and Moin, P. (2003). Numerical simulation of the flow around a circular cylinder at high Reynolds numbers. *International Journal of Heat Fluid Flow*, 24, 463-469.
- Çengel, Y.A. and Cimbala, J.M. (2006). *Fluid Mechanics: Fundamentals and Applications*. McGraw-Hill Higher Education, Boston.
- Ding, L., Zou, Q., Zhang, L. and Wang, H. (2018). Research on Flow-Induced Vibration and Energy Harvesting of Three Circular Cylinders with Roughness Strips in Tandem. *Energies*, 11, 2977 - 2994.
- Feng, C.C. (1968). *The measurement of vortex induced effects in flow past stationary and oscillating circular and D-section cylinders*. Ph. D. thesis, University of British Columbia.
- Jasak, H. (1996). *Error Analysis and Estimation for the Finite Volume Method with Applications to Fluid Flows*, Ph. D. thesis, Imperial College, University of London.
- Jauvtis, N. and Williamson, C.H.K. (2004). The effect of two degrees of freedom on vortex-induced vibration at low mass and damping. *Journal of Fluid Mechanics*, 509, 23–62.
- Kalghatgi, S.G. and Sayer, P.G. (1997). Hydrodynamic Forces on Piggyback Pipeline Configurations. *Journal Waterway Port Coastal Ocean Engineering*, 123, 16–22.
- Khalak, A. and Williamson, C.H.K. (1999). Motions, Forces and Mode Transitions in Vortex-Induced Vibrations at Low Mass-Damping. *Journal of Fluids and Structures*, 13, 813–851.

Kundu, P.K., Cohen, I.M. and Dowling, D.R. (2012). *Fluid Mechanics*. 5th Ed., Academic Press, Waltham, MA.

Lienhard, J. H. (1966). Synopsis of Lift, Drag, and Vortex Frequency Data for Rigid Circular Cylinders. Technical Report 300, Washington State University, College of Engineering, Research Division.

Lam, K. and Lin, Y.F. (2008). Large eddy simulation of flow around wavy cylinders at a subcritical Reynolds number. *International Journal of Heat Fluid Flow*, 29, 1071–1088.

Menter, F. R. (1994). Two-equation eddy-viscosity turbulence models for engineering applications. *AIAA journal*, 32(8), 1598-1605.

Menter, F. R., Kuntz, M. and Langtry, R. (2003). Ten years of industrial experience with the SST turbulence model. *Turbulence, heat and mass transfer*, 4(1), 625-632.

Nakamura, T., Kaneko, S., Inada, F., Kato, M., Ishihara, K., Nishihara, T., Mureithi, N.W. and Langthjem, M.A. (2013). *Flow-Induced Vibrations: Classifications and Lessons from Practical Experiences*. Butterworth-Heinemann.

Ong, M.C., Utnes, T., Holmedal, L.E., Myrhaug, D. and Pettersen, B. (2009). Numerical simulation of flow around a smooth circular cylinder at very high Reynolds numbers. *Marine Structures*, 22, 142–153.

Porteous, A., Habbit, R., Colmenares, J., Poroseva, S. and Murman, S.M. (2015). Simulations of Incompressible Separated Turbulent Flows around Two-Dimensional Bodies with URANS Models in OpenFOAM. In *22nd AIAA Computational Fluid Dynamics Conference*. Dallas, TX.

Roshko, A. (1961). Experiments on the Flow Past a Circular Cylinder at Very High Reynolds Number. *Journal of Fluid Mechanics*, 10 (3), 345–56.

Sarpkaya, T. (2004). A Critical Review of the Intrinsic Nature of Vortex-Induced Vibrations. *Journal of Fluids and Structures*, 19 (4), 389–447.

- Schäfer, M. (2006). *Computational Engineering: Introduction to Numerical Methods*. Springer, Berlin.
- Schewe, G. (1983). On the force fluctuations acting on a circular cylinder in crossflow from subcritical up to transcritical Reynolds numbers. *Journal of Fluid Mechanics*, 133, 265–285.
- Sumer, B.M. and Fredsøe, J. (2006). *Hydrodynamics around cylindrical structures, Advanced Series on Ocean Engineering*. World Scientific Publishing Co. Ptc. Ltd.
- Sumner, D. (2010). Two circular cylinders in cross-flow: A review. *Journal of Fluids and Structures*, 26, 849–899.
- Tennekes, H. and Lumley, J.L. (1972). *A First Course in Turbulence*. Cambridge, MA: MIT Press.
- Tsutsui, T., Igarashi, T. and Kamemoto, K. (1997). Interactive flow around two circular cylinders of different diameters at close proximity. Experiment and numerical analysis by vortex method. *Journal of Wind Engineering and Industrial Aerodynamics*, 69 - 71, 279–291.
- Versteeg, H.K. and Malalasekera, W. (2007). *An introduction to computational fluid dynamics: the finite volume method*, 2nd Ed. Pearson Education Ltd, Harlow, England ; New York.
- Williamson, C.H.K. and Govardhan, R. (2004). Vortex-Induced Vibrations. *Annual Review of Fluid Mechanics*, 36:413-455.
- Williamson, C.H.K. and Roshko, A. (1988). Vortex formation in the wake of an oscillating cylinder. *Journal of Fluids and Structures*, 2, 355–381.
- Zang, Z., Gao, F. and Cui, J. (2012). Vortex Shedding and Vortex-Induced Vibration of Piggyback Pipelines in Steady Currents. *The Twenty-second International Offshore and Polar Engineering Conference*. International Society of Offshore and Polar Engineers.



Zang, Z., Gao, F., Mou, Y. and Li, Z. (2013). Transverse VIV Response of Piggyback Pipelines with Various Configurations in Ocean Current. *The Twenty-third International Offshore and Polar Engineering Conference*. International Society of Offshore and Polar Engineers.

Zang, Z. P. and Gao, F. P. (2014). Steady current induced vibration of near-bed piggyback pipelines: Configuration effects on VIV suppression. *Applied Ocean Research*, 46, 62–69.

Zdravkovich, M.M. (1997). *Flow around a Circular Cylinders: Volume I: Fundamentals*. Oxford Science Publications.

Zhao, M., Cheng, L., Teng, B. and Liang, D. (2005). Numerical Simulation of Viscous Flow Past Two Circular Cylinders of Different Diameters. *Applied Ocean Research*, 27 (1), 39–55.

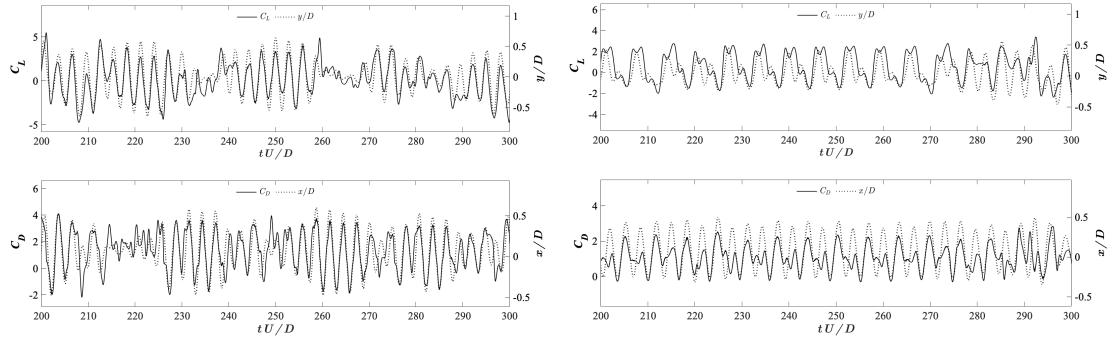
Zhao, M., Cheng, L., Teng, B. and Dong, G. (2007). Hydrodynamic forces on dual cylinders of different diameters in steady currents. *Journal of Fluids and Structures*, 23, 59–83.

Zhao, M., Midson, J. and Pearcey, T. (2016). Vortex-induced Vibration of Side-by-side Dual Cylinders of Different Diameters. *The Twelfth ISOPE Pacific/Asia Offshore Mechanics Symposium*. International Society of Offshore and Polar Engineers.

Zhao, M. and Yan, G. (2013). Numerical simulation of vortex-induced vibration of two circular cylinders of different diameters at low Reynolds number. *Physics of Fluids*, 25(8), 083601.

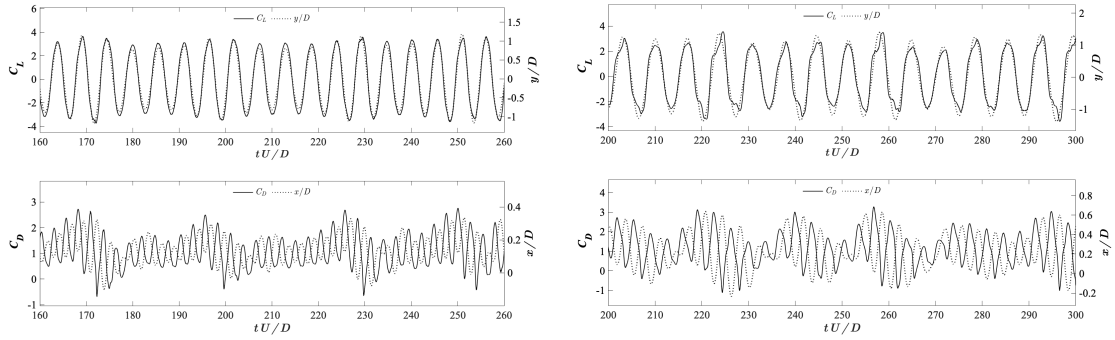
# Appendix A

Time histories of the hydrodynamic coefficients and normalized displacements



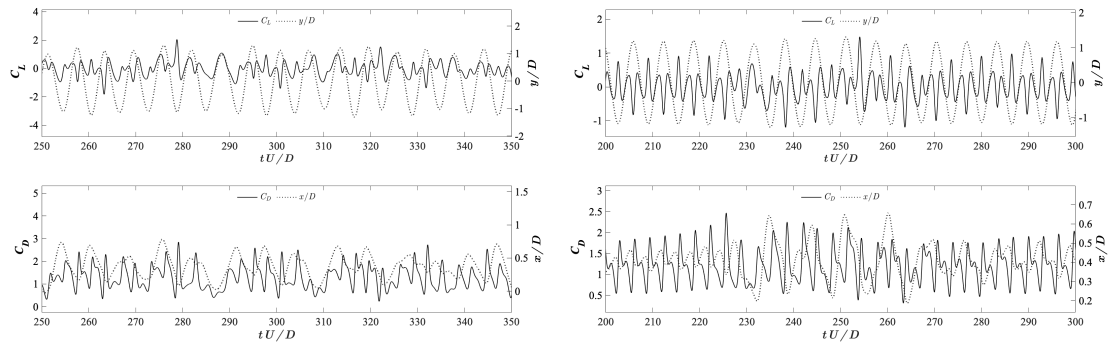
(a)  $U_r = 2.5$

(b)  $U_r = 3$



(c)  $U_r = 4$

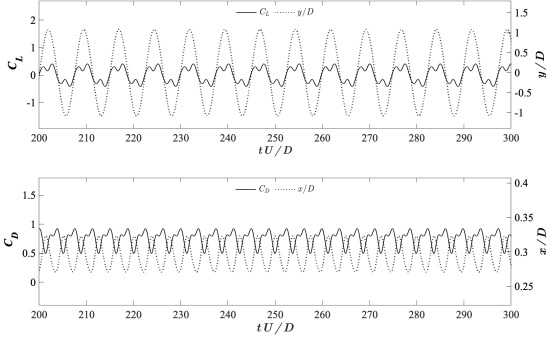
(d)  $U_r = 5$



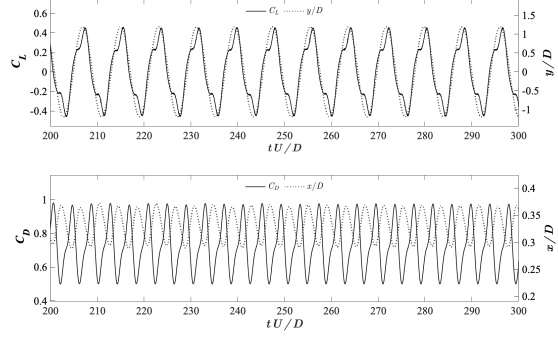
(e)  $U_r = 6$

(f)  $U_r = 6.5$

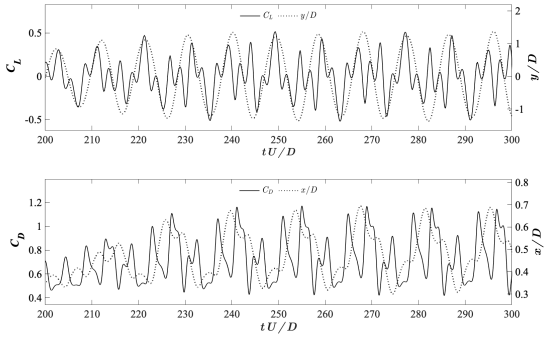
Figure A1: Time histories of  $C_L$ ,  $C_D$ ,  $y/D$  and  $x/D$ : single cylinder,  $U_r = 2.5 - 6.5$



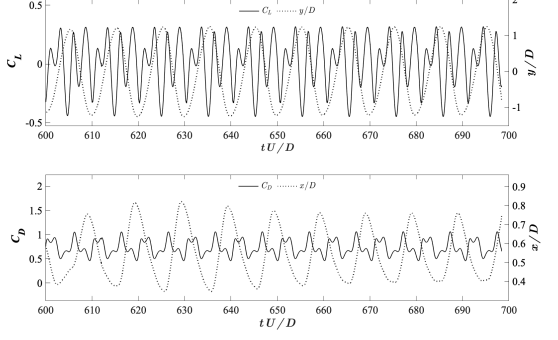
(a)  $U_r = 7$



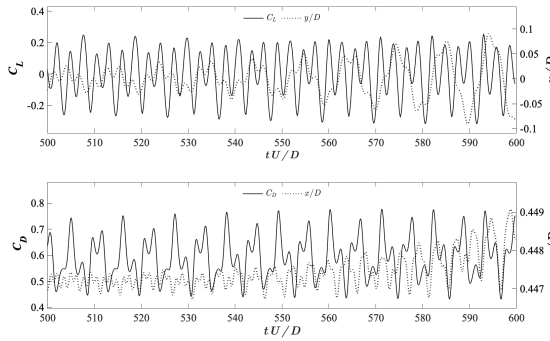
(b)  $U_r = 7.5$



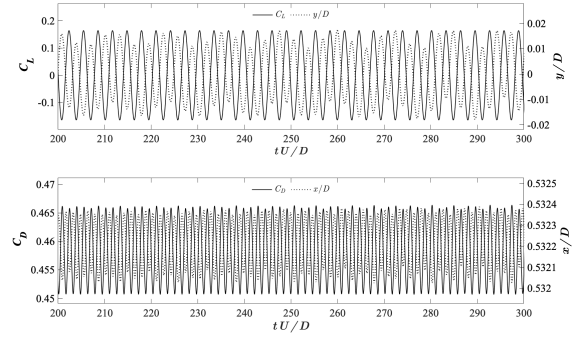
(c)  $U_r = 9$



(d)  $U_r = 10$



(e)  $U_r = 11$



(f)  $U_r = 12$

Figure A2: Time histories of  $C_L$ ,  $C_D$ ,  $y/D$  and  $x/D$ : single cylinder,  $U_r = 7 - 12$

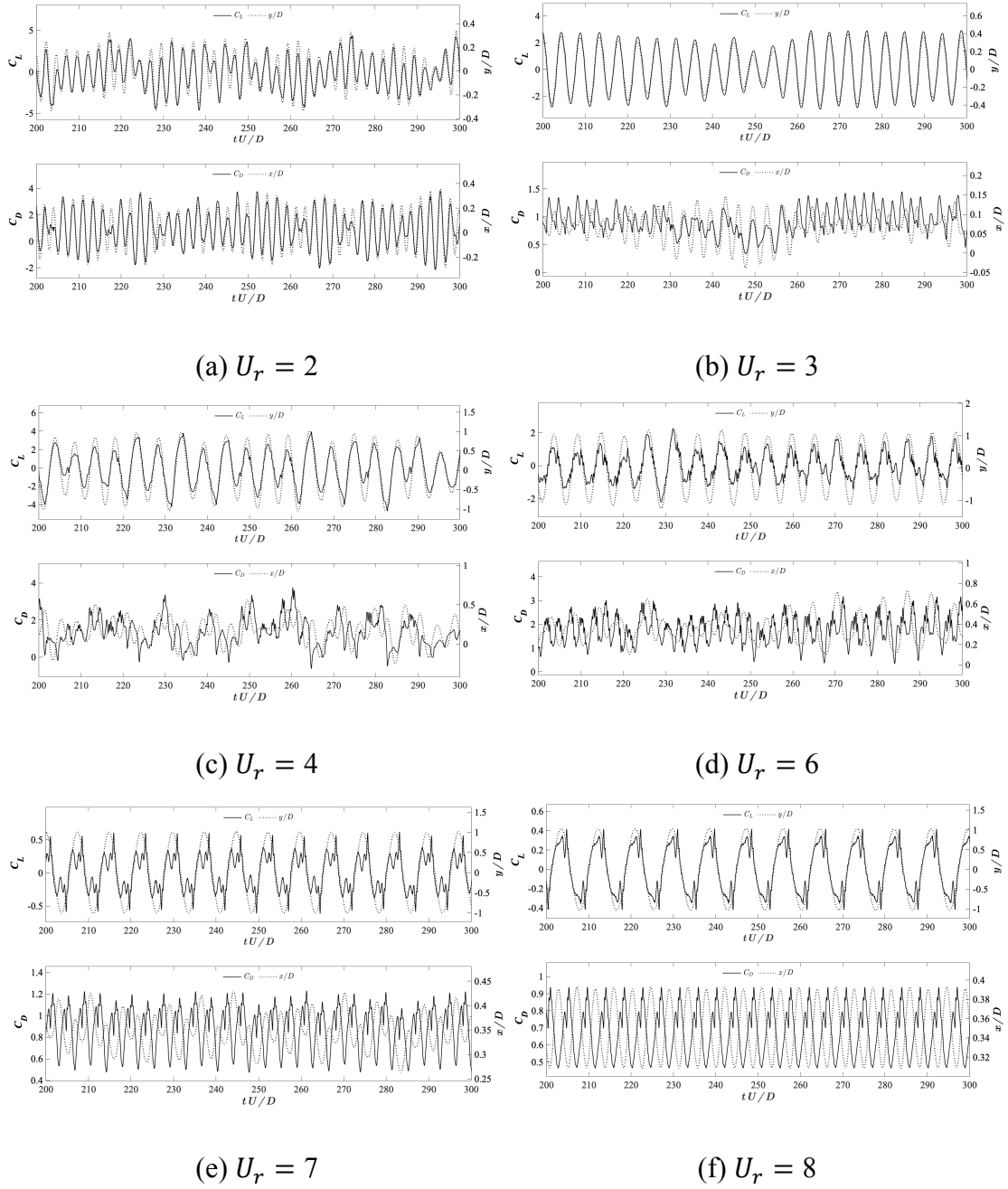


Figure A3: Time histories of  $C_L$ ,  $C_D$ ,  $y/D$  and  $x/D$ :  $\alpha = 0^\circ$ ,  $G/D = 0.1$ ,  $U_r = 2 - 8$

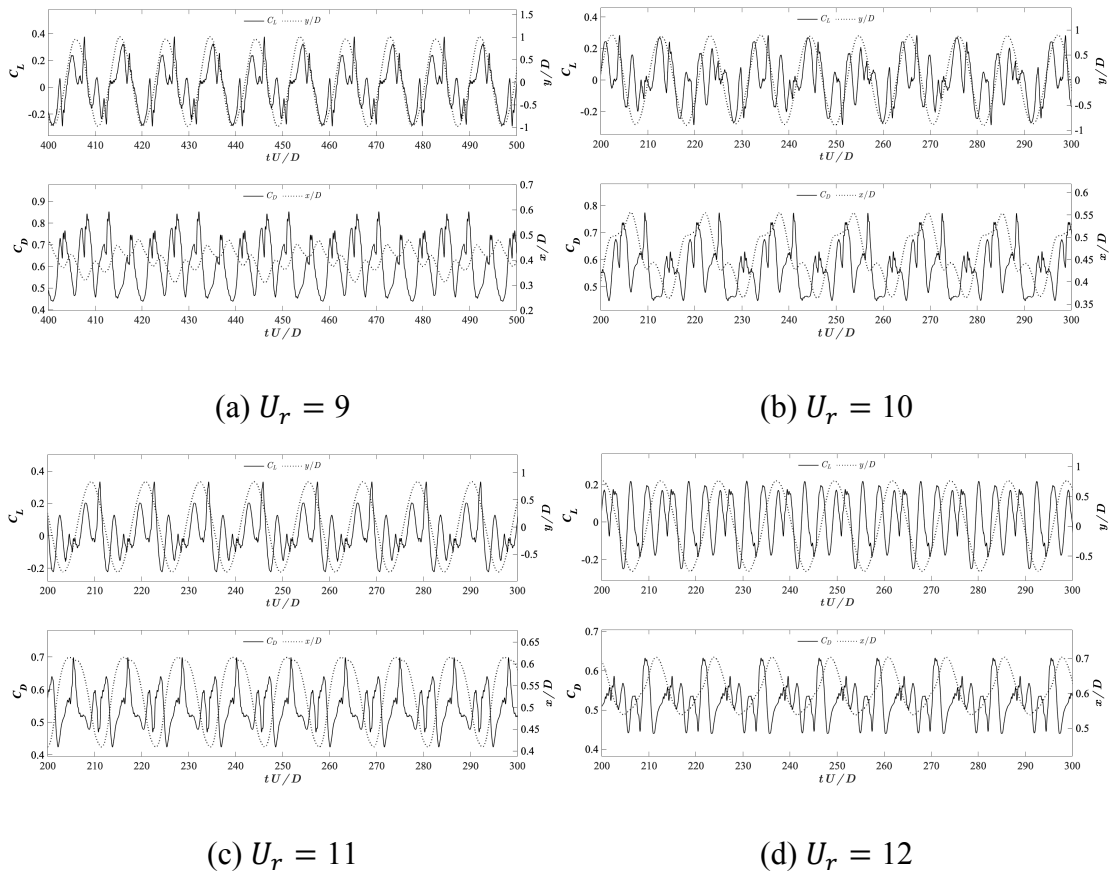
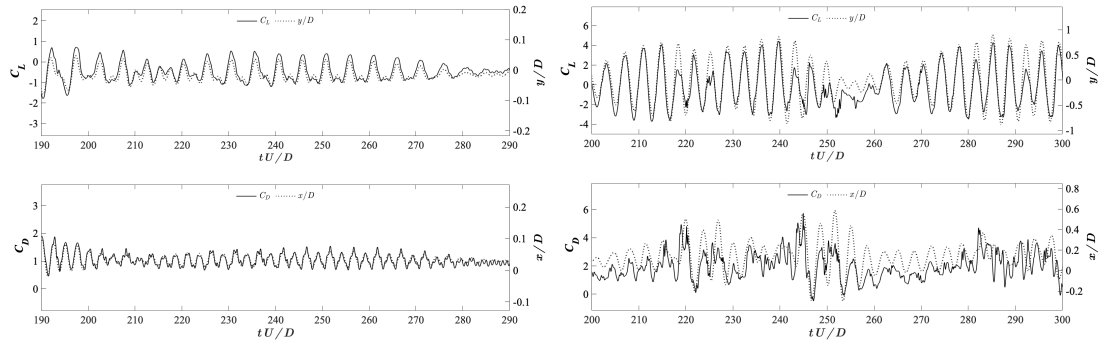
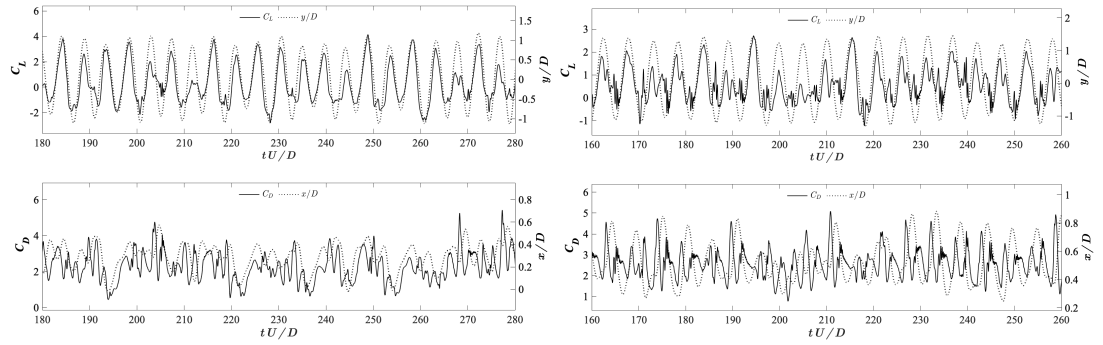


Figure A4: Time histories of  $C_L$ ,  $C_D$ ,  $y/D$  and  $x/D$ :  $\alpha = 0^\circ$ ,  $G/D = 0.1$ ,  $U_r = 9 - 12$



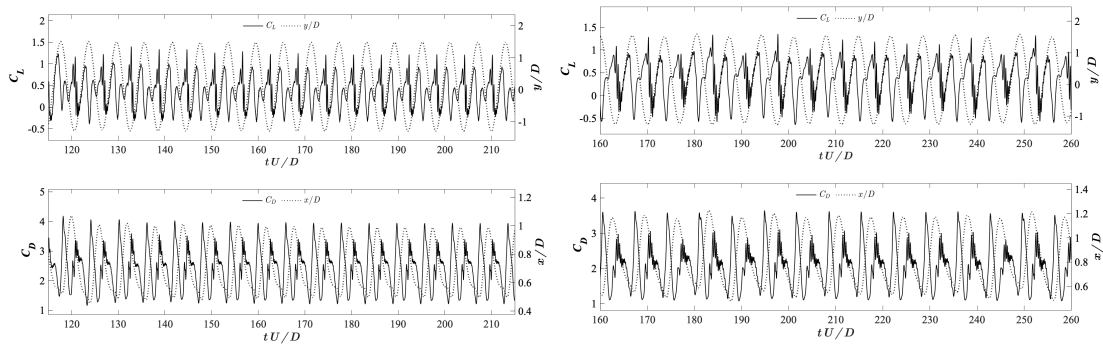
(a)  $U_r = 2$

(b)  $U_r = 3$



(c)  $U_r = 4$

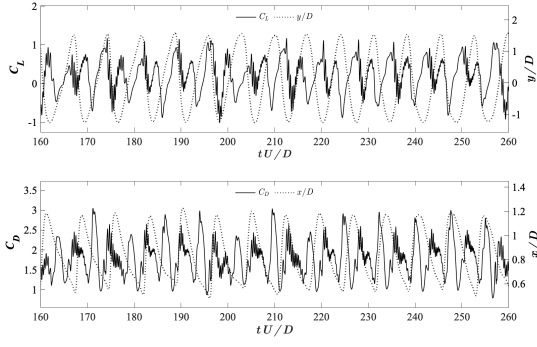
(d)  $U_r = 5$



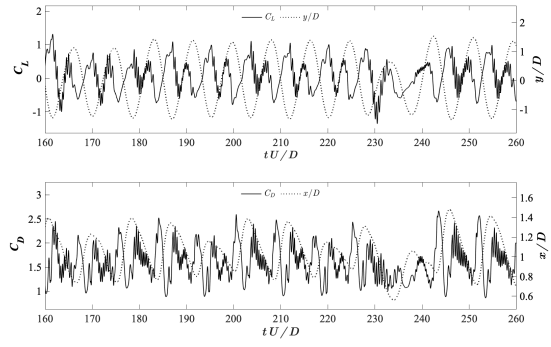
(e)  $U_r = 6$

(f)  $U_r = 7$

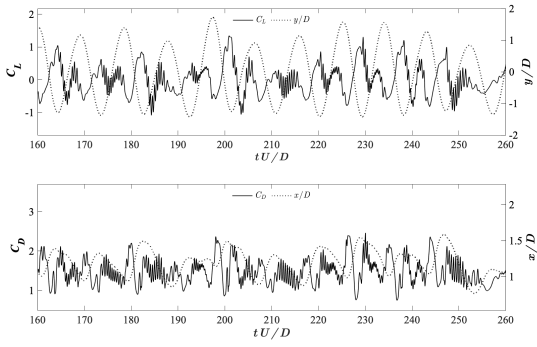
Figure A5: Time histories of  $C_L$ ,  $C_D$ ,  $y/D$  and  $x/D$ :  $\alpha = 90^\circ$ ,  $G/D = 0.1$ ,  $U_r = 2 - 7$



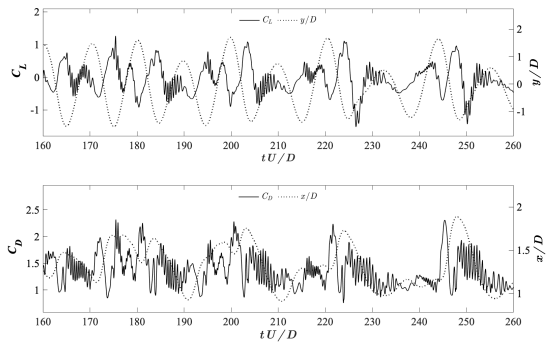
(g)  $U_r = 8$



(h)  $U_r = 9$

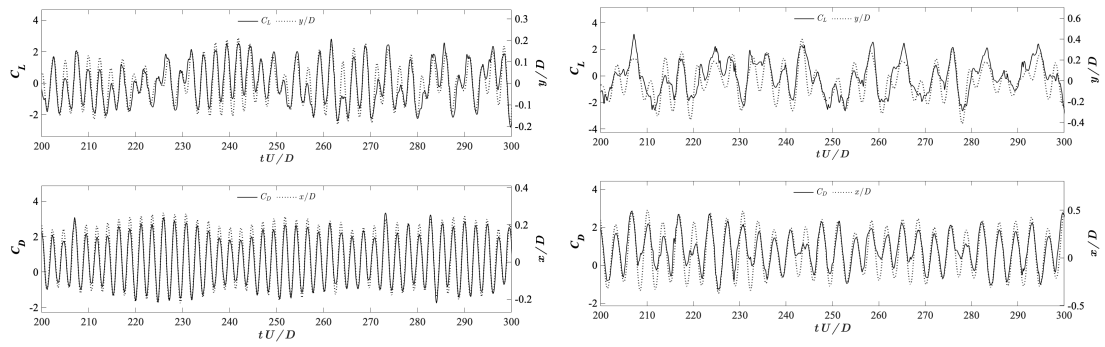


(a)  $U_r = 10$



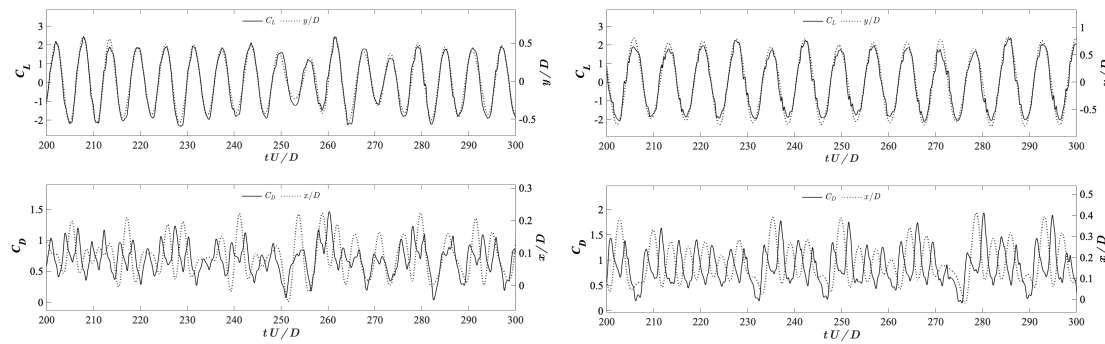
(b)  $U_r = 11$

Figure A6: Time histories of  $C_L$ ,  $C_D$ ,  $y/D$  and  $x/D$ :  $\alpha = 90^\circ$ ,  $G/D = 0.1$ ,  $U_r = 8 - 11$



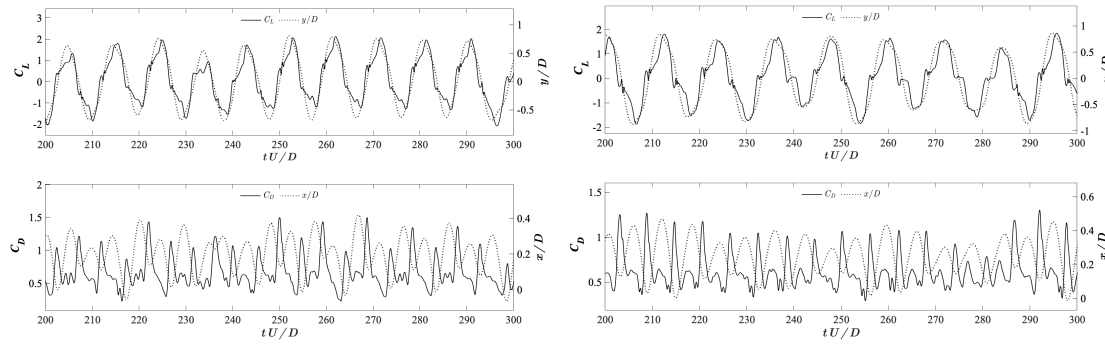
(a)  $U_r = 2$

(b)  $U_r = 3$



(c)  $U_r = 4$

(d)  $U_r = 5$

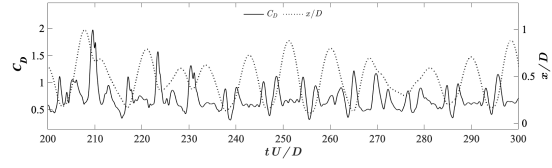
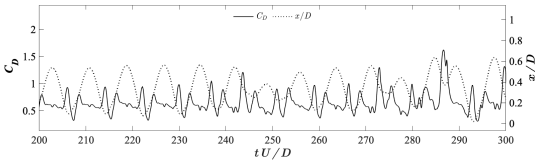
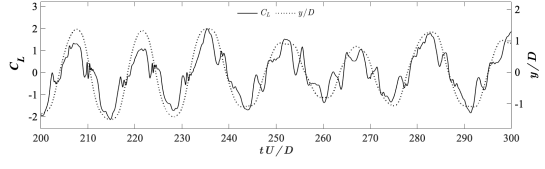
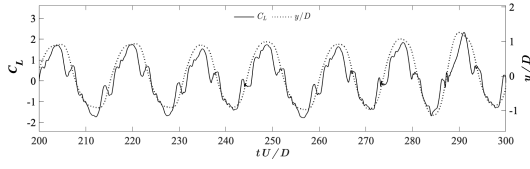


(e)  $U_r = 6$

(f)  $U_r = 7$

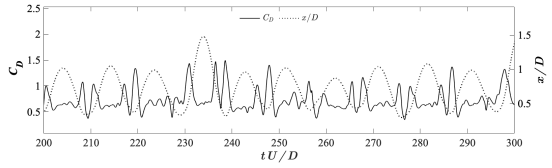
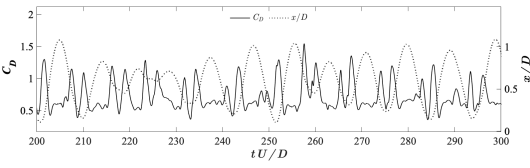
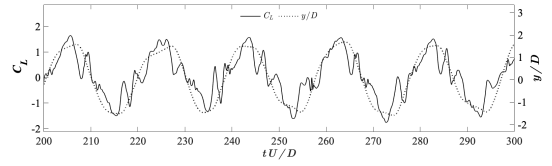
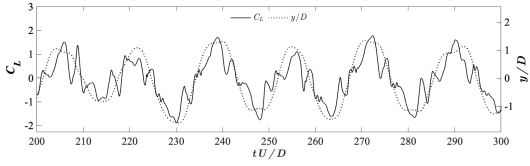
Figure A7: Time histories of  $C_L$ ,  $C_D$ ,  $y/D$  and  $x/D$ :  $\alpha = 180^\circ$ ,  $G/D = 0.1$ ,  $U_r = 2 - 7$





(g)  $U_r = 8$

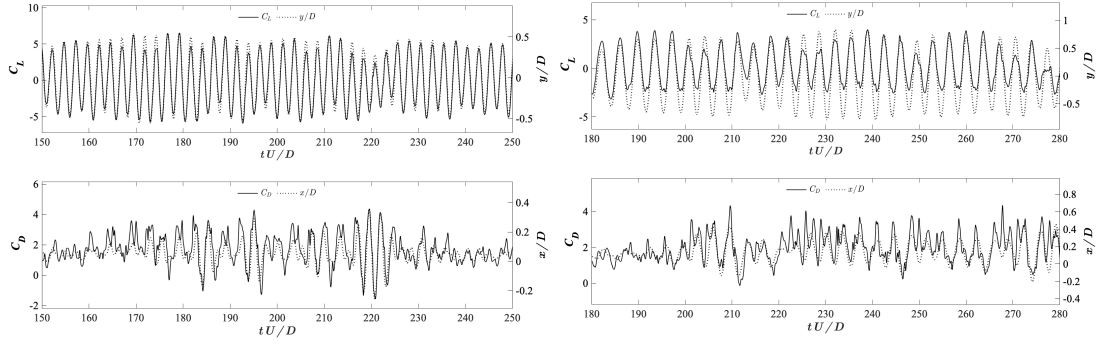
(h)  $U_r = 9$



(a)  $U_r = 10$

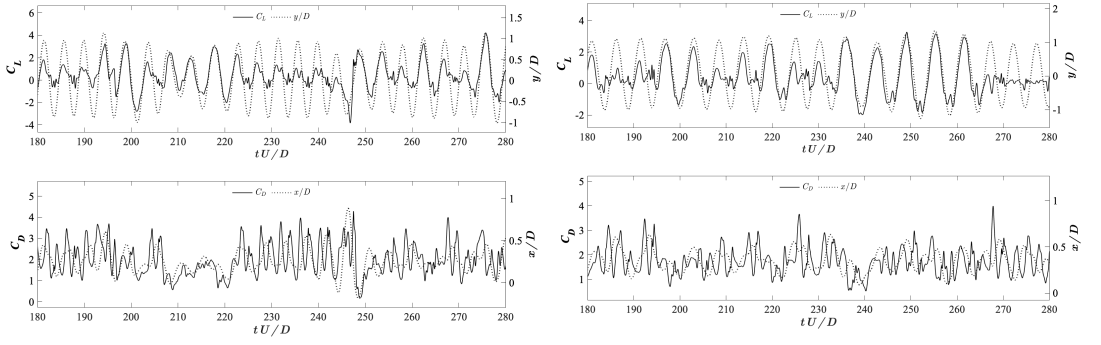
(b)  $U_r = 11$

Figure A8: Time histories of  $C_L$ ,  $C_D$ ,  $y/D$  and  $x/D$ :  $\alpha = 180^\circ$ ,  $G/D = 0.1$ ,  $U_r = 8 - 11$



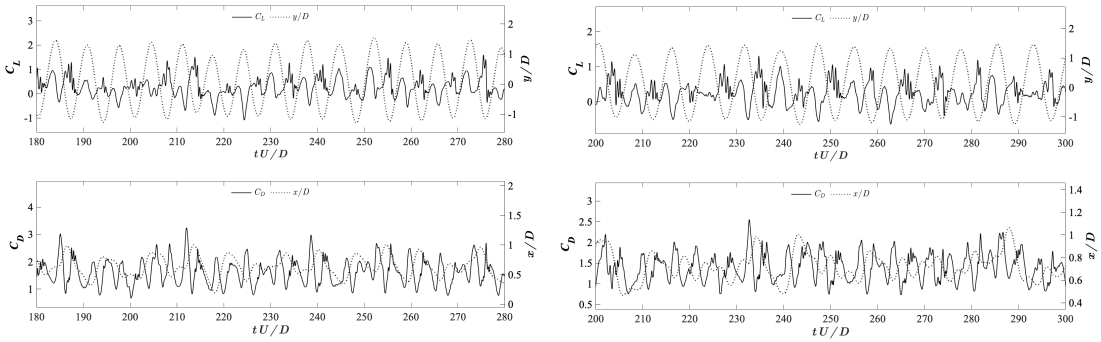
(a)  $U_r = 2$

(b)  $U_r = 3$



(c)  $U_r = 4$

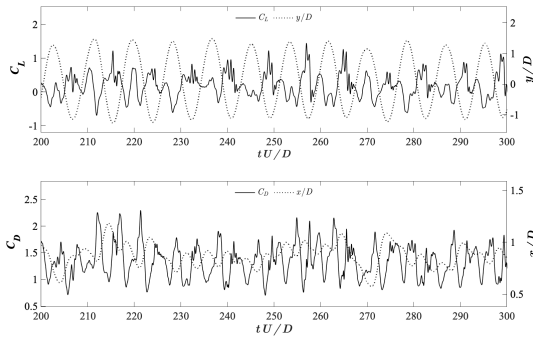
(d)  $U_r = 5$



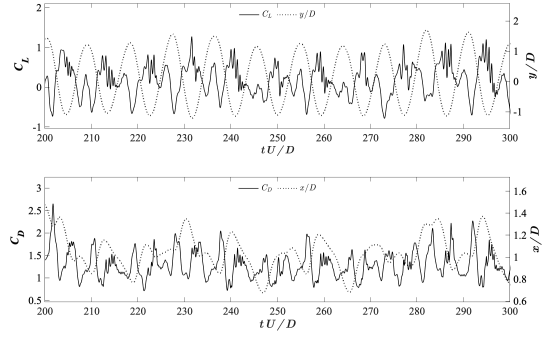
(e)  $U_r = 7$

(f)  $U_r = 8$

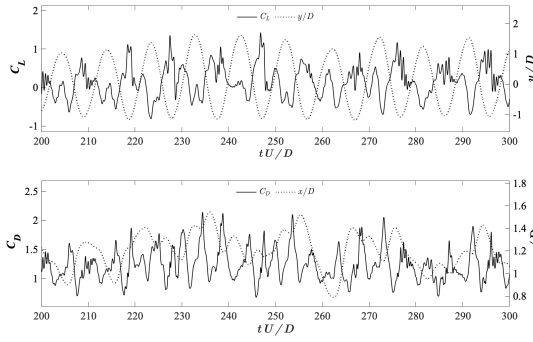
Figure A9: Time histories of  $C_L$ ,  $C_D$ ,  $y/D$  and  $x/D$ :  $\alpha = 90^\circ$ ,  $G/D = 0.25$ ,  $U_r = 2 - 8$



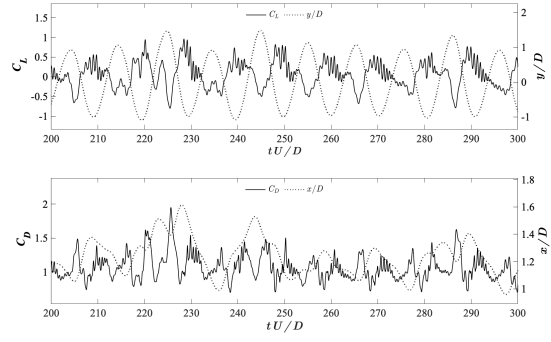
(g)  $U_r = 9$



(h)  $U_r = 10$

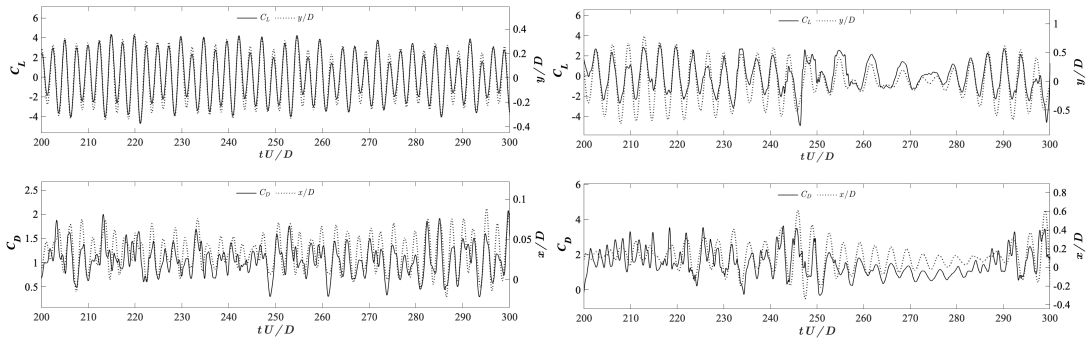


(a)  $U_r = 11$



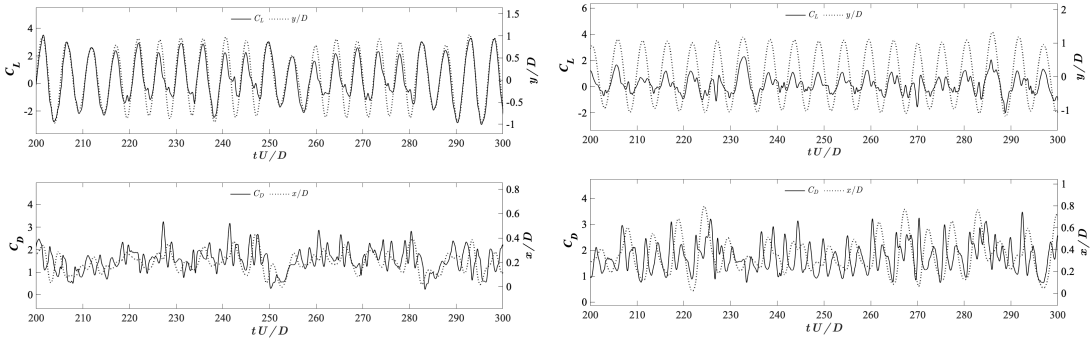
(b)  $U_r = 12$

Figure A10: Time histories of  $C_L$ ,  $C_D$ ,  $y/D$  and  $x/D$ :  $\alpha = 90^\circ$ ,  $G/D = 0.25$ ,  $U_r = 9 - 12$



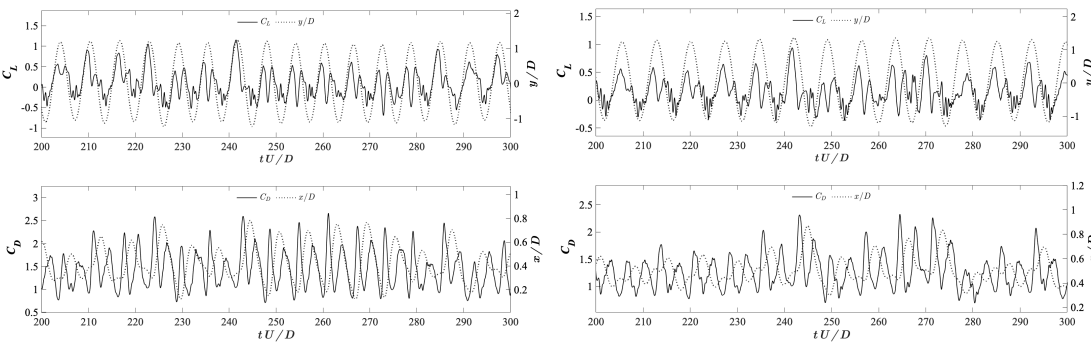
(a)  $U_r = 2$

(b)  $U_r = 3$



(c)  $U_r = 4$

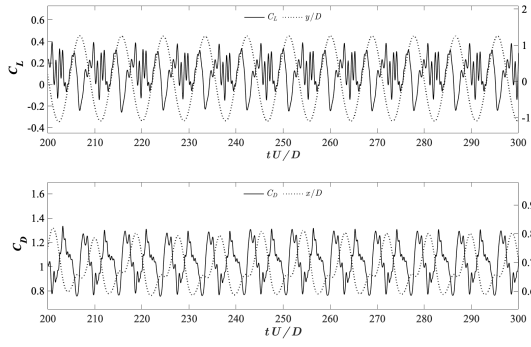
(d)  $U_r = 5$



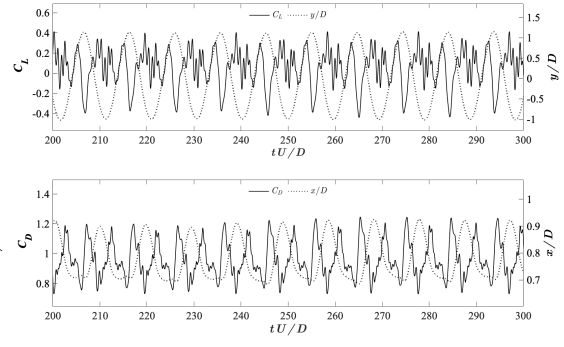
(e)  $U_r = 6$

(f)  $U_r = 7$

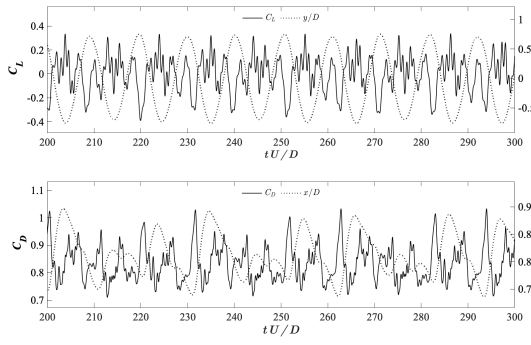
Figure A11: Time histories of  $C_L$ ,  $C_D$ ,  $y/D$  and  $x/D$ :  $\alpha = 90^\circ$ ,  $G/D = 0.5$ ,  $U_r = 2 - 7$



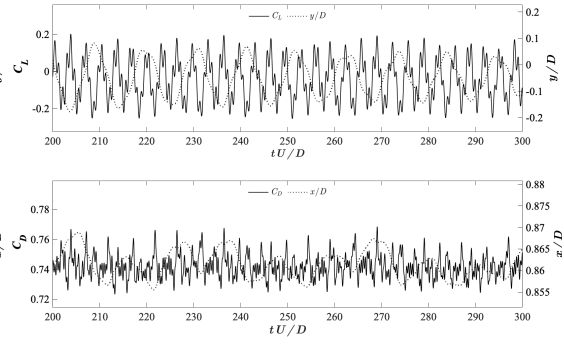
(g)  $U_r = 9$



(h)  $U_r = 10$



(a)  $U_r = 11$



(b)  $U_r = 12$

Figure A12: Time histories of  $C_L$ ,  $C_D$ ,  $y/D$  and  $x/D$ :  $\alpha = 90^\circ$ ,  $G/D = 0.5$ ,  $U_r = 9 - 12$